

## **INFORMATION TO USERS**

**This manuscript has been reproduced from the microfilm master. UMI films the text directly from the original or copy submitted. Thus, some thesis and dissertation copies are in typewriter face, while others may be from any type of computer printer.**

**The quality of this reproduction is dependent upon the quality of the copy submitted. Broken or indistinct print, colored or poor quality illustrations and photographs, print bleedthrough, substandard margins, and improper alignment can adversely affect reproduction.**

**In the unlikely event that the author did not send UMI a complete manuscript and there are missing pages, these will be noted. Also, if unauthorized copyright material had to be removed, a note will indicate the deletion.**

**Oversize materials (e.g., maps, drawings, charts) are reproduced by sectioning the original, beginning at the upper left-hand corner and continuing from left to right in equal sections with small overlaps.**

**Photographs included in the original manuscript have been reproduced xerographically in this copy. Higher quality 6" x 9" black and white photographic prints are available for any photographs or illustrations appearing in this copy for an additional charge. Contact UMI directly to order.**

**Bell & Howell Information and Learning  
300 North Zeeb Road, Ann Arbor, MI 48106-1346 USA  
800-521-0600**

**UMI<sup>®</sup>**



**ASSIMILATION OF SATELLITE-DERIVED CLOUD COVER INTO THE  
REGIONAL ATMOSPHERIC MODEL SYSTEM (RAMS) AND ITS IMPACTS  
ON MODELED SURFACE FIELDS**

by

**Ismail Yucel**

---

**A Dissertation Submitted to the Faculty of the  
DEPARTMENT OF HYDROLOGY AND WATER RESOURCES**

**In Partial Fulfillment of the Requirements**

**For the Degree of**

**DOCTOR OF PHILOSOPHY**

**WITH A MAJOR IN HYDROLOGY**

**In the Graduate College**

**THE UNIVERSITY OF ARIZONA**

**2001**

UMI Number: 3002537

**UMI<sup>®</sup>**

---

UMI Microform 3002537

Copyright 2001 by Bell & Howell Information and Learning Company.

All rights reserved. This microform edition is protected against  
unauthorized copying under Title 17, United States Code.

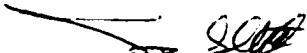
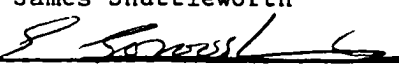
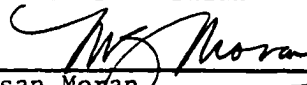
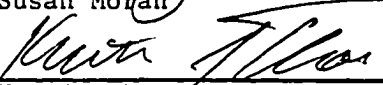
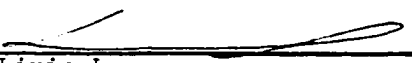
---

Bell & Howell Information and Learning Company  
300 North Zeeb Road  
P.O. Box 1346  
Ann Arbor, MI 48106-1346

THE UNIVERSITY OF ARIZONA ©  
GRADUATE COLLEGE

As members of the Final Examination Committee, we certify that we have read the dissertation prepared by Ismail Yucel entitled Assimilation of Satellite-Derived Cloud Cover into the Regional Atmospheric Model System (RAMS) and Its Impacts on Modeled Surface Fields

and recommend that it be accepted as fulfilling the dissertation requirement for the Degree of Doctor of Philosophy

 _____	_____
W. James Shuttleworth	Date
 _____	<u>1/12/01</u>
Soroosh Sorooshian	Date
 _____	<u>12 Jan 01</u>
Susan Moran	Date
 _____	<u>12 Jan 01</u>
Kurtis Thome	Date
 _____	<u>01/16/01</u>
Lixin Lu	Date

Final approval and acceptance of this dissertation is contingent upon the candidate's submission of the final copy of the dissertation to the Graduate College.

I hereby certify that I have read this dissertation prepared under my direction and recommend that it be accepted as fulfilling the dissertation requirement.

 _____	<u>1/15/01</u>
Dissertation Director	Date
W. James Shuttleworth	

### STATEMENT BY THE AUTHOR

This dissertation has been submitted in partial fulfillment of requirements for an advanced degree at the University of Arizona and is deposited in the University Library to be made available to borrowers under rules of the Library.

Brief quotations from this dissertation are allowed without special permission, provided that accurate acknowledgment of source is made. Requests for permission for extended quotation from or reproduction of this manuscript in whole or in part may be granted by the head of the major department or the Dean of the Graduate College when in his or her judgment the proposed use of the material is in the interest of scholarship. In all instances, however, permission must be obtained from the author.

SIGNED: \_\_\_\_\_



## ACKNOWLEDGMENTS

I would like to acknowledge all those who have contributed time and effort for this research directly or indirectly. I am especially thankful to my major advisor Professor W. James Shuttleworth for his very valuable insight and support for this research and for his guidance with an unmatched wisdom. I am also very thankful to Dr. Lixin Lu for her help and support in completing this dissertation. I wish to thank Professors Sorosh Sorooshian, Kurtis Thome and Susan Moran for serving in my examination committee and for offering their support. I am very grateful to Dr. Rachel T. Pinker for providing GEWEX/SRB model and original cloud screening algorithm for use in this research. I am also thankful to Dr. James Toth for his help and support at the early stage of this research and to Dr. Jaime Garatuza-Payan for exchanging information on the development of cloud screening algorithm and to Dr. Russell Scott for collecting data from infrared radiometer. I greatly appreciate Mr. Dan Braithwaite's assistance in providing the required satellite data sets. Finally, I express my appreciation to Altaf Muhammad, Omer L. Sen, Eleanor Burke, David Gochis and Khilha Lee for providing help and patient ears during my stay at The University of Arizona.

Financial support during my stay at The University of Arizona was provided by the NASA-EOS grant, NAG6W-2Y25 and by the Ministry of Education, Turkey.

I wish to thank all my family for their unwavering support and encouragement. I thank my parents Mustafa and Tevhide for instilling a sense of wonder and exploration in me. I thank my life-partner and best friend Sema who has been my primary support in this endeavor through her patience, encouragement and strength. Our future together is one of the motivating factors in my life. I thank my son, Mustafa Safa, for lending me the times when I had to spend with him.

Finally, but most important, I am very thankful to God Almighty on successful completion of my graduate studies. It is only through him that my life has meaning and direction.

## **DEDICATION**

**This work is dedicated to:**

**My Family, for their love and support**

***Mustafa Safa and Sema***

***Mustafa and Tevhide***

## TABLE OF CONTENTS

LIST OF ILLUSTRATIONS .....	10
LIST OF TABLES .....	16
ABSTRACT .....	17
<b>1. INTRODUCTION .....</b>	<b>19</b>
1.1 Introduction .....	19
1.2 Problem Definition .....	23
1.3 Historical Overview .....	25
1.4 Research Objectives .....	28
1.5 Summary of Dissertation .....	32
<b>2. MODEL DESCRIPTION .....</b>	<b>33</b>
2.1 Introduction .....	33
2.2 Description of the Version 3b of the RAMS Model .....	33
2.2.1 Microphysics Parameterization .....	39
2.2.2 Radiation Parameterization .....	43
2.3 Description of the UMD GEWEX/SRB Model .....	49
2.3.1 Radiative Transfer Technique .....	49
2.3.2 Satellite Algorithm .....	53

<b>3.</b>	<b>RESEARCH LOCATION AND DATA</b> .....	59
3.1	Introduction .....	59
3.2	Field Data .....	59
3.2.1	Southern Arizona Site .....	59
3.2.1.1	Data from AZMET Network .....	63
3.2.2	Experiment Site .....	66
3.3	Satellite Data .....	67
3.4	Modeled-Derived Data .....	69
<b>4.</b>	<b>CLOUD SCREENING ALGORITHM</b> .....	73
4.1	Introduction .....	73
4.2	Methodology .....	74
4.2.1	Deriving Clear-Sky Composite Images .....	75
4.2.2	Deriving Fractional Cloud Cover .....	78
4.3	Application and Evaluation of the Algorithm .....	80
4.3.1	<i>Spatial Patterns</i> .....	80
4.3.2	<i>Time series</i> .....	82
<b>5.</b>	<b>ASSIMILATING SATELLITE DATA</b> .....	92

	8
5.1 Introduction .....	92
5.2 Assimilating Satellite-Derived Solar Radiation .....	93
5.3 Assimilating Satellite-Derived Cloud Cover .....	97
5.3.1 Whole-Column Cloud Water and Ice Estimated from Satellite .	98
5.3.2 Fractional Cloud Mass Profiles Represented in RAMS Prior to Assimilation .....	99
5.3.3 Updating the RAMS Cloud Field and Air Temperature .....	103
5.3.4 Assimilation Using Different Frequencies .....	105
<b>6. RESULTS .....</b>	<b>112</b>
6.1 Evaluation .....	112
6.2 Impact of Cloud Assimilation on Atmospheric Wind Speed .....	113
6.3 Impact of Cloud Assimilation on the Surface Energy and Water Balance	117
6.3.1 Evaluation of Model-Derived Near-Surface Data Relative to Observations .....	117
6.3.1.1 Incoming Short-wave Radiation .....	118
6.3.1.2 Incoming Long-wave Radiation .....	129
6.3.1.3 Precipitation .....	135
6.4 Ensemble Runs .....	146
<b>7. SUMMARY, CONCLUSIONS AND RECOMMENDATIONS .....</b>	<b>156</b>
7.1 Summary .....	156

	9
7.2 Conclusions .....	158
7.3 Recommendations .....	161
<b>REFERENCES</b> .....	<b>163</b>

## LIST OF ILLUSTRATIONS

<u>Figure</u>	<u>Page</u>
2.1	The sigma coordinate framework ..... 35
2.2	Flow diagram illustrating the microphysical processes considered in the model ..... 43
2.3	(a) The spatial patterns of incoming solar radiation for the Chen/Cotton scheme and (b) for the Harrington scheme. In (c) the scatter plot of two schemes is illustrated ..... 48
2.4	The retrieval of surface albedo is illustrated in (a) and the retrieval of surface solar radiation is summarized in (b) ..... 58
3.1	The state of Arizona showing the general location of the AZMET networks in southern part of the state. The labels at the top-right-hand corners of each small square identify the station number of each AZMET site ..... 70
3.2	The broken line shows the area coverage of visible images which includes 1200 (1-km) pixels in X direction and 1000 (1-km) pixels in Y direction ..... 71
4.1	(a) Flow chart of the procedure used to estimate the clear-sky reflectance for each of the 4 x 4 km target areas in the real-time tracking. (b) Flow chart of the procedure used to assign pixels in each target area into the “clear-sky” and “cloudy-covered” categories. .... 84
4.2	(a) Daily average clear-sky composite radiances for July 16, 1999 and for June 23, 2000. (b) The frequency distributions for clear-sky composite radiance at GMT 16:00 for July 16, 1999 and for June 23, 2000, while the same histograms are shown for the GMT 22:00 in (c) ..... 85
4.3	The GOES visible image and the main outputs from the cloud-screening algorithm, specifically the cloud fraction, and the cloudy, clear and composite radiance images for July 14, 1999 at GMT 22:00. .... 86
4.4	The GOES visible image and the main outputs from the cloud-screening

	algorithm, specifically the cloud fraction, and the cloudy, clear and composite radiance images for June 22, 2000 at GMT 20:00. ....	87
4.5a	Time series of cloudy radiance, clear radiance, composite radiance, and cloud cover over the AZMET sites for July 14-16, 1999 . ....	88
4.5b	Time series of cloudy radiance, clear radiance, composite radiance, and cloud cover over the AZMET sites for July 14-16, 1999 . ....	89
4.6a	Time series of cloudy radiance, clear radiance, composite radiance, and cloud cover over the AZMET sites for June 22-23, 2000 . ....	90
4.6b	Time series of cloudy radiance, clear radiance, composite radiance, and cloud cover over the AZMET sites for June 22-23, 2000 . ....	91
5.1	(a) Comparison between observed incoming solar radiation and incoming solar radiation computed using the UMD GEWEX/SRB model for a field site near Obregon in Mexico on September 30, 1998. (b) and (c) average diurnal cycle observed incoming solar radiation and incoming solar radiation computed using the UMD GEWEX/SRB during 1998 for a field site near Obregon in Mexico and a field site in the San Pedro River basin, respectively . ....	96
5.2	Comparison of RAMS-calculated absorbed net short-wave radiation (a) without, and (b) with GOES data . ....	97
5.3	Diagram showing the entire steps for assimilating satellite-derived cloud fields into RAMS model . ....	107
5.4	Application of weighted interpolation method for cloud optical-depth values. Solid line shows the RAMS model domain to where optical depth values were interpolated . ....	108
5.5	Comparison between the total cloud/ice mixing ratio in the vertical column across the modeled domain with observations derived from GOES images assimilated into RAMS at 30 minute intervals. The first column show values immediately before next assimilation takes place, the second column shows the assimilated cloud image, third column shows the modeled field one time step after assimilation, while the fourth column shows the field calculated by RAMS when there is no assimilation of satellite observations (Results on July 14, 1999) . ....	109

5.6	Comparison between the total cloud/ice mixing ratio in the vertical column across the modeled domain with observations derived from GOES images assimilated into RAMS at 15 minutes and 30 minutes, respectively. The first and third columns show values immediately before next assimilation takes place, the second column shows the assimilated cloud image, and the fourth column shows the field calculated by RAMS when there is no assimilation of satellite observations (Results on July 14, 1999) . . . . .	110
5.7	Comparison between the total cloud/ice mixing ratio in the vertical column across the modeled domain with observations derived from GOES images assimilated into RAMS at every minute applying linear interpolation between image cycles. The column shows values immediately before next assimilation takes place, the second column shows the assimilated cloud image, the third column shows the modeled field one time step after assimilation, while the fourth column shows the field calculated by RAMS when there is no assimilation of satellite observations (Results on July 14, 1999) . . . . .	111
6.1	Comparison between the fields cloud water/ice mixing ratio, vertical wind speed and compound wind speed calculated by RAMS without cloud assimilation and with cloud assimilation on June 22, 2000 at GMT 20:00 at vertical level 17 in the model . . . . .	116
6.2a	RAMS-derived surface solar radiation, with and without cloud assimilation, averaged over hourly intervals on July 14-16, 1999 compared with observed values at the AZMET surface meteorology sites in Southern Arizona . . . . .	122
6.2b	RAMS-derived surface solar radiation, with and without cloud assimilation, averaged over hourly intervals on July 14-16, 1999 compared with observed values at the AZMET surface meteorology sites in Southern Arizona . . . . .	123
6.3a	RAMS-derived surface solar radiation, with and without cloud assimilation, averaged over hourly intervals on June 22-23, 2000 compared with observed values at the AZMET surface meteorology sites in Southern Arizona . . . . .	124
6.3b	RAMS-derived surface solar radiation, with and without cloud assimilation, averaged over hourly intervals on June 22-23, 2000 compared with observed values at the AZMET surface meteorology sites in Southern Arizona . . . . .	125

6.4	Scatter plots of hourly-average modeled and observed surface solar radiation in cloudy sky conditions for (a) July 14-16, 1999 and (b) June 22-23, 2000 and model simulations without and with cloud assimilation . . .	126
6.5	Scatter plots of daily-average modeled and observed surface solar radiation in cloudy sky conditions for (a) July 14-16, 1999 and (b) June 22-23, 2000 and model simulations without and with cloud assimilation . . .	127
6.6	Scatter plots of hourly-average modeled and observed surface solar radiation in clear sky conditions for (a) July 14-16, 1999 and (b) June 22-23, 2000 and model simulations without and with cloud assimilation . . .	128
6.7	Comparison between observed surface radiation fields and RAMS-derived values, with and without cloud assimilation, for (a) incoming short-wave radiation, and (b) incoming long-wave radiation on June 22-23, 2000 using the Chen/Cotton and the Harrington radiation schemes. In (b), the satellite-derived fractional cloud cover is also plotted . . . . .	132
6.8	Domain-average vertical temperature profiles during the night as modeled by RAMS with the Chen/Cotton and the Harrington schemes for (a) all levels and for (b) the lower model levels . . . . .	133
6.9	Scatter plots between the observed values and modeled values, with and without assimilation, of hourly averaged incoming long-wave radiation during the day for (a) the Chen/Cotton scheme and for (b) the Harrington scheme on June 22-23, 2000 . . . . .	134
6.10a	Comparison between observed precipitation and that calculated by RAMS with and without cloud assimilation for hourly intervals on July 14-16, 1999 at the AZMET sites in Southern Arizona. . . . .	138
6.10b	Comparison between observed precipitation and that calculated by RAMS with and without cloud assimilation for hourly intervals on July 14-16, 1999 at the AZMET sites in Southern Arizona. . . . .	139
6.11a	Comparison between observed precipitation and that calculated by RAMS with and without cloud assimilation for hourly intervals on June 22-23, 2000 at the AZMET sites in Southern Arizona. . . . .	140
6.11b	Comparison between observed precipitation and that calculated by RAMS	

	14
with and without cloud assimilation for hourly intervals on June 22-23, 2000 at the AZMET sites in Southern Arizona. . . . .	141
6.12 Scatter plots between observed and modeled (with assimilation) daily total, site-average precipitation for (a) July 14-16, 1999 and for (b) June 22-23, 2000 . . . . .	144
6.13 Time series of observed and hourly average modeled (with and without assimilation) precipitation averaged over all AZMET sites in model domain for (a) July 14-16, 1999 and for (b) June 22-23, 2000 . . . . .	145
6.14a Shows initial perturbations created from RUC surface-analysis and RUC 3-hr, 6-hr, 9-hr, and 12-hr forecasts and Eta surface-analysis for air temperature at the lowest model level on July 14, 1999 at GMT 00:00 . . .	148
6.14b Shows initial perturbations created from RUC surface-analysis and RUC 3-hr, 6-hr, 9-hr, and 12-hr forecasts and Eta surface-analysis for relative humidity at the lowest model level on July 14, 1999 at GMT 00:00 . . . . .	149
6.14c Shows initial perturbations created from RUC surface-analysis and RUC 3-hr, 6-hr, 9-hr, and 12-hr forecasts and Eta surface-analysis for compound wind speed at the lowest model level on July 14, 1999 at GMT 00:00 . . .	150
6.15a Results of domain average lowest model-level air temperature from five ensemble runs with RAMS coupled with cloud assimilation on July 14-16 1999 . . . . .	151
6.15b Results of domain average lowest model-level water vapor mixing ratio from five ensemble runs with RAMS coupled with cloud assimilation on July 14-16, 1999 . . . . .	152
6.15c Results of domain average lowest model-level compound wind speed from five ensemble runs with RAMS coupled with cloud assimilation on July 14-16, 1999 . . . . .	153
6.15d Results of domain average lowest model-level accumulated precipitation from five ensemble runs with RAMS coupled with cloud assimilation on July 14-16, 1999 . . . . .	154
6.15e Results of domain average lowest model-level incoming solar radiation from five ensemble runs with RAMS coupled with cloud assimilation on	

July 14-16, 1999 ..... 155

**LIST OF TABLES**

<u>Table</u>		<u>Page</u>
2.1	The options used in the Version 3b of RAMS model .....	38
2.2	Input parameters and their primary functions in the satellite algorithm .....	57
3.1	Information on the AZMET stations .....	62
3.2	The detailed information about sensors at AZMET .....	65
3.3	The main characteristics of the GOES Imager radiometer .....	72
6.1	RAMS-simulated with and without cloud assimilation and measured daily precipitation at AZMET sites for July 14-16, 1999 .....	142
6.2	RAMS-simulated with and without cloud assimilation and measured daily precipitation at AZMET sites for June 22-23, 2000 .....	143

## ABSTRACT

The goal of this study is to provide an improved, high resolution, regional diagnosis of three important surface variables on the land surface energy and water balance, namely the downward short-wave and downward long-wave surface radiation fluxes, and precipitation. Cloud cover is a key parameter linking and controlling these three terms. An automatic procedure was developed to derive high-resolution (4 km x 4 km) fields of fractional cloud cover from visible band, (GOES series) geostationary satellite data using a novel tracking procedure to determine the clear-sky composite image. In our initial data assimilation studies, the surface short-wave radiation fluxes calculated by RAMS were simply replaced by the equivalent estimated values obtained by applying this high-resolution satellite-derived cloud cover in the UMD GEWEX/SRB model. However, this initial study revealed problems associated with inconsistencies between the revised solar radiation fields and the RAMS-calculated incoming long-wave radiation and precipitation fields, because modeled cloud cover remained unchanged and, consequently, these other surface fields retained their low, clear-sky values. It was recognized that the UMD GEWEX/SRB model provides an important relationship between cloud albedo, cloud optical depth and cloud water/ice. Thus, exploration was made of feasibility of directly assimilating vertically integrated cloud water/ice fields to update modeled cloud cover. This approach will not only enhance the realism of radiation scheme in RAMS, but it may also dramatically increase the model's

capability to predict the location of precipitation, thus enhancing the ability of such mesoscale modeling systems to make accurate short-term forecasts of precipitation. This, in turn, would benefit flood forecasting as an associated hydrologic response. In the method adopted, the assimilated image takes the horizontal distribution of cloud from the satellite image but it retains a vertical distribution which is the area-average simulated by RAMS across the modeled domain in the time step immediately prior to cloud assimilation. Cloud assimilation is made every minute, with linear interpolation applied to derive cloud images for each minute between two GOES samples. Comparisons were made between modeled and observed data taken from the AZMET weather station network for model runs with and without cloud assimilation to demonstrate the improvement in RAMS' ability to describe surface radiation and precipitation fields. Cloud assimilation was found to substantially improve the RAMS model's ability to capture both the temporal and spatial variations in surface fields associated with observed cloud cover. The sensitivity of these comparisons to model initiation was explored by making five ensemble runs starting from different initiation. In general, RAMS with cloud assimilation technique is not sensitive to realistic perturbation of initial conditions.

## **CHAPTER 1**

### **INTRODUCTION**

#### **1.1 Introduction**

Remotely sensed data from satellite observations can provide unique information on the spatial and temporal distribution of many geophysical variables and the importance of these data has been demonstrated for many different applications. Satellite-based information is vital for understanding atmospheric properties, particularly those pertaining to cloud cover and its radiative properties, which is the main focus of the present study.

Clouds play a critical role in the Earth's hydrological cycle and in the energy balance of the climate system. They have a strong effect on solar heating by reflecting part of the incident solar radiation back to space. Clouds affect the thermal cooling by intercepting part of the infrared radiation emitted by the earth and atmosphere below the cloud, and re-emitting part of this radiation back to the surface. Global change in surface temperature is highly sensitive to cloud amount and type. Increasing low-level and mid-level clouds has a net cooling effect because they reflect more solar radiation and have a relatively small effect on infrared radiation. On the other hand, increased high clouds will have a warming effect by virtue of their low temperature and reduced cooling to space. Radiative fluxes, both at the top of the atmosphere and at the surface are the highest priority measurement necessary to understand the role of clouds in the climate system. The net radiation balance of these two fluxes is strongly influenced by the hydrological

and dynamical processes that directly control the precipitation rate. In this study, clouds provide the primary link between the two surface energy exchange processes that most influence climate, namely the exchange of short-wave and long-wave radiation and the exchange of water.

Numerous studies have explored the microphysics and dynamics of clouds at the scale of individual cloud elements (e.g., Pruppachear and Klett, 1980; Cotton and Anthes, 1989). Cloud optical properties (depth, size, phase, coverage, and height) can change quickly and over relatively small distances down to meters and they vary independently. Because of this, numerical weather prediction (NWP) models require detailed cloud parameterizations to represent the behavior of cloud processes in order to make reliable estimates of radiative fluxes and precipitation. However, it is generally recognized that inadequate parameterization of clouds is one of the greatest sources of uncertainty in the prediction of weather and climate. When dealing with cloud convective processes, this uncertainty is exacerbated by the great disparity between the spatial scale of observed clouds (typically 100 m to a few kilometers) and model grid scale (typically 40 to a few hundred kilometers). Derivation and/or parameterization of fine-scale cloud properties are required. Climate models When applied to the simulation of present climate, climate models produce markedly unrealistic surface fluxes of energy and water, and the fluxes must be supplement by prescribed, artificial “flux corrections” (e.g. Manabe et al. 1991). It has been stated that the primary reason for requiring surface energy flux corrections is that present-day climate models produce unrealistic simulations of the surface energy fluxes associated with solar and terrestrial radiation, and especially the modulations of

surface radiation by clouds. For example, the marine stratocumulus clouds that strongly reflect solar radiation away from the eastern sides of the subtropical oceans (e.g. Hanson 1991) are almost completely missed by many existing climate models. Small perturbations in the amount or radiative properties of these clouds could strongly affect the climate state (e.g. Randell et al. 1984; Slingo 1990). Failure to simulate these and other types of clouds is a major problem for existing climate models.

At the largest time and space scales, testing of climate models against global satellite observations and field data is inadequate, and diminishing confidence in their predictions of clouds, radiation and precipitation. Instead, cloud-scale and regional-scale models with more advanced cloud physics and radiation physics must be tested and incorporated with both field experiment data and satellite data. Once land-surface and atmosphere representations have been validated in these models, and shown to provide significant improvement, they can be transferred to global scale models.

The net available energy at the land surface is a key driver for regional climatology. It is particularly important to know the downwelling short-wave and long-wave fluxes, which are largely modulated by cloud cover. Additionally, there is increasing evidence of the linkages between a region's cloud climatology and its surface hydrometeorology (Wielicki et al. 1995). The rapid cycling of water in the coupled atmosphere/land-surface system, and the control on this cycling exerted by soil moisture, emphasize the importance of the hydrologic cycle to regional energy fluxes. To predict a region's climate and to give feedback for climate models, research focuses on the potential ability of a mesoscale model to aid diagnosis of the highly variable spatial

distribution of surface energy and water balances by assimilating satellite-derived cloud cover.

Measurements of the extent and of optical properties of clouds using Earth satellites have the potential to supplement surface observations. In this context, the International Satellite Cloud Climatology Project (ISCCP) was established by the World Climate Research Program (WRCF) in 1982 to collect and analyze satellite radiance data and, from this, to produce a uniform global cloud climatology (Schiffer and Rossow, 1983). Because clouds are very complex, available satellite data preclude the measurement of all the important properties of clouds. Nonetheless, it is assumed that cloud amount, cloud-top temperature, and optical thickness, which are the cloud properties that affect satellite-measured radiance most (Rossow and Garder, 1993a), are also the properties that most affect the total radiation balance. To maintain physical consistency, radiative transfer models are used to relate cloud properties both to satellite-measured radiance and to the complete radiation balance.

Modern satellites provide synoptic scale views of cloud fields taken at wide ranges of spectral bands and at high spatial and temporal resolutions. The Geostationary Observational Earth Satellites (GOES), for example, have 1 km spatial, 15 minute temporal, and 5 spectral resolutions. Data assimilation has been recognized as an important tool not just for providing initial conditions for numerical model prediction but also for improving model diagnostic/prognostic fields (Bengtsson et al. 1988). In recent years, progress has been made in controlling model error through assimilation of wind and temperature observations, but corresponding progress has been lacking in

assimilating cloud cover. Thus, in the research described in this thesis, a technique was developed to assimilate fine-scale information on cloud cover provided by GOES visible imager in a coupled hydrology and mesoscale model to produce improved description of surface exchanges.

## **1.2 Problem Definition**

Cloud cover is a key parameter linking and controlling downward components of short-wave and long-wave surface radiation and precipitation on the land surface energy and water balance, yet, as described above, the specification of cloud cover in regional coupled atmosphere-land surface models is among the largest sources of uncertainty. On the other hand, hydrologists are now actively using the currently available high-resolution land cover, topography, soil and vegetation characteristics data sets (1 x 1 km) to parameterize distributed hydrologic models and to couple these models with regional atmospheric models. Adequate evaluation and optimal use of these coupled models will depend on the accurate estimation of fine-resolution surface variables (4 x 4 km). These estimated-fields can also reduce the great uncertainty in model initialization of soil moisture that is crucial to the atmospheric modeling, especially to those physical processes, which are related to atmospheric moisture and precipitation.

Mesoscale atmospheric models predict clouds, but only in a highly parameterized manner, thus causing model estimates of spatial distributions and radiative characteristics to be subject to considerable error. RAMS, one of these models applied in research of this type, demonstrates uncertainty based on comparison between model results and

observations, although on clear days the model output agreed reasonably well with the observed data. The inconsistencies arise on cloudy days in areas that are modeled by RAMS as being cloud free, when the model compares poorly with observations. For instance, downward short-wave fluxes assume relatively high, clear-sky values, while downward long-wave fluxes retain their relatively low, clear-sky values, rather than the higher values appropriate to cloud covered areas (clouds behave as near black-bodies emitting radiation according to the temperature of their base). In semi-arid areas such as Southern Arizona-- the area used in this study-- the difference in long-wave radiation between cloud-free and cloud-covered areas can easily exceed  $100 \text{ W/m}^2$ . A further important inconsistency is that RAMS generally underestimates precipitation in spite of using detailed parameterization schemes for clouds and precipitation. This may in part be due to RAMS using inaccurate model re-initialization fields and domain boundary forcing and, more importantly, a modeled atmospheric boundary layer in which latent heat flux is easily curtailed by soil moisture stress, with sensible heat becoming the dominant energy flux over the semi-arid land.

The present research is focused on correcting the modeled cloud cover in RAMS, thus allowing the RAMS radiation and precipitation codes to calculate the actual spatial variability generated by the observed clouds. It recognizes that satellite remote sensing is an innovative and powerful technique to improve weather simulated from such models. Therefore, fine-scale cloud cover, derived from satellite observations, is assimilated into RAMS to aid diagnosis of surface energy and water exchanges. The potential benefits of this approach are tremendous. It will not only enhance the realism of radiation scheme in

the model, but it may also dramatically increase the model's capability to predict the location of precipitation fields, thus enhancing the ability of such mesoscale modeling systems to make accurate short-term forecasts of precipitation. This, in turn, would benefit flood forecasting (especially flash flood forecasting) as an associate hydrologic response. High spatial resolution flood forecasting is crucial because in some regions, such as areas in deserts, near mountain ranges, and in coastal zones, weather conditions can vary much over short distances and floods can cause severe damages and even loss of human life.

### **1.3 Historical Overview**

For many years, the primary purpose of data assimilation has been to provide initial conditions for numerical weather predictions. More recently, data assimilation has been recognized as an important tool for climate and earth system studies. Several fields (precipitable water, water vapor, precipitation, wind, temperature, and some cloud parameters) are assimilated into numerical models to improve model results.

Lipton (1993) developed and applied a retrieval-assimilation method by means of which the effect of cloud shading on surface radiation budgets is estimated from satellite imagery along with numerical model parameters. This model-satellite coupled analysis system merges information from visible image data in cloudy areas with infrared sounder data in clear areas. Retrievals of surface temperatures and water vapor concentrations are assimilated. Data from GOES visible-imager and the atmospheric sounder are used in different part of the system. The numerical model used in the coupled system is a

hydrostatic version of the Colorado State University Regional Atmospheric Modeling System (RAMS) with a terrain-following coordinate system (Mahrer and Pielke 1977; 1978). Merging satellite retrievals with model products is accomplished by adjusting model products with the satellite retrievals. For example, by employing simple radiative transfer models, visible image data from GOES are used to retrieve the clouds' effective solar transmittance and infrared emittance. These parameters, along with other relevant parameters computed by the RAMS, control the model's computation of downward radiation fluxes at the ground under cloudy condition during four-dimensional data assimilation. Modeled surface temperatures are controlled by these radiative fluxes. RAMS performs the interpolation of retrieved cloud parameters between satellite image observation times. A case study in the northwestern Texas demonstrated the impact of this method in the RAMS model. The analysis system including shading retrieval technique accounted for the shading effect of a persistent region of stratiform cloud cover and produced consistently smaller height-temperature errors than analyses without shading retrievals. The research was applied for stratiform cloud types because the retrieval of radiation parameters used in the assimilation are appropriate for relatively thin clouds.

Lipton and Modica (1999) made further application for the assimilation method originally applied by Lipton (1993) to make a short-term forecast from the initiate, assimilated values. They adjusted humidity fields to improve forecast reliably using only data from the GOES visible-imager. The adjustment of humidity fields is required for the model to make better forecasts because there is a tendency for the model to lose

information provided during assimilation unless satellite-derived forcing is maintained because of the influence of boundary conditions (Vukicevic and Paegle 1989). In this study, assimilation of satellite data was made using the National Center for Atmospheric Research-Pennsylvania State University Mesoscale Model 4 (MM4) Version 8. The assimilated values of cloud solar transmittance and infrared emittance are derived from satellite data using a simple radiative transfer model. These values are averaged to the model grid resolution before assimilation. This study also applied to stratiform clouds, which are important initiator of convective cloud development. MM4 diagnoses clouds from the relative humidity distribution in model layers, and humidity changes with cloud fraction across the model grid. Infrared emittance is used on determining cloud-top height, while cloud-base height is determined using pseudoadiabatic ascent based on the liquid water amount derived from satellite. The assimilation retrieval assumed that the cloud mass fraction can be calculated by from the cloud thickness between these elevations. The adjustment to the humidity field is applied using the cloud mass fraction values in each layer. The satellite-derived effective transmittance used in model radiation parameterization is also necessary for the short-term forecast run. Results of a case study involving both for both analysis and forecast runs show that model run with assimilation is significantly better than the model run without assimilation. One important result from this study is that forecast experiments, starting from analysis, run with assimilation, benefit from model parameter tuning. This is not unreasonable in longer-term forecasts.

Ruggiero et al. (2000) developed an assimilation system to improve the diagnosis of convective initiation due to differential cloud shading. They hypothesize that one of

the primary drivers of locally forced convection is differential surface heating due to the differential cloud shading, which causes perturbations to the wind field that result in local areas of convergence. High spatial-resolution information is needed to introduce this into numerical model (MM4). In their study, Ruggiero et al (2000) introduced the assimilation of hourly surface observations in addition to the assimilation of GOES visible-imager data. The retrieval-assimilation method described Lipton (1993) and Lipton and Modica (1999) was again applied for the satellite data. However, the study only considered analysis runs, so humidity adjustment was not applied. Ruggiero et al (2000) conclude that the model run with assimilation shows improved depiction of the effect of modified surface heating beneath cloud, as well as of mass and moisture convergence and convective available potential energy in both cloudy and adjoining regions.

Review of the literature shows that use of retrieved satellite information in meteorological models has hitherto been limited to assimilating the effective transmittance of solar radiation to investigate the direct effect on surface heating. Direct assimilation of satellite-derived cloud water/ice into these models has not previously been attempted in spite of the fact that cloud cover is itself a major control on the atmospheric and surface fields.

#### **1.4 Research Objectives**

The main goal of the research described in this thesis is to provide an improved, high-resolution regional diagnosis of three of the important controls on the land surface energy and water balance, namely the downward short-wave and downward long-wave

surface radiation fluxes, and precipitation. It is envisaged that improving these surface fields will enhance the ability of a mesoscale modeling system to produce accurate short-term forecasts. As previously mentioned, cloud cover is clearly a key parameter linking and controlling these three terms, and it is also one of the largest sources of uncertainty in models. Hence, the overall objective of the study is to develop, apply, and evaluate a method that involves assimilating satellite-derived, fine-resolution cloud cover into the RAMS model.

In pursuit of the above goal and objective, the first task (and objective) was to set up RAMS so that it runs reliably in a domain that comprised the semi-arid region of interest in southern Arizona. The model domain covered an area of 400 km x 400 km at 4-km resolution, centered on (33.25 N, -111.7 W). RAMS is initiated and then nudged every 6 hours by the atmospheric fields that are routinely synthesized by a regionally-appropriate mesoscale model, specifically the National Center for Environmental Predictions (NCEPs) version of the Eta model. These atmospheric fields are obtained via the Internet.

The second task (and objective) was to acquire satellite data for a period in which there was significant cloud amount, and for which Eta forcing fields were available every 6 hours and GOES images available during daylight hours every 15 minutes. For this study, the satellite data were from the GOES visible channel for a 3-day period, 14-16 July 1999, and for a 2-day period, 22-23 June 2000. GOES (series 9 and 10) data at 1-km resolution are routinely available via the Internet. This task also included analyzing and

quality controlling the satellite data by filtering any random noise in the satellite images.

Noisy lines in the images are filtered and replaced by the nearby good lines.

The third task (and objective) was to develop an automatic procedure to derive high-resolution (4-km x 4-km) fields of cloudy sky radiance and clear sky radiance from visible band of GOES data. This procedure is an extension of the method used by Garatuza et al. (2000), but differs in that the method used a novel, real-time tracking procedure to determine the required clear sky composite image. The radiances and cloud fraction from this procedure can be used in the University of Maryland (UMD) GEWEX Solar Radiation Based (SRB) model to calculate surface downward short-wave radiation fluxes.

Initial data assimilation studies revealed problems when assimilating estimates of surface radiation derived from satellite using the UMD GEWEX/SRB model. Doing this creates inconsistencies in RAMS-calculated surface fields because the cloud cover remains unchanged. Thus, these initial studies demonstrated the need to address a fourth objective, namely to develop a method by way of which satellite-derived cloud water/ice can be assimilated into the RAMS model. The cloudy sky, clear sky, and composite radiances, and cloud fraction used in UMD GEWEX/SRB model are related to cloud albedo, cloud optical depth, and cloud water/ice. This relationship was used to derive an estimate of the vertically integrated cloud water/ice that was directly assimilated into the RAMS model to update the modeled cloud cover. With this method, the assimilated image obtains its horizontal distribution of cloud from the satellite image but it retains a

vertical distribution which is that given by RAMS along atmospheric columns in the modeled domain.

The fifth task (and objective) was to perform model runs with and without cloud assimilation, and to obtain and process relevant model fields from these runs to evaluate the resultant cloud fields against satellite images and to compare the model calculated surface fields against observed data. A 17-site network of automatic weather stations, Arizona Meteorological Network (AZMET), was used to provide the observed data at 1-hour intervals. Since measurements of downward long-wave radiation fluxes were not available from AZMET, a radiometer from Kipp & Zonen Company was purchased and deployed at an experiment site in Tombstone, Arizona. Data collection with this instrument started on June 15, 2000, so data were available for the 2-day study period (June 22-23, 2000) of model run. Model runs with cloud assimilation were performed using different assimilation frequencies (e.g. 30 minute, 15 minute and every minute). The results showed that there is substantial improvement in modeled horizontal distribution and the overall cloud amount when satellite data are assimilated, and that assimilation improved the accuracy of the model-derived radiation and precipitation fields at the AZMET sites.

The final task (and objective) was to make ensemble runs with RAMS coupled with the cloud assimilation technique. The purpose of these runs was to investigate the relevant to which runs with cloud assimilation are sensitive to initial conditions. Five ensemble runs were performed using initiations from surface-analysis and 3-hour, 6-hour, 9-hour, and 12-hour forecast of Rapid Update Cycle (RUC) model. Each set of data

coincided with the initialization time of the RAMS runs. The results showed that model runs with cloud assimilation are not sensitive to initial conditions, and that all the runs tend to converge within a few hours of initiation.

## **1.5 Summary of Dissertation**

This dissertation is organized into seven chapters as follows:

Chapter 1, the present chapter, provides an introduction to the study and a problem definition and specifies the objectives of this research along with a brief historical review of previous attempts to assimilate satellite data into meteorological models. Chapter 2 provides describes the nature and structure of the RAMS and UMD GEWEX/SRB models. The description of the RAMS model puts emphasis on the surface layer, microphysics and radiation parameterization schemes, while that of the UMD GEWEX/SRB model emphasizes surface albedo and surface irradiance retrievals. Chapter 3 describes the sources of the data used in this study. Chapter 4 presents the methodology for the cloud screening algorithm and describes the application and evaluation of this algorithm. Chapter 5 describes how satellite data are assimilated into the RAMS model. It first describes our initial attempts to assimilate solar radiation fields, and then describes the methodology and the application of the assimilation of cloud water/ice fields. Chapter 6 gives the results of the comparison between model runs with and without cloud assimilation and observed data. Chapter 7 summarizes the study, gives the main results, and draws conclusions.

## **CHAPTER 2**

### **MODELS**

#### **2.1 Introduction**

In this study, the Regional Atmospheric Modeling System (RAMS) coupled with the Land Surface Model (LSM) is used to simulate simultaneous observations of the atmosphere and land surface hydrologic and energy exchanges, while the UMD GEWEX/SRB model is applied to estimate variables from satellite observations for use in atmospheric model. The following sections describe the nature and structure of the RAMS and UMD GEWEX/SRB models with emphasis on those parts most relevant to the research.

#### **2.2 Description of the Version 3b of the RAMS Model**

The RAMS model is a comprehensive mesoscale meteorological modeling system which was developed at Colorado State University in order to simulate and forecast meteorological phenomena in a very wide range of scales (thousands of km to the microscale). It is a three-dimensional, nonhydrostatic system (Tripoli and Cotton 1980) consisting of equations of motion, heat, moisture, and mass continuity in a terrain-following coordinate system (Pielke et al. 1992). Comprehensive testing, tuning and development of the RAMS representation of surface-atmosphere interactions and of atmospheric convection and radiation processes has been carried out in many applications (Tripoli and Cotton 1982; Chen 1983; Tremback et al. 1985; Pielke et al. 1992; Nicholls

1995; Walko et al. 1995a). These studies demonstrated that RAMS was able to construct the atmospheric circulation and structure at various scales and was able to solve the fundamental dynamical and thermodynamical equations of the atmosphere without the hydrostatical approximations. The model includes the feature of telescoping interactive nested grids (Clark and Farley 1984; Walko et al. 1995b) and various alternative turbulent closure schemes (Deardorf 1980; McNider and Pielke 1981; Tripoli and Cotton 1986) and initialization (Tremback 1990) and boundary condition schemes (Pielke et al. 1992).

The RAMS horizontal grid is configured in a rotated latitude-longitude framework (i.e. polar-stereographic projection), where the pole of the projection is rotated to near the center of simulation domain, thus minimizing the distortion of the projection in the main area of interest. The vertical grid uses the terrain-pursuing sigma ( $\sigma_z$ ) coordinate system (Clark, 1977; Tripoli and Cotton, 1982). The sigma-z coordinate is defined by the relation

$$\sigma_z = H \left( \frac{z - z_g}{H - z_g} \right) \quad (2.1)$$

where  $H$  is the height of the top of the domain and  $z_g$  is local topography height. Sigma coordinates are pressure based and are normalized from the top of the domain (TOD) to the ground. Figure 2.1 illustrates the sigma coordinate framework. The coordinate system identifies vertical position in the atmosphere relative to a fundamental base and the TOD, and varies from zero at the TOD to unity at the base which is at the modeled ground surface in this system. In Figure 2.1,  $P1$  and  $P2$  have the same elevation relative to Mean

Sea Level (MSL), but  $P1$  is at ground level (e.g. at the top of a mountain), while  $P2$  is in the free atmosphere. The sigma value at  $P1$  is unity, while that at  $P2$  it less than one. Surface pressure at ground level (below these points) minus pressure at the TOD is very different. Hence, the sigma coordinate surfaces follow the model terrain and are sloped in regions where the topography is sloped.

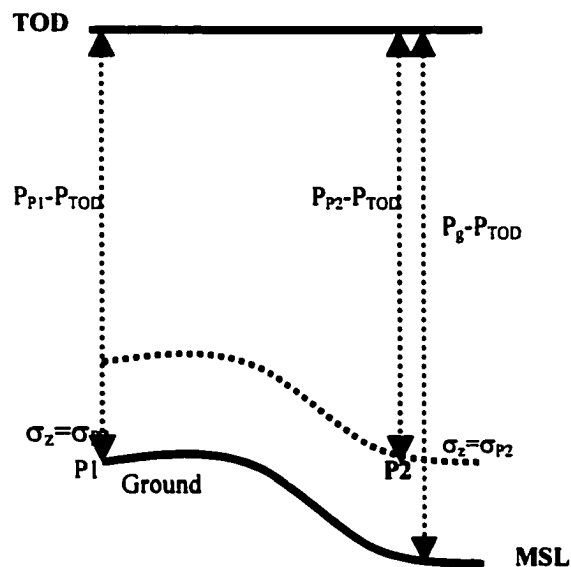


Figure 2.1 The sigma coordinate framework

The horizontal domain of the model is defined on the staggered Arakawa-C grid (Arakawa and Lamb 1977). The horizontal and vertical components of wind ( $u$ ,  $v$  and  $w$ ) are specified at points which are staggered one-half a grid length in the  $x$ ,  $y$  and  $z$  directions, respectively, from the grid used for thermodynamic, moisture, and pressure variables. The number of vertical levels in the model is user dependent. In this study, the RAMS used 28 levels, with a corresponding model top height of 23 km. The model uses

a geometrically-stretched grid between consecutive levels so that it obtains high vertical resolution near the ground and lower resolution at higher levels. Most of the 3-D atmospheric variables are layer averages, which are taken to be representative of the middle of the layer. An input file is available in the model that contains namelist data to specify many aspects of the model configuration and options. The file also contains numerous data used in initializing atmospheric, soil, and vegetation fields and controlling physical parameters.

The lower boundary condition in the RAMS is provided by a prognostic soil and vegetation model which interacts with the modeled atmosphere. Each grid area in the RAMS is divided into three different classes, namely water, bare soil, and vegetated surfaces. The surface layer parameterization requires surface temperature and moisture values for all three classes. For bare soil, RAMS uses the multi-layer soil model described by Tremback and Kessler (1985). For the vegetated surface, it uses the “big leaf” approach with a layer of vegetation overlying a shaded soil (Avissar and Mahrer 1988). The RAMS uses 18-vegetation classifications and the parameters defined for each class include the vegetation albedo, emissivity, roughness height, displacement, fractional coverage, and leaf area index which are taken from the Biosphere-Atmosphere Transfer Scheme (BATS). Once the temperatures and effective moisture values for each surface categories have been calculated, the surface-layer fluxes of heat, momentum, and water vapor are computed using the method of Louisie (1979, 1982). The fluxes are then averaged to provide the grid-area average fluxes that are applied to the atmosphere.

A nudging type four-dimensional data assimilation (4DDA) scheme was implemented in the RAMS model to provide lateral boundary conditions. By using this scheme, the model introduces time-varying information into the modeled domain while damping out information propagating from the model interior towards the lateral boundaries. In this research, an alternative procedure, not the standard Isentropic Analysis (ISAN) package, was developed and used to generate variable initialization files and time-dependent lateral boundary conditions for RAMS model. This procedure interpolates the NCEP Eta model (AWIPS Grid 212) atmospheric fields directly from the Eta levels to the RAMS sigma-z levels. This relies on the horizontal interpolation of the AWIPS grid to the intermediate latitude-longitude grid, with a subsequent horizontal interpolation to the RAMS grid, and vertical interpolation, initially from pressure levels to isentropic levels, with subsequent vertical interpolation to the RAMS sigma-z levels. The Eta model fields at 40-km horizontal resolution are interpolated to the RAMS grid at 4-km resolution. Table 1 summarizes the options of Version 3b of the RAMS model that were applied in this study.

Table 2.1: The options used in the Version 3b of RAMS model.

Category	Options Used	References
Basic equation	Nonhydrostatic; compressible	Tripoli and Cotton (1980)
Vertical coordinates	Terrain-following sigma z	Clark (1977); Tripoli and Cotton (1982)
Horizontal coordinates	Oblique polar-stereographic projection	
Grid stagger	Arakawa C grid	Arakawa and Lamb (1977)
Time differencing	Hybrid	
Stable precipitation	Explicit microphysics	Cotton et al. (1995)
Convective Parameterization	None	
Radiation	Harrington	Harrington (1997)
Cloud	Explicit microphysics, condensation	Cotton et al. (1995)
Surface layer	Louis	Louis (1979, 1982)
	Prognostic soil model	Tremback and Kessler (1985)
	Vegetation parameterization	Avisar and Mahrer (1988)

### 2.2.1 Microphysics Parameterization

The RAMS uses the explicit cloud microphysical model originally developed by Cotton et al. (1986). To provide improvements to the cloud model physics and numerical scheme, this model was applied in a range of weather and geographical conditions (Manton and Cotton, 1977; Cotton and Tripoli, 1978; Meyers et al. 1991; Meyers and Cotton, 1992). One of the important improvements deriving from these studies is the parameterization of the ice phase in the cloud model. The dynamics and microphysics of convective clouds and mesoscale cloud systems can be simulated efficiently if the ice phase is incorporated into the numerical models because the freezing of water drops and the deposition of water vapor onto ice particles both contribute to latent heat release that enhances cloud growth. Furthermore, because ice particles fall at higher terminal velocities, they can play a dominant role in altering the distribution of total water and, subsequently, the formation and extent of downdrafts as well as the amount of precipitation at the ground.

In the model, the cloud microphysical variables are described in physical terms as a mixing ratio (or content), which is the ratio of the mass of the water species to mass of dry air. The total water,  $r_T$ , in the cloud is given by

$$r_T = r_v + r_c + r_r + r_p + r_g + r_h + r_a + r_s$$

or

$$r_T = r_v + r_l + r_{ice}$$

where

(2.2)

$$r_l = r_c + r_r$$

$$r_{ice} = r_p + r_g + r_h + r_a + r_s$$

In above equations,  $r_v$ ,  $r_c$ ,  $r_r$ ,  $r_p$ ,  $r_g$ ,  $r_h$ ,  $r_a$ , and  $r_s$  are the mixing ratios of water vapor, cloud water, rain water, pristine, graupel, hail, aggregate, and snow species, respectively. The mixing ratio of liquid water,  $r_l$ , in the model is given by the sum of cloud water and rain water, while the mixing ratio of the ice phase,  $r_{ice}$ , is calculated by the sum of pristine, graupel, hail, aggregate, and snow water. Cloud water, water vapor, potential temperature, air temperature, and pressure are derived diagnostically from the prognostic values of ice-liquid water potential temperature ( $\theta_{il}$ ), dry air density, total water, rain water, and ice water. At temperatures warmer than the homogeneous ice nucleation temperature ( $T_H = 233.16$  K), cloud water and water vapor mixing ratios are diagnosed as

$$r_c = \begin{cases} MAX(r_T - r_r - r_{ice} - r_{vs}, 0) & T > T_H \\ 0 & T \leq T_H \end{cases} \quad (2.3)$$

and

$$r_v = \begin{cases} r_{vs} & T > T_H \\ MAX(r_T - r_r - r_{ice}, 0) & T \leq T_H \end{cases} \quad (2.4)$$

where  $r_{vs}$  is the saturation vapor mixing ratio with respect to water.

At temperatures below  $T_H$ , it is required that all liquid water freezes (the model assumes zero supersaturation with respect to ice), thus

$$r_{ice} = \begin{cases} r_{ice} & T > T_H \\ r_{ice} + MAX(r_T - r_r - r_{ice} - r_{vs}, 0) & T \leq T_H \end{cases} \quad (2.5)$$

Along with the thermodynamic equations (the Poisson equation, the ideal gas law, and combination of these two), the microphysics equations comprise a diagnostic set which is solved using iterative techniques for pressure, potential temperature, temperature, cloud water and water vapor mixing ratios from predicted values of air density,  $\theta_i$ , total water and ice water mixing ratios at a given time. The time-dependent mass continuity equations, including the advective, diffusive, and source and sink terms, are applied for each of the prognostic variables. The time-dependent conservation equations, together with the diagnostic equation set in the model, make up a closed system to be solved numerically given proper boundary conditions and initial conditions. The source and sink terms describing the various rates of conversion of water substance between its phases and hydrometeor types are defined by the letters AC for accretion, CN for auto-conversion, NU for nucleation, ML for melting, FR for freezing, CL for collection, VD for vapor deposition or evaporation, RM for riming and PR for precipitation. In Figure 2.2, the various physical processes that are considered in ice phase parameterization are summarized.

Cloud droplets are assumed to have negligible terminal velocity and evaporate and condense instantaneously, with zero supersaturation. The mixing ratio of cloud droplets is initially converted to raindrops using a parameterization of cloud droplet collection described by Tripoli and Cotton (1980). Once raindrops form, they can accrete cloud droplets, evaporate, precipitate or interact with ice particles. Ice crystals are considered pristine individual crystals that are not highly rimed. They are initiated naturally from a specified concentration of activated ice nuclei. On the other hand, graupel particles,

which are highly rimed ice crystals, are frozen raindrops. As the graupel mixing ratios increase, the mass of individual graupel particles may reach a sufficient size that they are considered hail. The ice parameterization predicts the changes in ice crystal (pristine) mixing ratio by vapor deposition and riming growth of ice crystals, as well as melting. The parameterization also predicts the changes in graupel mixing ratio due to vapor deposition, conversion of ice crystals into graupel, riming growth of graupel, supercooled raindrops collecting ice crystals and freezing, graupel particles collecting supercooled raindrops, melting of graupel, and precipitation. The surface precipitation in the model can occur in the form of rain and ice (graupel, hail, snow, pristine, and aggregate). The latter form is likely to be predicted only when the surface and lower atmosphere temperatures are colder than 0°C.

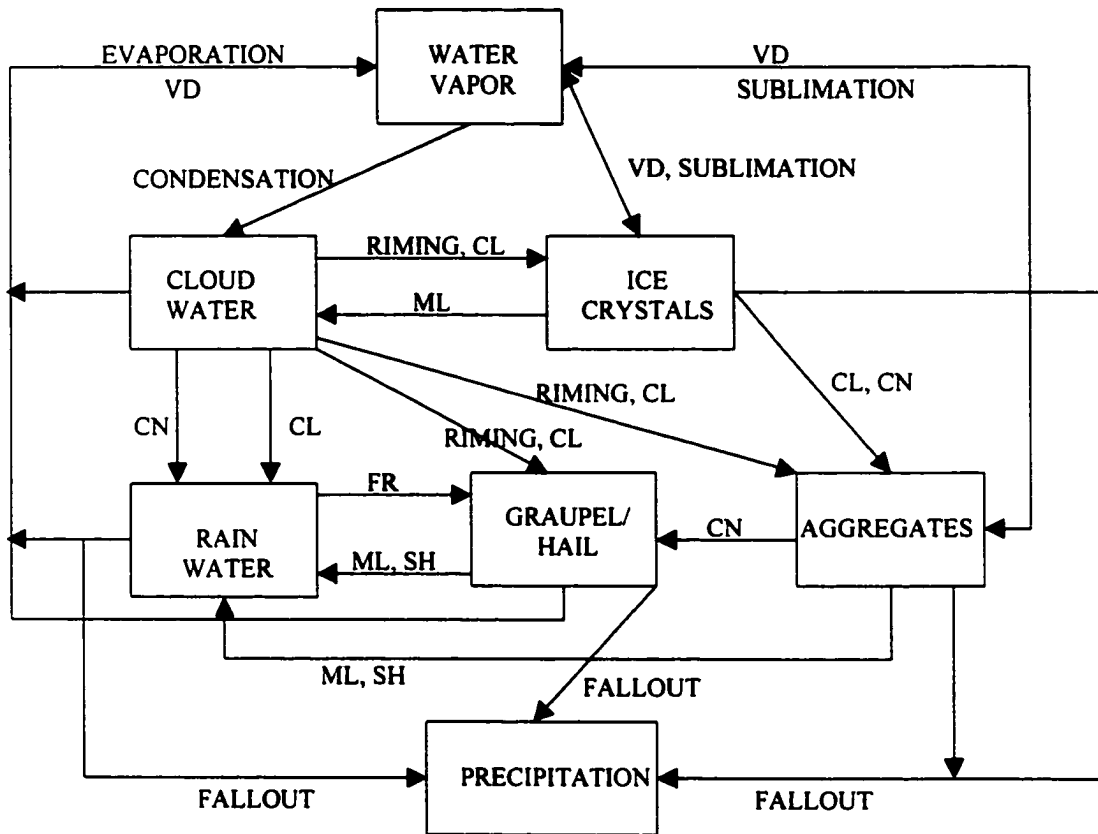


Figure 2.2 Flow diagram illustrating the microphysical processes considered in the model.

### 2.2.2 Radiation Parameterization

Version 3b of the RAMS model allows two options for the long-wave and two options for the short-wave radiation parameterization. The first options, which are taken from Mahrer and Pielke (1977), are simple and their use involves relatively little computational expense. However, these radiation schemes do not include the radiative effects of liquid water or ice. The second options, those used in this research, activate a

scheme developed by Chen and Cotton (1983). This scheme is more expensive computationally than that of Mahrer and Pielke to run, but it takes into account the radiative effects of liquid water and ice. The Chen/Cotton short-wave radiation scheme has 3-band accounting for molecular scattering, absorption in clear air (Yamamoto, 1962), ozone absorption (Lacis and Hansen, 1974), and reflectance, transmittance and absorptance by a cloud layer (Stephens, 1978) in a clear-cloudy, mixed layer approach (Stephens, 1977). The Chen/Cotton long-wave radiation scheme includes the emissivity of the clear atmosphere (Rodgers, 1967), emissivity of cloud layer (Stephens, 1978), and emissivity of a clear-cloudy mixed layer (Herman and Goody, 1976). The cloud water and ice at each level in the atmospheric column is obtained by extracting the water vapor mixing ratio from the total water mixing ratio (Equation 2.2), and the cloud optical depth is derived using an empirical equation derived by Stephens 1978, 1984. The routine partitioning of short-wave radiation is determined simply, by interpolation from a multidimensional lookup table that is pre-calculated for fixed intervals of the input variables (cloud optical depth, solar zenith angle, spectral band, total ozone and water vapor absorption). The long-wave radiation fluxes at the surface are estimated using efficient emissivity approximation at each level in the atmospheric column through surface layer.

However, our initial investigations showed that the Chen and Cotton radiation scheme has deficiencies when calculating downward short-wave radiation. With the Chen/Cotton scheme, calculated surface radiation is usually very low whenever RAMS diagnoses cloud, as illustrated in Figure 2.3a. Accordingly, this radiation scheme was

replaced with the improved scheme of Harrington (1997) that uses an 8-band, two-stream radiation transfer code. The Harrington scheme generated much better spatial patterns of incoming solar radiation as shown in Figure 2.3b. The scatter plots for the two schemes shown in Figure 2.3c clearly demonstrates that the Chen/Cotton radiation scheme has shortcomings when the clouds are diagnosed by the model.

The two-stream radiative transfer model in the Harrington radiation scheme includes the effects of clouds characterized by highly anisotropic scattering, mixes of Rayleigh scattering, aerosol scattering and molecular absorption, absorption by selected greenhouse gasses, and the complex effects of cloud geometry. At each layer which scatters, absorbs and emits radiation, the radiative fluxes are calculated and then summed to derive surface fluxes. The forms of the source functions considered in the two-stream transfer scheme are those of the Eddington approximation, namely:

$$t = \sigma_{ext} \frac{7}{4} - \frac{\sigma_{sca}}{4} (4 + 3g) \quad (2.6)$$

$$r = -\sigma_{ext} \frac{1}{4} + \frac{\sigma_{sca}(4 - 3g)}{4}$$

and source vectors are derived from

$$Q^+ = \frac{\sigma_{sca}}{4} (2 - 3g\mu_0) \quad (2.7)$$

$$Q^- = -\frac{\sigma_{sca}}{4} (2 + 3g\mu_0)$$

where (+) and (-) signs describe upwelling and downwelling vectors, respectively,  $g$  is the asymmetry parameter,  $\theta_0$ , the solar zenith angle ( $\mu_0 = \cos(\theta_0)$ ),  $\omega_0 = \sigma_{sca} / \sigma_{ext}$  the single scatter albedo and  $\sigma_{ext} = \sigma_{sca} + \sigma_{abs}$  is the volume extinction coefficient (optical depth) with  $\sigma_{sca}$  and  $\sigma_{abs}$  the volume scattering and absorption coefficients, respectively. The two-stream solutions are therefore defined by 5 parameters, namely  $\sigma_{sca}$ ,  $\sigma_{abs}$ ,  $g$ ,  $\theta_0$ , and geometric thickness of the layer. The total optical depth ( $\sigma_{ext}$ ) at each layer is the sum of the gaseous optical depth, the Rayleigh optical depth, and the cumulative hydrometeor optical depth. The cumulative hydrometeor optical depth,  $\tau_{au}$ , is calculated by the sum of extinction coefficients of each microphysical cloud water/ice fields given in the Equation 2.2, as follows:

$$\tau_{au} = \sum_{i=1}^7 \sigma_i \quad (2.8)$$

where

$$\sigma(i) = m(i) * bc1 * r(i)^{bc2} * dz$$

where subscript  $i$  refers to each hydrometeor type,  $m$  is hydrometeor concentrations (# /  $m^3$ ),  $bc1$  and  $bc2$  are extinction fit coefficients,  $r$  is the characteristic diameter (m), and  $dz$  is the thickness of the level.

Accordingly, the cumulative single scattering albedo,  $\omega_{mgs}$ , is obtained as follows

$$\omega_{mgs} = \sum_{i=1}^7 \omega_i * \sigma_i \quad (2.9)$$

where

$$om(i) = oc1 + oc2 * \exp(oc3 * r(i)) + oc4 * \exp(oc5 * r(i))$$

where  $oc1$ ,  $oc2$ ,  $oc3$ ,  $oc4$  and  $oc5$  are the scattering albedo fit coefficients. Finally, the Harrington radiation scheme calculates the cumulative asymmetry parameter from the definition:

$$gp = \sum_{i=1}^7 gg_i * om_i * \sigma_i \quad (2.10)$$

$$gg(i) = gc1 + gc2 * \exp(gc3 * r(i)) + gc4 * \exp(gc5 * r(i))$$

where  $gc1$ ,  $gc2$ ,  $gc3$ ,  $gc4$  and  $gc5$  are the asymmetry fit coefficients.

Unlike the Chen/Cotton radiation scheme, the Harrington radiation scheme considers each individual microphysical variable separately in the calculation of cloud radiative properties.

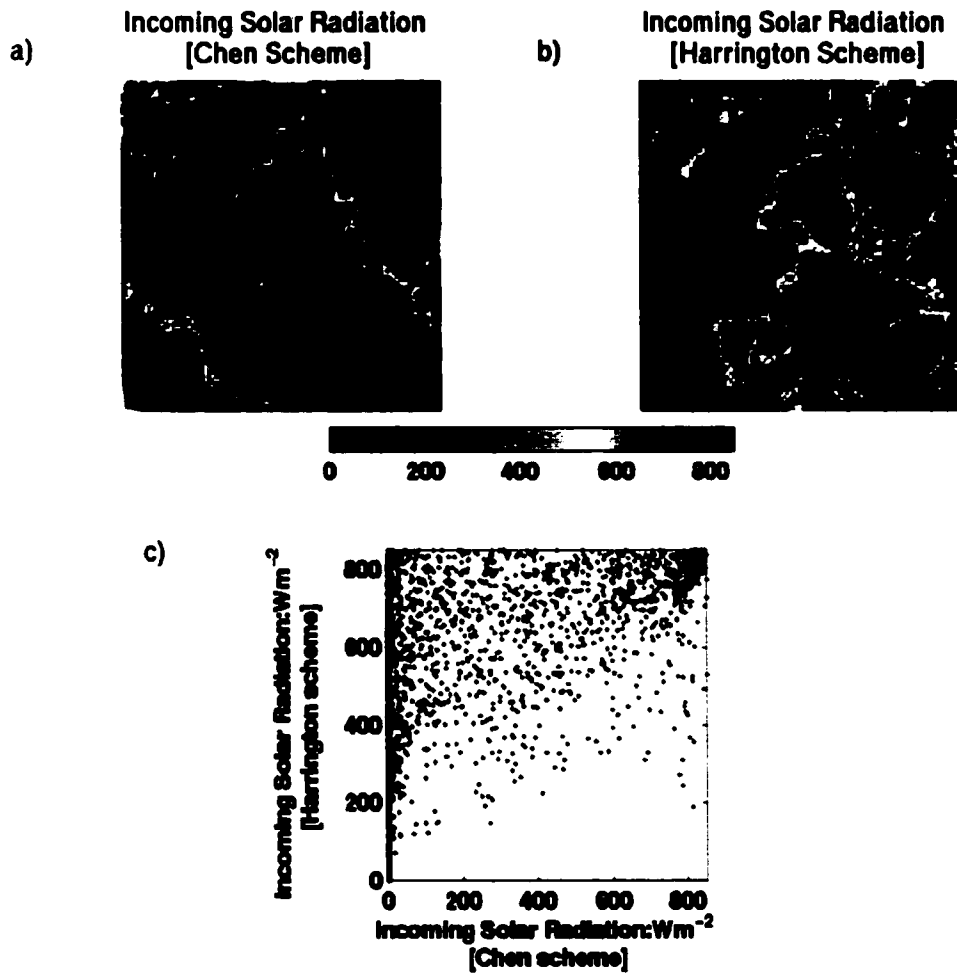


Figure 2.3 (a) The spatial patterns of incoming solar radiation for the Chen/Cotton scheme and (b) for the Harrington scheme. In (c) the scatter plot of two schemes is illustrated.

## 2.3 Description of the UMD GEWEX/SRB Model

### 2.3.1 Radiative Transfer Technique

The UMD GEWEX/SRB model is based on application of the model introduced and developed by Pinker and Ewing (1985) and by Pinker and Lazslo (1992). In this model, the Delta-Eddington two-stream technique is used to describe radiative transfer through a three-layer (0 – 2 km, 2 – 5.5 km and 5.5 – top of the atmosphere) model atmosphere, the middle layer being a cloud layer, which is assumed homogeneous. The calculations are made in the visible spectrum 0.3 to 0.7  $\mu\text{m}$  for four spectral intervals (0.3 – 0.4, 0.4 – 0.5, 0.5 – 0.6 and 0.6 – 0.7  $\mu\text{m}$ ), and in the region 0.7 – 4  $\mu\text{m}$  for eight spectral intervals. The latter is based on a discrete probability distribution of water vapor coefficients (Lacis and Hansen, 1974). In this technique, the values of optical thickness ( $\tau$ ), single-scattering albedo ( $\omega$ ) and an asymmetry factor ( $g$ ) required for each model layer and spectral interval are parameterized for Rayleigh scattering, water vapor absorption, aerosol absorption and scattering, and cloud absorption and scattering, as appropriate. Ozone absorption is allowed for by reducing the incident solar flux in relevant spectral intervals. These variables are determined by the following equations:

$$\tau = \sum \tau_i ; \quad \omega = \sum \frac{\omega_i \tau_i}{\tau} ; \quad g = \sum \frac{\omega_i \tau_i g_i}{\omega \tau} ; \quad (2.11)$$

where the subscript  $i$  refers to the above radiative constituents at each layer and each interval.

The aerosol parameterization follows the approach of Leighton (1979), which assumed a haze-C distribution of aerosols and used Mie theory calculations to determine the values of  $\tau$ ,  $\omega$  and  $g$  for each interval (wavelengths  $< 0.7 \mu\text{m}$ ). The eight non-spectral intervals (wavelengths  $> 0.7 \mu\text{m}$ ) are held constant, but the value of the height through which aerosols concentration falls drops by a factor  $e$ . It was assumed that there is no water vapor absorption for wavelengths smaller than  $0.7 \mu\text{m}$ , so clouds are assumed to be non-absorbent for the same wavelengths.

The cloud optical thickness is the most important parameter needed to describe the radiative properties of clouds. Roughly speaking, the range of optical depth is between 5 and 500 in meters. Stephens (1978) defined the cloud optical thickness as function of wavelength formally as

$$\tau_{\lambda} = \int_0^{\Delta z} \int_0^{\infty} n(r) Q_{ext}(x) \pi r^2 dr dz \quad (2.12)$$

where  $x = 2\pi r / \lambda$ ,  $n(r)$  is the cloud-droplet size distribution,  $z$  is cloud-depth varying from zero to  $\Delta z$ ,  $Q_{ext}(x)$  is efficiency factor for extinction determined from Mie theory, and the effective radius ( $r$ ) of the distribution is introduced (Hansen and Travis, 1974) as

$$r = \int_0^{\infty} n(r) r^3 dr / \int_0^{\infty} n(r) r^2 dr \quad (2.13)$$

The efficiency factor for extinction is approximately equal to two from Mie theory. The efficiency factor and effective radius formulated above are introduced into equation (2.12), and it becomes

$$\tau \approx \frac{3}{2} W / r \quad (2.14)$$

where  $W$  is the total Liquid Water Path (LWP) in  $\text{g m}^{-2}$  and  $r$  is in  $\mu\text{m}$ . The total vertical LWP is defined as

$$W = w \Delta z$$

where  $w$  is the liquid water content ( $\text{g m}^{-3}$ ), and  $W$  is based on the assumption that the cloud is vertically uniform with respect to drop-size distribution. Formal parameterization of optical thickness as a function of  $W$  requires information on effective radius, which is difficult to determine. Therefore, Stephens (1978, 1984) made an optical thickness parameterization based on calculations that were performed using a set of eight different “standard” cloud types. Stephens (1978, 1984) plotted the broadband optical thickness of these cloud types for the two spectral regions ( $0.3 - 0.75 \mu\text{m}$  and  $0.75 - 4 \mu\text{m}$ ) as a function of LWP, and then derived the least-squares-fitted lines to the points as follows:

a) For conservative scattering, ( $0.3 < \lambda < 0.75 \mu\text{m}$ )

$$\log_{10}(\tau) = 0.2633 + 1.7095 \log_e[\log_{10}(W)] \quad (2.15)$$

b) For non-conservative scattering, ( $0.75 < \lambda < 4 \mu\text{m}$ )

$$\log_{10}(\tau) = 0.3492 + 1.6518 \log_e[\log_{10}(W)] \quad (2.16)$$

In these empirical equations, the dependence of cloud optical depth on the effective radius distribution is inherently parameterized because the effective radius of distribution is a function of liquid water content.

The relationship between the backscattered fraction of mono-directional incident radiation ( $\beta(\mu_o)$ ) (Stephens 1978) and the asymmetry factor is given by the expression (Pinker et al 1992):

$$\beta(\mu_o) = \frac{1}{2} - \frac{3}{4} g\mu_o - HO \quad (2.17)$$

where  $HO$  represents higher-order terms. The asymmetry factor ( $g$ ) is deduced from  $\beta(\mu_o)$  iteratively using knowledge of the reflectance, absorption and transmittance of clouds. Accordingly, for single scattering, cloud albedo is equal to 1 for conservative scattering ( $0.3 - 0.7 \mu\text{m}$ ), and varies from 0.96 to 1 (with a most frequent value near 0.98) for non-conservative scattering ( $\lambda > 0.75 \mu\text{m}$ ). Stephens (1978) determined the single scattering albedo of cloud for eight different cloud types and then averaged these values. The values were empirically expressed as functions of cloud optical depth and solar zenith angle, as follows:

$$\omega = 1 - \sqrt{3} \left( \sum_{i=1}^{m+1} \sum_{j=1}^i w_n x^{i-j} y^{j-i} \right) (n = n + j) \quad (2.18)$$

where  $x = \ln(\tau)$ ,  $y = \mu_o$  and  $w_n$  and  $m$  are the surface polynomial coefficients (initially  $n = 0$ ). Note that the solution parameters (optical depth, single scattering albedo and

asymmetry factor) in the radiative transfer equation apply for a specific wavelength or band of wavelengths, in which they are assumed to be uniform.

### **2.3.2 Satellite Algorithm**

The atmospheric radiative transfer model described above was applied in a wide range of conditions to generate a look up table of atmospheric reflectance (R) and atmospheric transmittance (T) over a non-reflecting surface expressed as a function of spectral interval, solar zenith angle, ozone and water vapor amounts, aerosol optical depths for clear skies, and cloud optical depth for cloudy skies. For cloudy cases, a constant value for (climatological) aerosol extinction is also included in the data library. For a set of given realistic atmosphere-surface conditions, the relationship ( $T = f_i(R)$ ) between atmospheric reflectance and transmittance is derived from this data library. Fluxes and optical depths are determined by matching the broadband top of the atmosphere (TOA) albedo under clear and cloudy skies (routinely observed by GOES satellites) with the albedo computed from the look up tables. The input parameters and the primary function for which they are used in the satellite algorithm are given in Table 2.2. The required atmospheric precipitable water inputs are obtained from the Eta model-- but with adjustment for the topography used in the RAMS model. To obtain the model TOA albedo, the atmospheric aerosol model (continental or marine) appropriate for the given observation is selected by identifying the surface type (ocean, land, desert and snow) from the global vegetation data of map (Matthews, 1985). The reflectances and transmittances from the model are then interpolated to correspond to the actual values of

the solar zenith angle, precipitable water and ozone amount. The result is two subsets of models, which depend on the aerosol optical depths for clear sky conditions, and cloud optical depths for cloudy sky conditions. The surface spectral albedo is retrieved by the combination of reference albedo models (Briegleb et al. 1986) as a function of surface type and the clear-sky composite albedo derived from GOES satellites with minimum aerosol and atmospheric contribution to the signal. The reference albedo models, which are specified for ten surface types, are updated by the satellite-derived albedo. The retrieval of surface albedo is illustrated in Figure 2.4a. Finally, the broadband TOA albedo is obtained, by spectrally integrating the reflectances of the surface-atmosphere system. The TOA radiances associated with clear and cloudy pixels are a function of the positions of the satellites and the sun relative to the scene observed. These positions are described by the zenith angle of the satellite and the sun ( $\theta$  and  $\theta_o$ ) and the relative azimuth angle ( $\phi$ ). The measurements represent radiation in a narrow band of the shortwave spectrum. To enable the use of relationships between flux transmissivity and broadband albedo, satellite narrowband radiances need to be converted to broadband albedo. A narrowband bi-directional reflectance  $R_n(\theta, \theta_o, \phi)$  is computed from the measured radiance  $L(\theta, \theta_o, \phi)$  as follows:

$$R_n(\theta, \theta_o, \phi) = \frac{\pi L(\theta, \theta_o, \phi)}{\cos \theta_o E_o} \quad (2.19)$$

where  $E_o$  is the TOA shortwave irradiance corrected for the sun-earth distance. To bring the spectral observations to a common denominator,  $R_n(\theta, \theta_o, \phi)$  is transformed into a

broadband bi-directional reflectance  $R_b(\theta, \theta_o, \phi)$ , assuming a linear transformation between the two reflectances:

$$R_b(\theta, \theta_o, \phi) = MR_n(\theta, \theta_o, \phi) + B \quad (2.20)$$

The narrow to broadband conversion factors,  $M$  and  $B$ , for different satellites were defined from simulations over ocean, vegetation, desert, and clouds (Lazslo et al. 1988). Finally,  $R_b(\theta, \theta_o, \phi)$  is converted into a broadband albedo  $R_{sat}$  using the anisotropic correction factors  $X(\theta, \theta_o, \phi)$ , developed for the Earth Radiation Budget Experiment (ERBE) project (Suttles et al. 1988):

$$R_{sat} = \frac{R_b(\theta, \theta_o, \phi)}{X(\theta, \theta_o, \phi)} \quad (2.21)$$

In summary, the outputs from this step contain the broadband planetary albedo derived separately from clear and cloudy radiances ( $R_{sat, \text{clear}}$  and  $R_{sat, \text{cloudy}}$ ), and an identification of the observed scene (scene ID). Moreover, a broadband planetary albedo is derived from clear-sky composite radiance  $R_{CSC}$ .

The atmospheric transmittance and aerosol and cloud optical depths associated with the model, which provides the best match between the model TOA albedo and the satellite TOA albedo for given observations, are determined by linear interpolation from the values in the data library. The spectral direct and diffuse surface irradiances,  $SW_{dir}$  and  $SW_{dif}$ , are obtained from:

$$\begin{aligned} SW_{dif} &= \cos \theta_o E_o T^{dif} \\ SW_{dir} &= \cos \theta_o E_o T^{dir} \end{aligned} \quad (2.22)$$

and global spectral irradiance is obtained by summing the two components:

$$SW = SW_{dir} + SW_{dif} \quad (2.23)$$

Average fluxes are obtained by weighting the clear and cloudy pixels by the number of clear and cloudy observations. A flow chart summarizing the flux retrieval is showed in Figure 2.4b.

Table 2.2 Input parameters and their primary functions in the algorithm.

INPUT PARAMETER	FUNCTION
Clear-Sky Radiance	To derive fluxes for clear-sky condition
Cloudy-Sky Radiance	To derive fluxes for cloudy-sky condition
Clear-Sky Composite Radiance	To derive surface albedo
Number of Clear Pixels	To weight clear-sky fluxes for all-sky conditions
Number of Cloudy Pixels	To weight cloudy-sky fluxes for all-sky conditions
Precipitable Water and Ozone Amount	To select optical functions
Solar and Satellite Zenith and Relative Azimuth Angles	To select anisotropic correction factors
Latitude and Longitude	To select clear-scene type and surface albedo model
Satellite ID	To select appropriate narrow-to-broadband transformation
Snow Cover	To weight snow cover

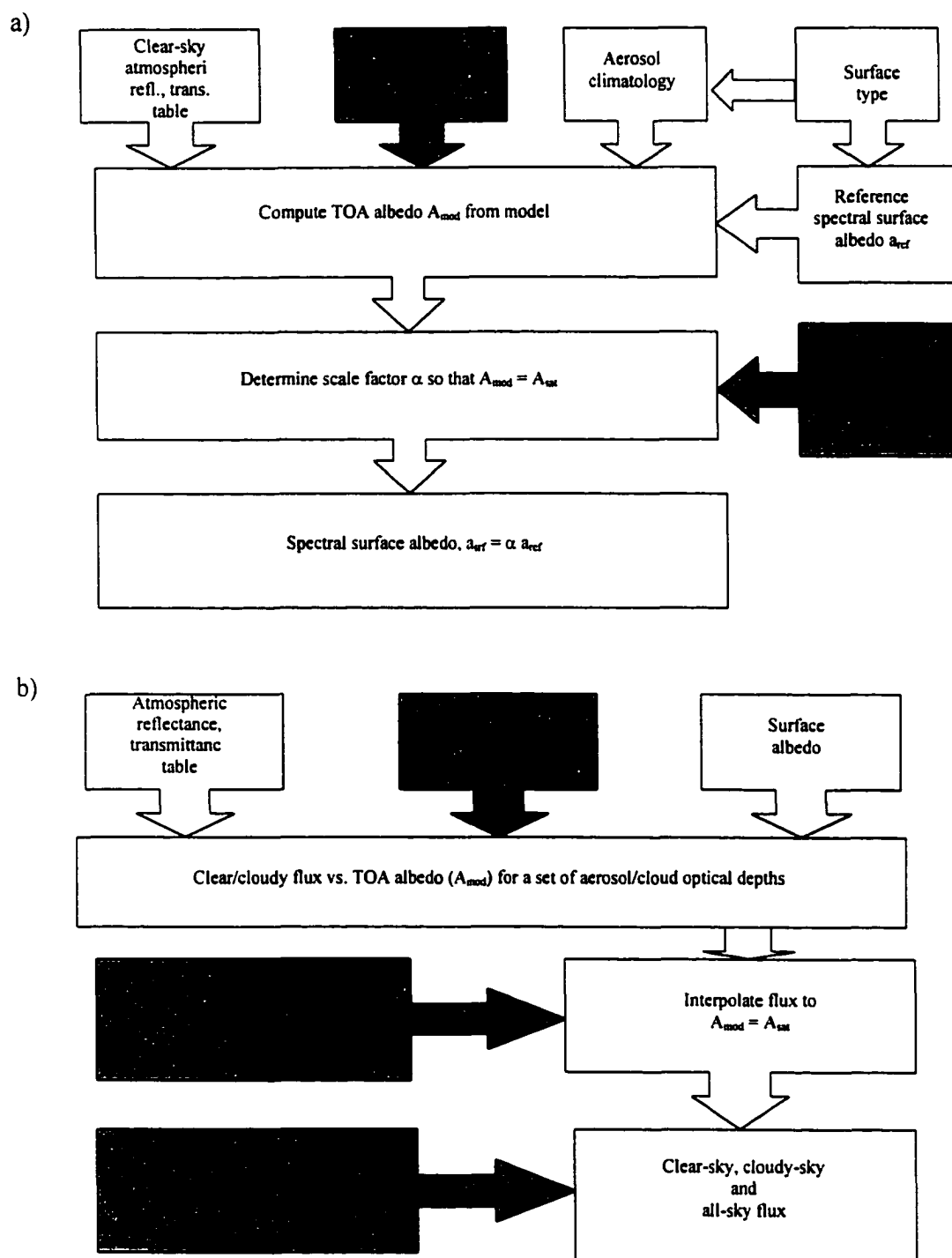


Figure 2.4 The retrieval of surface albedo is illustrated in (a) and the retrieval of surface solar radiation is summarized in (b).

## **CHAPTER 3**

### **RESEARCH LOCATION AND DATA**

#### **3.1 Introduction**

This chapter provides information on the region selected for study in Southern Arizona, on the experiment site, and on the data acquisition and processing of satellite, observed, and modeled data. A detailed description of the study region, experiment site and the data taken from these sites is given in Section 3.2 Information on the satellite data and model-derived data is provided in Section 3.3 and Section 3.4, respectively.

#### **3.2 Field Data**

Figure 3.1 shows the location of Southern Arizona together with the position of the individual stations in the observational networks from which data were taken, the position of the experimental site at which data were collected, and the position of the model domain used in this study.

##### **3.2.1 Southern Arizona Site**

The southern part of the state of Arizona that selected for the purposes of making comparison between observations and modeled-generated data in this study comprised a box laying approximately between 31.5 N and 36 N and 108 W and 115 W. The southern,

eastern, and western edges of this box roughly correspond to boundaries of Arizona, while the northern edge approximately coincides with the I40 Interstate.

The semi-arid environment that typifies this Southern Arizona site is in part due to its location (close to 30° N) and in part because it is in the rain-shadow of mountain ranges. The dominant geologic structure of the site is the 'Basin and Range' province, which is characterized by rugged mountain ranges separated by flat valley floors. The numerous ranges create multiple rain shadow zones which exacerbate an already very dry climate. The limited rainfall of less than 20 inches (50 cm) per year often occurs through violent thunderstorms with high rainfall rates. Such intense rain can create significant runoff resulting in flash floods because the soil is bare and sun-baked.

Daily temperature changes can be large (up to 20° C) in dry climates and winds can be quite strong. These climate features are important influences on drainage and topography. Weathering creates geological features by eroding and aging the topography, with sedimentation apparent in the soil structure in the form of differences in grain size. As regards vegetation cover, some specialized types of plants do grow well in desert climates because they have extensive root systems to access water. They are often widely spaced and their leaves are usually very small, so helping to reduce the water lost by transpiration. During the much of the year many plants appear dead, but when rain falls the plants rapidly become green. The individual observation stations within the Southern Arizona site are usually located in regions of irrigated agriculture and the data may, in part, be influenced by this fact.

The study was focused on seventeen individual stations that are concentrated near the center of the study area. The stations are, in general, representative of the geological, climate and topography of Southern Arizona. Table 3.1 provides detailed information on the locations, elevation, soil particle size and soil texture at each station. The information given in this table was taken from the Arizona Meteorological Network (AZMET: <http://ag.arizona.edu/azmet/>) web page. The soil particle size and texture type are based on the analysis of samples of bare soil taken between ground level and 12 cm depth within one square meter area of the soil temperature probes used in the meteorological stations. The soil percentages are calculated for sand, silt and clay after removing the gravel, and the soil texture is derived from these percentages.

**Table 3.1. Information on the AZMET stations**

Stations (#)	Coordinates lat, lon	Elevations (m)	Soil Particle Size			Soil Texture Type
			Sand (%)	silt (%)	clay (%)	
Tucson (01)	32.28 N 110.946 W	713	64	26	10	Sandy Loam
Q. Creek (22)	33.258 N 111.642 W	430	-	-	-	analysis not complete
Harquahala (23)	33.483 N 113.116 W	350	-	-	-	analysis not complete
Safford (04)	32.813 N 109.69 W	901	46	30	24	Loam
Coolidge (05)	32.98 N 111.605 W	422	62	25	13	Sandy Loam
Marcopa (06)	33.069 N 111.972 W	361	-	-	-	analysis not complete
Aguila (07)	33.947 N 113.189 W	655	31	34	35	Clay Loam
Buckeye (26)	33.40 N 112.68 W	304	-	-	-	analysis not complete
Bonita (09)	32.4636 N 109.929 W	1346	77	16	7	Loamy sand
Waddell (10)	33.618 N 112.460 W	407	60	30	10	Sandy Loam clay
Litchfield (11)	33.467 N 112.398 W	309	66	23	11	Sandy Clay Loam
P. Greenway (12)	33.621 N 112.108 W	401	-	-	-	analysis not complete
Marana (13)	32.461 N 111.233 W	601	-	-	-	Silt clay loam
P. Encanto (15)	33.479 N 112.096 W	335	-	-	-	analysis not complete
Eloy (16)	32.774 N 111.557 W	461	-	-	-	analysis not complete
Paloma (19)	32.927 N 112.896 W	219	-	-	-	analysis not complete
Laveen (21)	33.376 N 112.15 W	315	-	-	-	analysis not complete

### **3.2.1.1 Data from AZMET Network**

The data fields of interest in this study were acquired from the Arizona Meteorological Network (AZMET), which has been in operation since 1986 to provide weather data information for agricultural and horticultural purposes. The available data fields provided by AZMET are air temperature (in °C), humidity (in %), solar radiation (in MJ m<sup>-2</sup>), wind speed (in m s<sup>-1</sup>), precipitation (in mm), soil temperatures at 5 cm and at 10 cm (in °C), vapor pressure deficit (in kPa), and Reference Crop Evapotranspiration (in mm). These data are collected by an automatic weather station located at each site and transmitted over phone lines to a central computer where they are processed and made available to the public on AZMET's computer bulletin board system (BBS). The AZMET data fields are made available in comma delimited, ASCII format. They are provided as both hourly and daily data, with bad date identified by inserting 9999 or 999.

Each AZMET weather station is maintained by a data logger (Campbell Scientific Inc, Utah), which samples the sensors every ten seconds and processes and stores all the sampled measurements for each hour. At midnight, the data logger processes the hourly measurements and calculates the daily values for the previous day. The measurements of precipitation and solar radiation are totaled, while readings of temperature, humidity, wind speed and direction, vapor pressure deficit and reference crop evaporation are averaged. Table 3.2 provides detailed information about the sensors used at the AZMET stations. The solar radiation and wind speed sensors are replaced with recalibrated sensors once a year, and the humidity sensors are recalibrated twice a year. All the data fields reported by

AZMET follow Arizona time. In this study the data fields of interest are incoming solar radiation and precipitation. These were obtained from AZMET web page rather than the AZMET bulletin board.

**Table 3.2** The detailed information about sensors at AZMET (Adapted from AZMET WEB page.)

Measurement	Instrument Model	Sensor Type	Siting	Accuracy
Air Temperature	Camp. Sci. Model 207 Probe	Thermistor Fenwall (UUT51J1)	1.5 m above surface	+/-0.2C
	Vaisala	Thermistor Fenwall (UUT51J1)	1.5 m above surface	+/-0.4C
Rel. Humidity	Camp. Sci. Model 207 Probe	Resistance Chip: Phys Chem PCRC11	1.5 m above surface	+/-5%RH
	Vaisala	Vaisala Capacitive	1.5 m above surface	+/-2%RH
Solar Radiation	Licor LI200S Pyranometer	Silcon Cell Pyranometer	2.5 m above surface	+/-5%
Precipitation	Sierra Misco RG2501 Rain Gage	Tipping Bucket With Magnetic Reedswitch	Gage top at ~43cm above surface	+/-1mm
Wind Speed	Met One Model 014A Wind Speed Sensor	Anemometer Using Reed Switch	3.0 m above surface	+/-1.5%

### 3.2.2 Experiment Site

A field experiment was set up to provide measurements of downward long-wave radiation fluxes for comparison with model-generated fluxes because these data were not available from AZMET networks. The experiment site is located at 32.05 N and 110.50 W, near Tombstone in southern Arizona, as shown in Figure 3.1. The site characteristics and climate features of the experiment site are similar to those described above for the AZMET stations. A Kipp & Zonen radiometer was purchased and deployed at the site. This radiometer has two optional modes for installation. It only measures net radiation in the first optional mode, but it is able to measure the four components of the radiation (upwelling and downwelling solar radiation, and upwelling and downwelling terrestrial radiation) simultaneously if the second optional mode is used. Since downwelling long-wave and downwelling short-wave radiations are of interest in the study, the radiometer was installed to operate in the second mode. The pyrogeometers, sensors to measure upward and downward components of terrestrial radiation work in the wavelength range 5 and 50  $\mu\text{m}$ , while the pyronometers sensors to measure solar radiation components work in the wavelength range 0.3 and 3  $\mu\text{m}$ . The pyrogeometer makes measurements which incorporate temperature compensation for detector response. It has a response time of 2 seconds and output ranges from 0 to 700  $\text{Wm}^{-2}$ . A data logger (Campbell Scientific Inc, Utah) was connected to the radiometer processed and stored all the observations as 15 minute average values. Data collection with this instrument started June 15, 2000, thus data were available for one of the 2-day model run for which comparisons were made (June 22-23, 2000).

### 3.3 Satellite Data

Data from the Geostationary Operational Environmental Satellites (GOES) are used in the study. These satellites provide continuous monitoring in the equatorial plane of the earth in a geosynchronous orbit at a speed that matches that of the Earth's rotation. The geosynchronous plane is about 35,800 km above the Earth, high enough to allow the satellites a full-disc view of the Earth. Since their speed matches the Earth's rotation, they hover continuously over one position on the Earth's surface and in this way provide constant vigil of atmospheric and surface conditions.

The GOES has two primary instruments, the Imager and the Sounder. The first is a five channel (one visible, four infrared) imaging radiometer designed to sense radiant and solar reflected energy from sampled areas of the earth. The second provides data to determine the vertical temperature and moisture profile of the atmosphere, surface and cloud top temperatures, and ozone distribution. The primary satellite data used for this study was the reflected visible (0.55 – 0.75 $\mu$ m) radiance observed by the imaging spin-scan radiometer (VISSR) on GOES-10 (or GOES-West) which was positioned at 135 W longitude above the equator. The VISSR can simultaneously sweep an 8-kilometer north-to-south swath along an east-to-west/west-to-east path, at a rate of 20 degrees east-west per second. The main characteristics of the Imager radiometer are provided in Table 3.3. For a region covering 1200 pixels along longitudinal direction and 1000 pixels along latitudinal direction (Figure 3.2), the visible images, which are available every 15 minutes during daylight hours, have been collected since August 1997. These images are still routinely being collected via the

Internet. The size of the individual picture elements (pixels) determines the spatial resolution of the satellite sensor, which is an approximately 1-km resolution (for a nadir view). The raw data are originally stored with 10-bit precision by NOAA Environmental Satellite, Data, and Information Service (NESDIS), but subsequently these data are converted to calibrated “albedo”, unadjusted for direction angle, with 8-bit precision by NASA. These dimensionless quantities range from 0 to 255 are proportional to the albedo, which is derived from the following equation:

$$a = count * 0.4$$

where  $a$  is albedo and  $count$  is the 8-bit data value (0-255). The radiances are calculated from albedo using the following calibration equation:

$$R = (a / 100) / c$$

where  $R$  is the calibrated radiance (in  $W\ m^{-2}$ ), and  $c$  ( $=1.94180e-03\ m^2 / W$ ) is the conversion coefficient. The coefficient and equations are obtained from calibration document available in the NASA URL page.

Navigation files, which provide geometrically corrected pixels for latitude and longitude points, are provided along with the image files for use in post-processing. To use these satellite data efficiently, a computer code must be applied to analyze and quality control the data by filtering any random noise in the satellite images. (Noisy lines in the images are filtered and replaced by the nearby good lines).

### **3.4 Modeled-Derived Data**

In this study, the main surface fields derived from the RAMS to compare with data from the AZMET sites were incoming short-wave and long-wave radiation and precipitation. These surface fields were selected because their magnitudes mainly depend on the cloud cover which, in this study, is derived by assimilating satellite data into the RAMS model. The model domain covered an area of 400 km x 400 km at 4-km resolution centered on (33.25 N, -111.7 W), as shown in Figure 3.1. The modeled data from the simulations with and without cloud assimilation were gathered during a 3-day period, 14-16 July 1999, and during a 2-day period, 22-23 June 2000, these periods being selected because satellite data showed a worthwhile amount of cloud during these periods.

The model timestep was set to 15 seconds, this being appropriate for a model with spatial resolution of 4-km. Both the atmospheric and surface tendencies for radiative calculations are only updated every 15 minutes during model integration because of the computationally expensive process. The total surface precipitation is accumulated every timestep during model integration. Since observed radiation fields are, in general, hourly average values, corresponding average fields were calculated for the model. Similarly, the modeled hourly total surface precipitation was derived because the observed precipitation is that accumulated amount in an hour. The above modeled data fields were obtained for locations in the RAMS grid coordinate corresponding to AZMET sites, with the time code appropriately adjusted to correspond to local time.

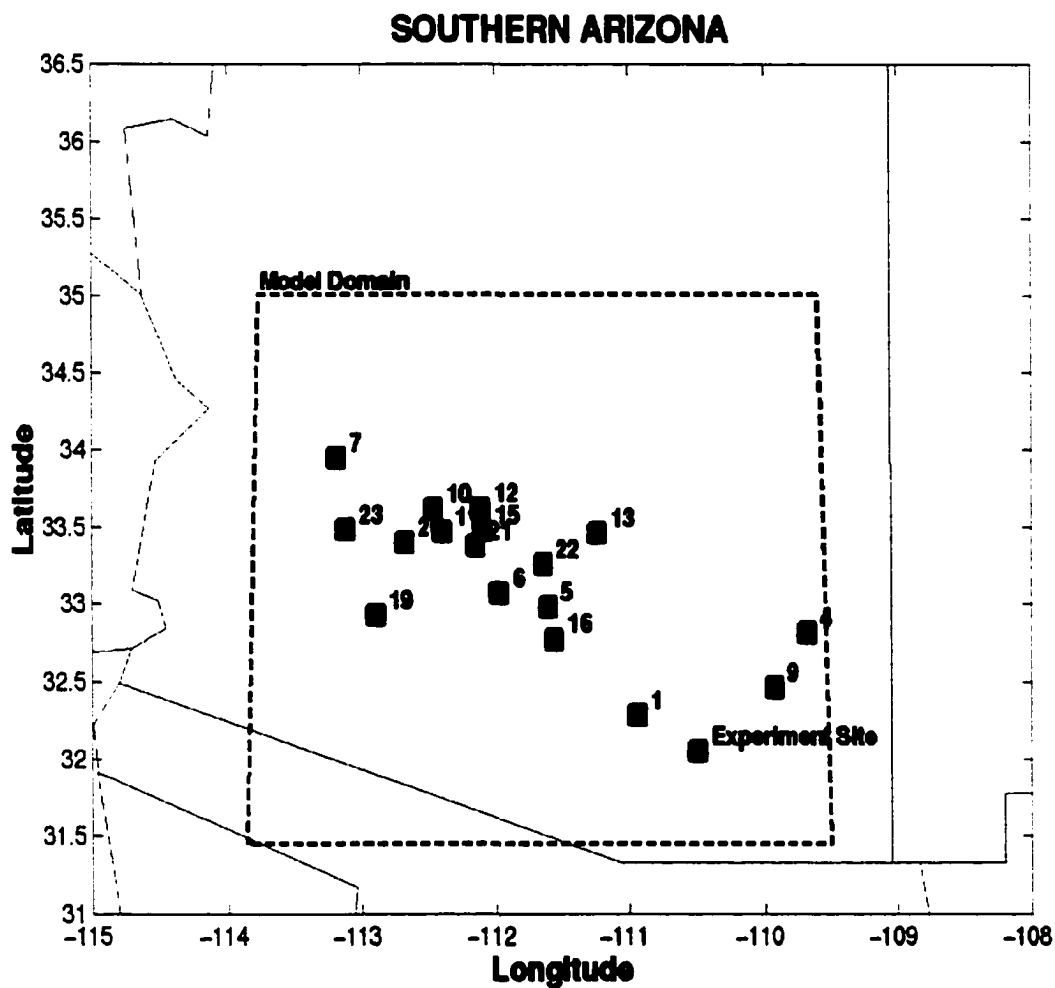


Figure 3.1 The state of Arizona showing the general location of the AZMET networks in southern part of the state. The labels at the top-right-hand corners of each small square identify the station number of each AZMET site.

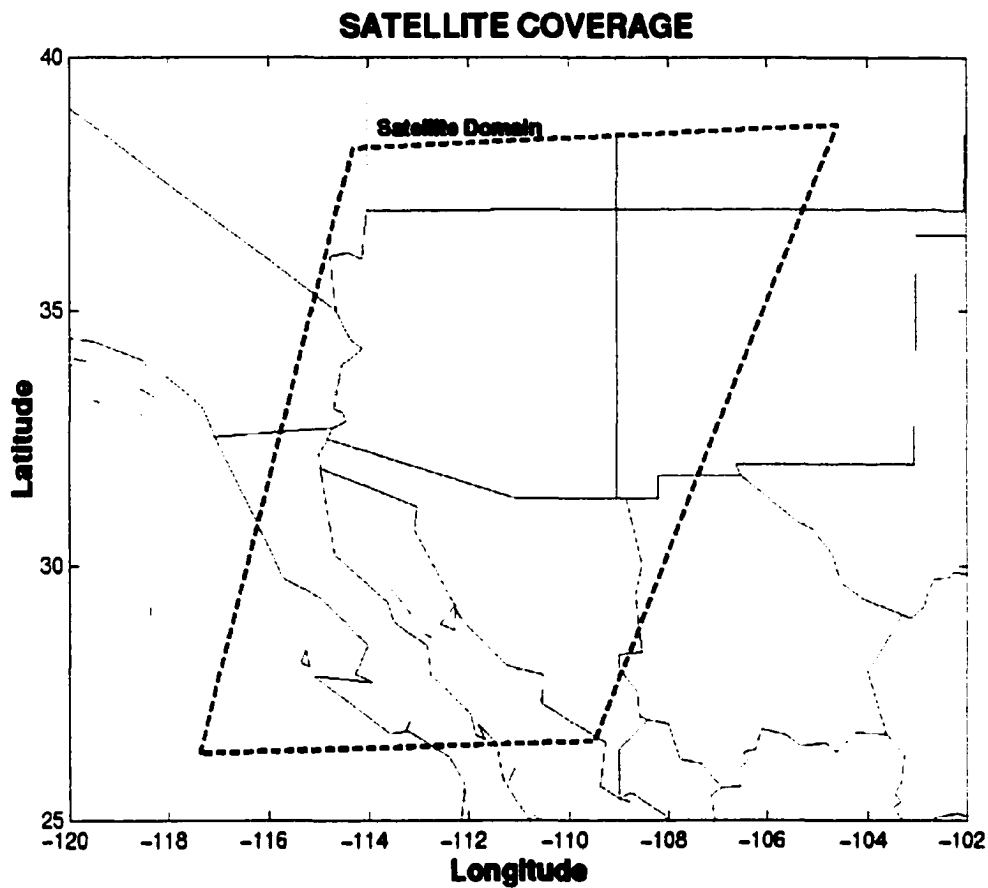


Figure 3.2 The broken line shows the area coverage of visible images which includes 1200 (1-km) pixels in X direction and 1000 (1-km) pixels in Y direction.

Table 3.3 The main characteristics of the GOES Imager radiometer.

<b>Imager Instrument Characteristics (GOES)</b>					
<b>Channel number:</b>	<b>1 (Visible)</b>	<b>2 (Shortwave)</b>	<b>3 (Moisture)</b>	<b>4 (IR 1)</b>	<b>5 (IR 2)</b>
<b>Wavelength range (<math>\mu\text{m}</math>)</b>	0.55 - 0.75	3.80 - 4.00	6.50 - 7.00	10.20 - 11.20	11.50 - 12.50
<b>Instantaneous Geographic Field of View (IGFOV) at nadir</b>	1 km	4 km	8 km	4 km	4 km
<b>System absolute Accuracy</b>	<b>IR channels: less than or equal to 1 K</b> <b>Visible channel: %5 of maximum scene irradiance</b>				
<b>Imaging rate</b>	<b>Full earth disc, less than or equal to 26 minutes</b>				

## **CHAPTER 4**

### **CLOUD SCREENING ALGORITHM**

#### **4.1 Introduction**

Human image processing skills are such that it is comparatively easy for us to determine whether or not a particular GOES scene is clear or cloudy. However, due to the vast quantity of GOES data that is routinely produced, it is simply not possible to rely on human image processing skills for this purpose in most applications. Consequently, many automated image-processing methods have been developed over the years and these have been applied with varying degrees of success (e.g. Stowe et al., 1989; Warren et al., 1986; Wylie and Menzel, 1989; Seze and Rossow, 1991; Pinker and Lazlo, 1992; Pinker et al., 1994; and Stewart et al., 1994). Many of these methods were applied to data from polar-orbiting satellites that provide a single daylight image each day, and this precluded investigation of diurnal changes in cloud cover.

Clouds are characterized by the fact that they generally have a higher reflectance and a lower temperature than the underlying earth surface. However, there are land surface conditions when relying on these distinctions to characterize the presence of clouds is inappropriate, most notably over snow- and ice-covered surfaces. Additionally, some cloud types, such as thin cirrus and small cumulus clouds and low stratus cloud at night, are difficult to detect because they have insufficient contrast with surface radiance. Cloud edges cause further difficulty because the instrumental field of view will not always be either completely cloudy or completely clear. In spite of these uncertainties in

cloud detection methods, simple visible and infrared “window threshold” approaches offer considerable skill in cloud detection. In this chapter, the algorithm for detecting clouds from GOES observations used in the present study is first described, followed by a description and evaluation of the results obtained when this algorithm is applied.

## 4.2 Methodology

During the present study, a novel automatic procedure was developed to derive high-resolution (4 km x 4 km) fields of cloud cover and associated cloudy- and clear-sky radiance maps from visible band GOES data. The method is an extension of that used by Garatuza et al. (2000) but it differs in that it uses a new real-time tracking procedure to determine the required clear-sky composite image rather than relying on retrospective derivation of monthly-average threshold indexes. In this study, cloud detection involves partitioning radiance samples from within an array of 4 x 4 contiguous pixels into three categories, specifically (a) totally cloud-free, (b) completely cloudy, or (c) partly covered by clouds. The decision rules used to discriminate between these groups are threshold statements. Thus, an individual pixel was designated to be “cloudy” if the radiance is greater than a threshold value (e.g., 35% reflectance). Alternatively, it may be designated “clear” if the radiance is less than a specified value (in the present study, the radiance of a running mean plus the standard deviation of clear sky values was used). Pixels that are neither cloud-covered nor clear were designated “mixed”. Using this approach minimizes false cloud detection, but it may miss light cloud if its observed radiance closely resembles that for pixels with no cloud.

In general, examination of the time records of visible radiance for a particular area reveals four types of variation (Sèze and Rossow, 1991). In decreasing order of magnitude, these are:

- (a) variations due to the formation and/or dissipation or to the movement of clouds;
- (b) periodic variations associated with changes in solar illumination;
- (c) variations in surface conditions at synoptic and seasonal time scales; and
- (d) variations in radiance associated with changing atmospheric conditions.

The daily variation in solar illumination usually causes changes in surface radiance that are comparable in magnitude to those caused by changing cloud cover. Success of the threshold method relies on accurately selecting the clear-sky threshold. The ensuing cloud screening algorithm involves the two steps described in the next two sections.

#### **4.2.1 Deriving Clear-Sky Composite Images**

The full-resolution (1 km) GOES observations were first grouped into 4 x 4 “target areas” comprising 16 of the original (1km x 1 km) pixels, and the average,  $R$ , and standard deviation of the observed radiance were computed for each target area for each 15 minute image every day. The radiance for each 4 x 4 pixel was then corrected for changes in the sun-to-earth distance and the solar zenith angle using standard equations and parameters from the Nautical Almanac.

Temporal variations in clear-sky reflectance are usually smaller than spatial variations. The (generally small) variations of surface reflectance in the visible wave band and the tendency for the surface reflectance to be smaller than cloud reflectance

produce a characteristic shape in the darker part of the visible radiance probability distribution that is only weakly related to the surface cover (Sèze and Rossow, 1991). This relatively simple behavior of the visible radiance (Reynolds and Vonder Haar, 1977) allows use of the minimum value to estimate clear-sky values from a set period, usually selected to be one month. However, using a monthly minimum always introduces some phase delay into the clear-sky radiance estimate if there is an annual cycle in surface albedo and it biases the clear sky radiance estimate low if there is random noise in the GOES signal. Recognizing these deficiencies, an alternative automatic procedure was developed to give near real-time tracking of the clear sky radiance for each target area for each time of the day in the GOES data. This automatic procedure required specification of an initial clear sky radiance and acceptance windows, and initial estimates of the standard deviation (an estimate of the random noise) of the clear sky radiance for each 4 x 4 group of pixels. These initial/window values were calculated from data for the 5-10 clearest days selected from among the pre-existing GOES observations. The value of the acceptance window (here called *window*) defines the number of radiance units above the running mean for which some cloudy sky is assumed. It determines whether the currently observed value of the radiance is accepted and used to update the running estimate of clear sky radiance. It was set to the estimated random noise given by the satellite sensor, thus

$$window = 4 \leq \left( \frac{max - R_{clear}}{4} \right) \leq 10$$

where  $max$  is the maximum clear sky radiance for each 4 x 4 target area and  $R_{clear}$  is the initial, mean clear sky radiance for that target area. Once the initial composite radiance and  $window$  values have been defined, the real-time tracking procedure is applied to update the mean clear sky radiance and standard deviation of each target area used to specify the optimum threshold that distinguishes cloudy from clear skies, which threshold varies with location and time (Rossow and Garder, 1993).

The automatic procedure used to estimate the clear-sky reflectance for each target area at each time of the day is illustrated in Figure 4.1(a). First, for each individual pixel, inverse corrections for satellite viewing geometry were applied to allow for the angular dependence of clear-sky radiance. A decision was then made as to whether to update the value of clear sky radiance from that used at the current time on the previous day. The following logical expressions were used to replace the previously assumed values of  $R_{clear}$  and the standard deviation,  $\sigma_{clear}$  of clear sky radiance for the target area.

$$\text{If } R < (window + R_{clear}) \text{ and } \sigma < (4 \cdot \sigma_{clear})$$

and

$$R_{clear} = weight \cdot R_{clear} + (1 - weight) \cdot R$$

$$\sigma_{clear} = \sigma \text{ If } \sigma < \sigma_{clear}$$

where:

$$weight = WMAX \cdot \exp(-vndays/TD)$$

In above expressions,  $R$  is the currently measured radiance,  $\sigma$  is the newly calculated standard deviation of radiance,  $weight$  is the transient value of the weight assigned to the old running mean of clear sky radiance,  $WMAX (= 0.7)$  is the maximum weight,  $vndays$  is the number of days through which running mean has not been updated, and  $TD (=10)$  is an assumed time constant (in days).

This decision/replacement procedure was carried out for each 4 x 4 pixel target area (there were 300 x 250 target areas in the processed image) until the last days of each run. The resulting estimates of the updated clear sky radiance for every time of day on each day were then assembled into the daily “clear-sky composite” images used during image processing.

#### 4.2.2 Deriving Fractional Cloud Cover

For each 4-km resolution GOES target area, the analysis procedure provides the number of cloudy and clear pixels and the value of their radiance. Specifying which pixels are cloud-free involves comparing the actual measured radiance (computed from Equation (3.1)) for that pixel, with the value of radiance for the target area in which the pixel falls in the corresponding clear-sky composite image. The procedure is illustrated in Figure 4.1(b). Thus, the observed value of radiance for the pixel is compared against,  $R_{clear}$ , the clear-sky composite value for the target area in which the pixel falls and, if the observed value is less than  $(R_{clear} + 15 \sigma_{clear})$ , the pixel is classified as being a clear-sky pixel. (Note: the factor 15 in this expression may vary with application and is sometimes called the “contrast threshold”. Typically, the contrast threshold corresponds to a

reflectance of about 10%). If the observed raw data count is greater than 358 times the cosine of ( $Z$ ), where  $Z$  is the solar zenith angle, the pixel is classified as being totally cloud-covered. (In raw data terms, the value 358 corresponds to the radiance prescribed to bright cloud in this study.) If the pixel does not fall into either the clear-sky or totally cloud-covered categories, it is classified as having mixed cloud cover.

Pixels defined as having mixed cloud cover are then re-allocated between the clear-sky and totally cloud-covered categories. The proportion of mixed pixels is given by the ratio of the average measured radiance for the mixed pixels minus the clear-sky radiance, to the (prescribed) value of radiance corresponding to total cloud cover minus clear-sky radiance, as follows:

$$f = \frac{\bar{R}_{mixed} - R_{clear}}{R(35\%) - R_{clear}}$$

and the number of cloudy-sky and clear-sky pixels are respectively re-designated as follows:

$$n'_{cloudy} = n_{cloudy} + f * n_{mixed}$$

$$n'_{clear} = n_{clear} + (1 - f) * n_{mixed}$$

The final step is to assign a fractional cloud cover to each target area on the basis of how many of the (16) contributing pixels have finally been designated as having complete cloud cover.

### **4.3 Application and Evaluation of the Algorithm**

The cloud-screening algorithm was applied to the GOES visible data to detect high-resolution cloud cover. The resulting estimated cloud cover was then assimilated into a meso-scale meteorological model to improve the surface fields calculated by the model. The results of this procedure are discussed and evaluated in terms of the spatial patterns relative to observed satellite images, and in the form of the modeled daily time series for 4-km pixels judged relative to observations from the corresponding station in the AZMET network. For the purpose of this study, the cloud retrieval algorithm, model assimilation, and ensuing comparison was made for a few days at approximately the same time of year in two different years. Evaluation is made both in terms of simultaneous comparison between modeled and observed values and in terms of daily-average values.

#### ***4.3.1 Spatial Patterns***

The daily average, clear-sky composite images derived from the 15-minute composite images using the above-described algorithm are illustrated in Figure 4.2(a) for July 16, 1999 and June 23, 2000. (Note: in practice, the algorithm was run for the period July 14 – 16, 1999 and for June 22 – 23, 2000). Each day the composite radiances images are updated to those of the previous day. Consequently, for both periods, the last-day composite radiance images are used as being the most representative, clear-sky composite image for the purpose of this evaluation. Both figures clearly show that any contamination that may result from the presence of unusually persistent clouds is minimized and/or removed. Spatial variations in surface albedo are reasonably described

by the lowest values over water surfaces and the (variable) highest values over land surfaces. The frequency distribution of observed radiance in the clear-sky composite image for the whole image area is shown in Figure 4.2(b) for July 16, 1999 and for June 23, 2000 at 16:00 GMT. The same histograms, but for 22:00 GMT are shown in Figure 4.2(c) for July 16, 1999 and for June 23, 2000. In these diagrams, the differing radiance of water and land is clearly visible. The narrower peak at lower values corresponds to water surfaces while the broader peak at higher radiances corresponds to land surfaces. In these figures, the separation between the two peaks corresponding to radiance from water and land is more pronounced at 22:00 GMT because the surface radiance over land increasingly shifts to higher radiance values as the surface illumination increases. The two peaks for water and land surfaces are reasonably well-defined relative to the full range of radiance, the observed differences in the frequency distribution between morning and afternoon are significant, and there is also no extended tail towards higher values of radiance in the frequency distributions. Together, these facts suggest that, in this study area, some clear-sky conditions are always encountered for each target area when clear-sky composite images are built using the automated, real-time tracking procedure used in the study. Moreover, the daily clear-sky composite images shown in Figure 4.2(a) and the frequency distributions shown in Figure 4.2(b)-(c) in consecutive years (1999 and 2000) suggest that the surface radiance does not change greatly between years. Presumably this is because the seasonal evolution of surface conditions is fairly consistent from one year to the next in this particular study area.

The purpose of the cloud screening procedure is to determine the cloud cover, and clear and cloudy radiance values from the GOES visible observations. These output fields from the algorithm along with original GOES visible image are illustrated in Figure 4.3 and in Figure 4.4 for July 14, 1999 at GMT 2200 and for June 22, 2000 at GMT 2000, respectively. According to the GOES data, the cloud cover was greatest at these particular times on these days. The cloudy radiance, clear radiance, and cloud fraction in Figure 4.3 and in Figure 4.4 show that the algorithm does indeed successfully separated cloudy from clear regions in the GOES images. If a 4km x 4km target area is totally covered by clouds, the algorithm assigns the clear radiance to zero for that particular target area, while if the target area is completely cloud free, its corresponding cloudy radiance is assigned to zero. GOES visible image in Figure 4.4 is a good example of one with small-scale cumulus clouds, the ability to recognize these being a critical test of algorithm performance. Fortunately, the algorithm shows an ability successfully to capture the small-scale cloud features discernable in this satellite image.

#### ***4.3.2 Time series***

The time series of cloudy radiance, clear radiance, composite radiance, and cloud cover for the 4-km target areas corresponding to sites in the AZMET observational network are shown in Figure 4.5a,b for July 14-16, 1999, and in Figure 4.6a,b for June 22-23, 2000. In these figures, the radiance values are given on the left-hand-side Y-axis while the cloud cover is given on the right-hand-side Y-axis. The GOES estimates of radiances and cloud cover are available as instantaneous samples every 15-minutes but,

for convenience, the hourly-average values of these 15-minute fields were calculated and these are the values displayed in Figures 4.5a,b and 4.6a,b. The figures illustrate inter-relationship between the values of cloudy, clear and composite radiances and cloud cover as they evolve through time.

As expected, there is straightforward relationship between cloudy radiance and cloud cover, and these two variables are, again as expected, inversely proportional to the clear radiance. As explained in the previous section, the algorithm assumes that pixel is clear if all the individual pixels in a target area have a radiance that is less than the running mean clear-sky radiance plus the standard deviation of the clear sky radiance. The application of this condition is evident in these figures. The clear-sky radiance, for instance, always stays less than the composite radiance throughout the period. It is also apparent in these time series plots that the composite radiance follows a smooth diurnal cycle each day, also expected. These features were observed at each of the 18 different target areas corresponding to individual AZMET stations. On the basis of Figures 4.5 and 4.6, we conclude that the algorithm functions correctly and that it provides an appropriate, fine resolution detection of clouds.

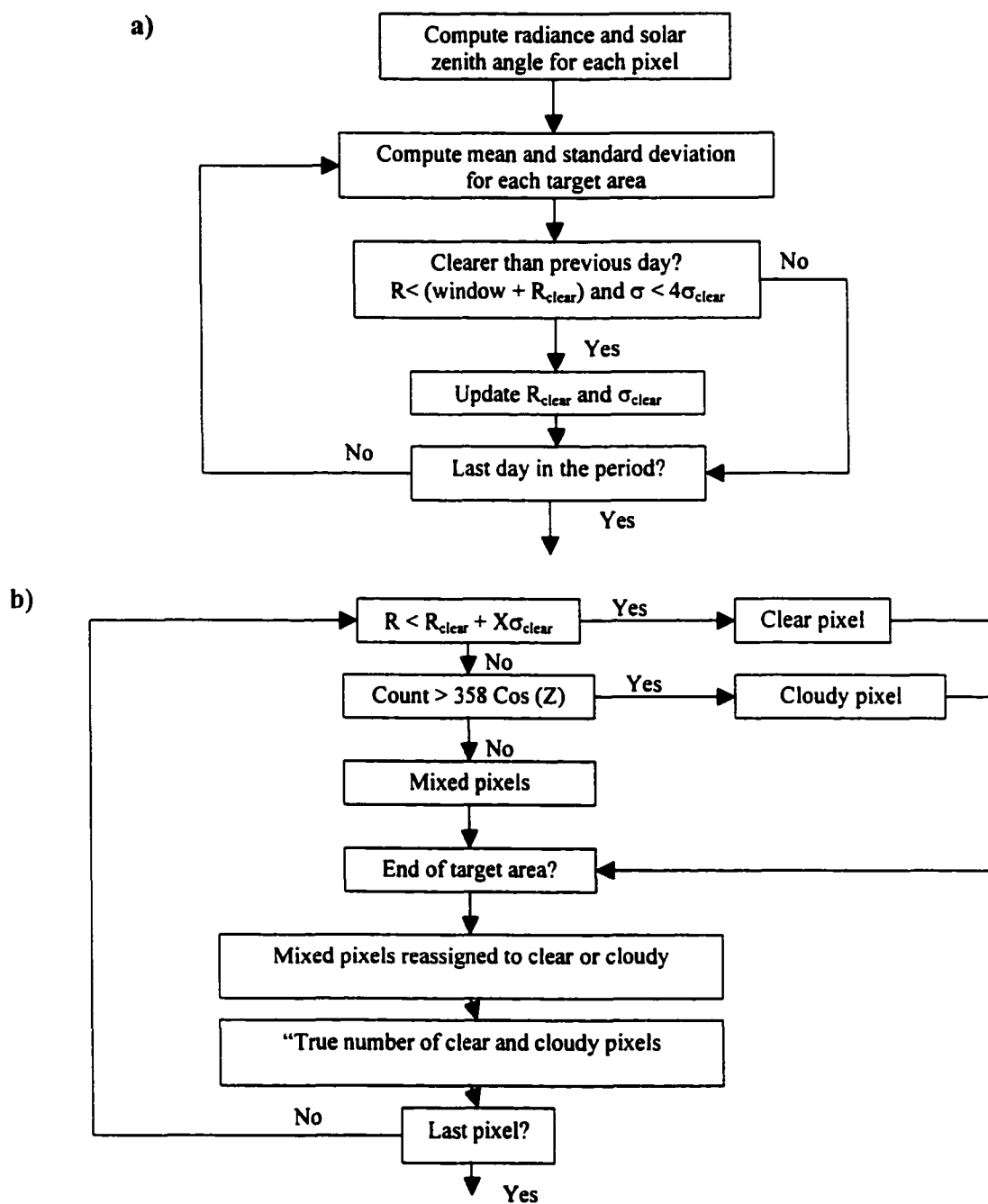


**Figure 4.1** (a) Flow chart of the procedure used to estimate the clear-sky reflectance for each of the 4 x 4 km target areas in the real-time tracking. (b) Flow chart of the procedure used to assign pixels in each target area into the “clear-sky” and “cloud-covered” categories.

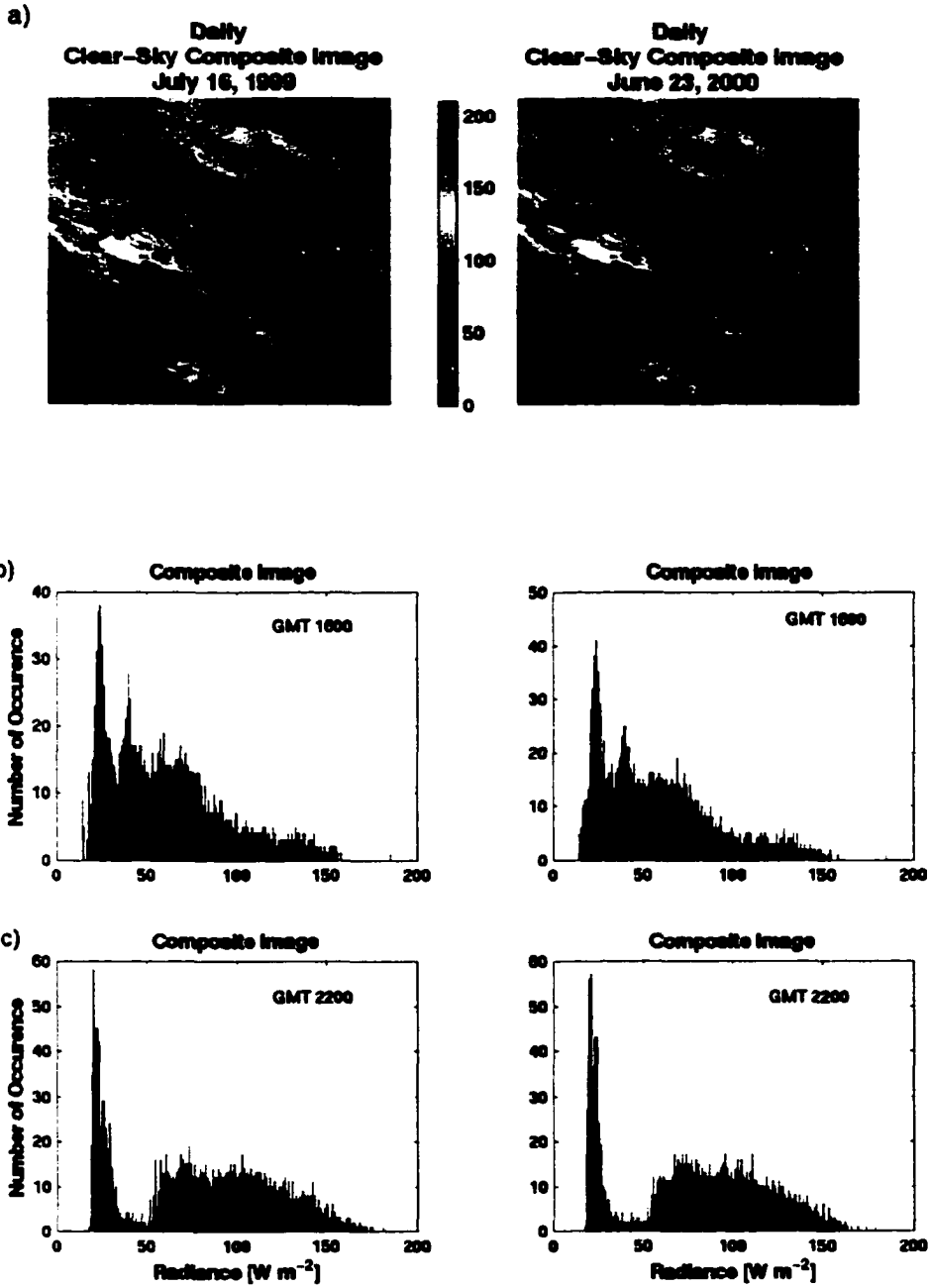


Figure 4.2 (a) Daily average clear-sky composite radiances for July 16, 1999 and for June 23, 2000. (b) The frequency distributions for clear-sky composite radiance at GMT 1600 for July 16, 1999 and for June 23, 2000, while the same histograms are shown for the GMT 2200 in (c).

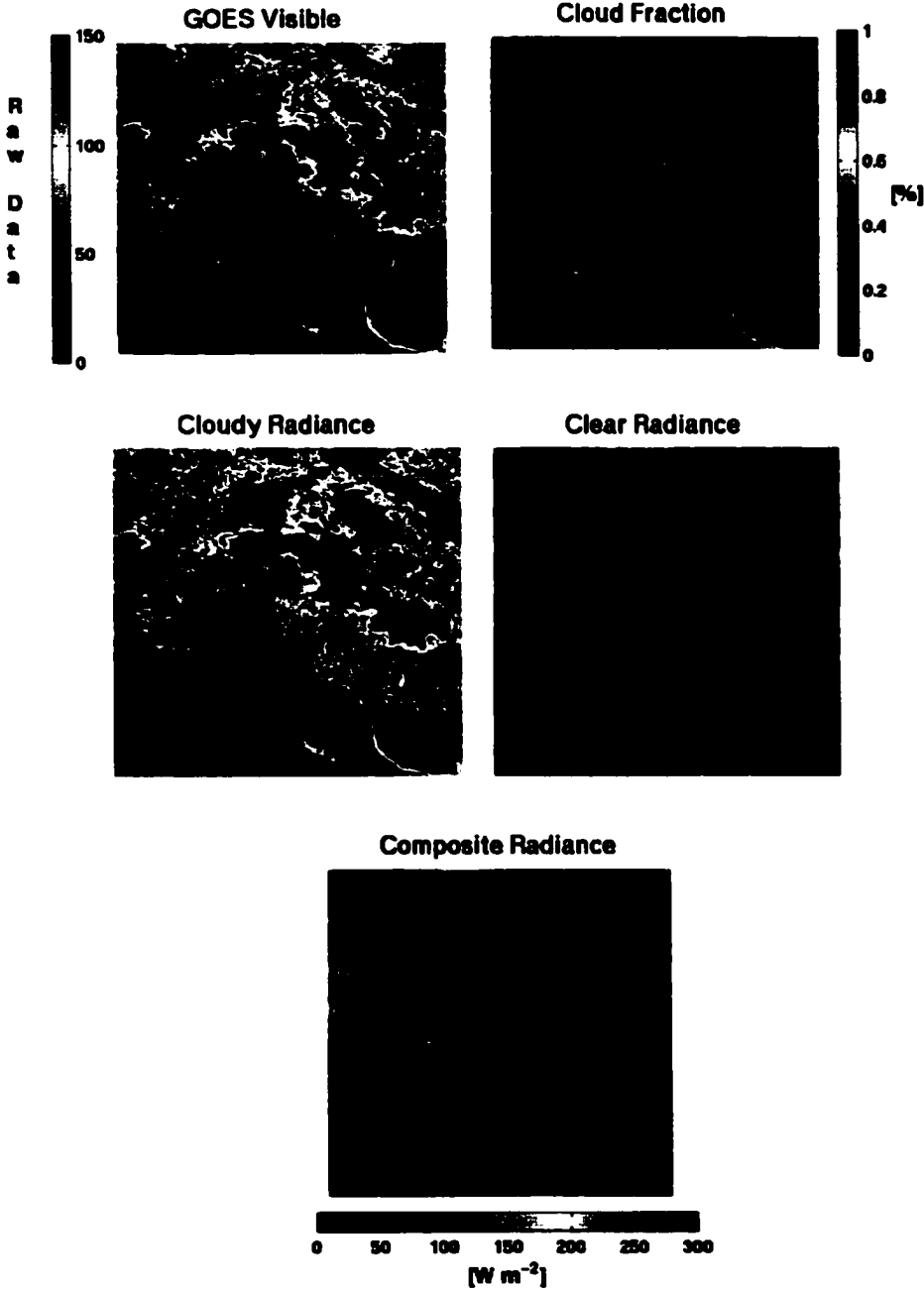


Figure 4.3 The GOES visible image and the main outputs from the cloud-screening algorithm, specifically the cloud fraction, and the cloudy, clear and composite radiance images for July 14, 1999 at GMT 2200.

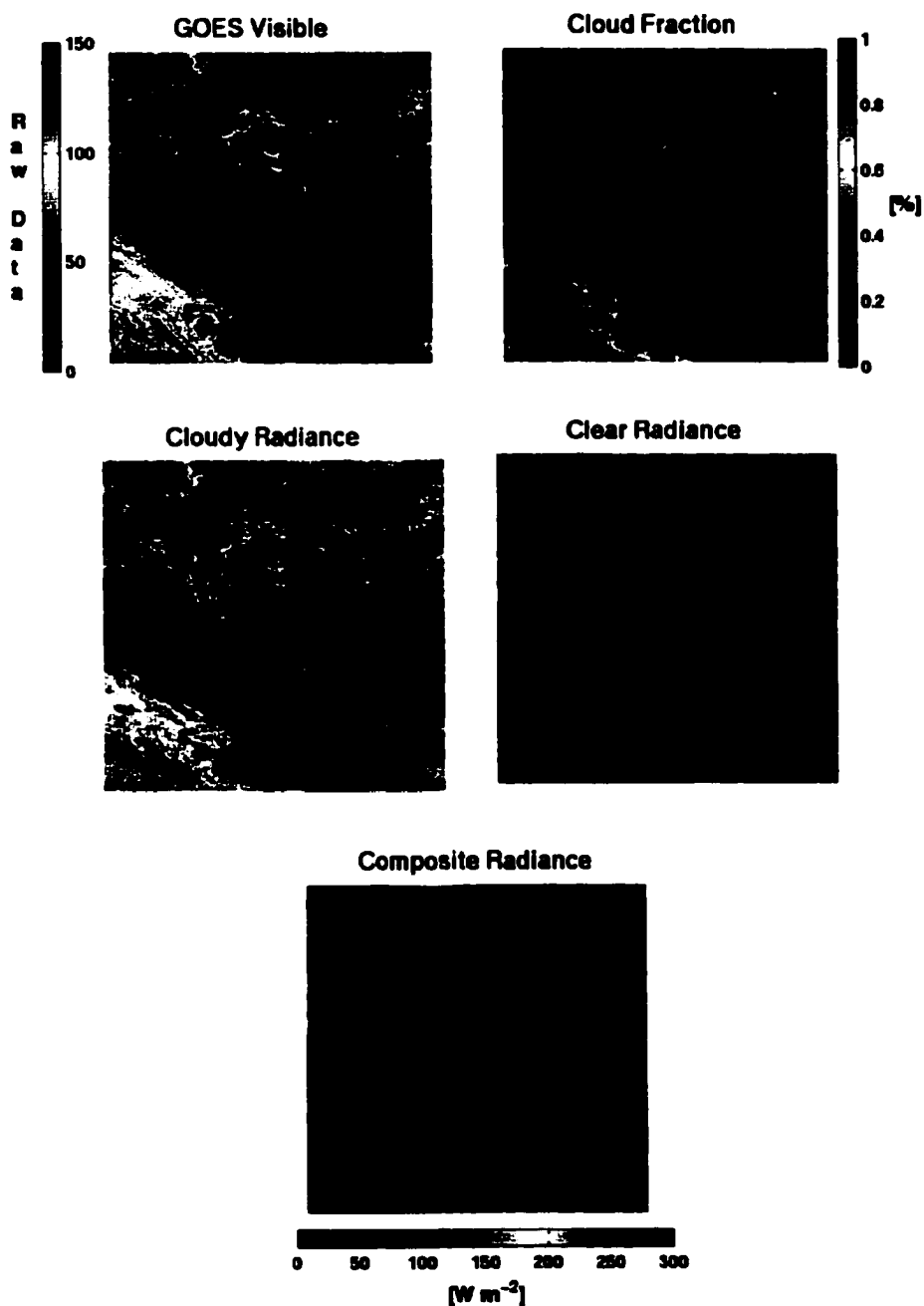


Figure 4.4 The GOES visible image and the main outputs from the cloud-screening algorithm, specifically cloud fraction, and the cloudy, clear and composite radiance images on June 22, 2000 at GMT 2000.

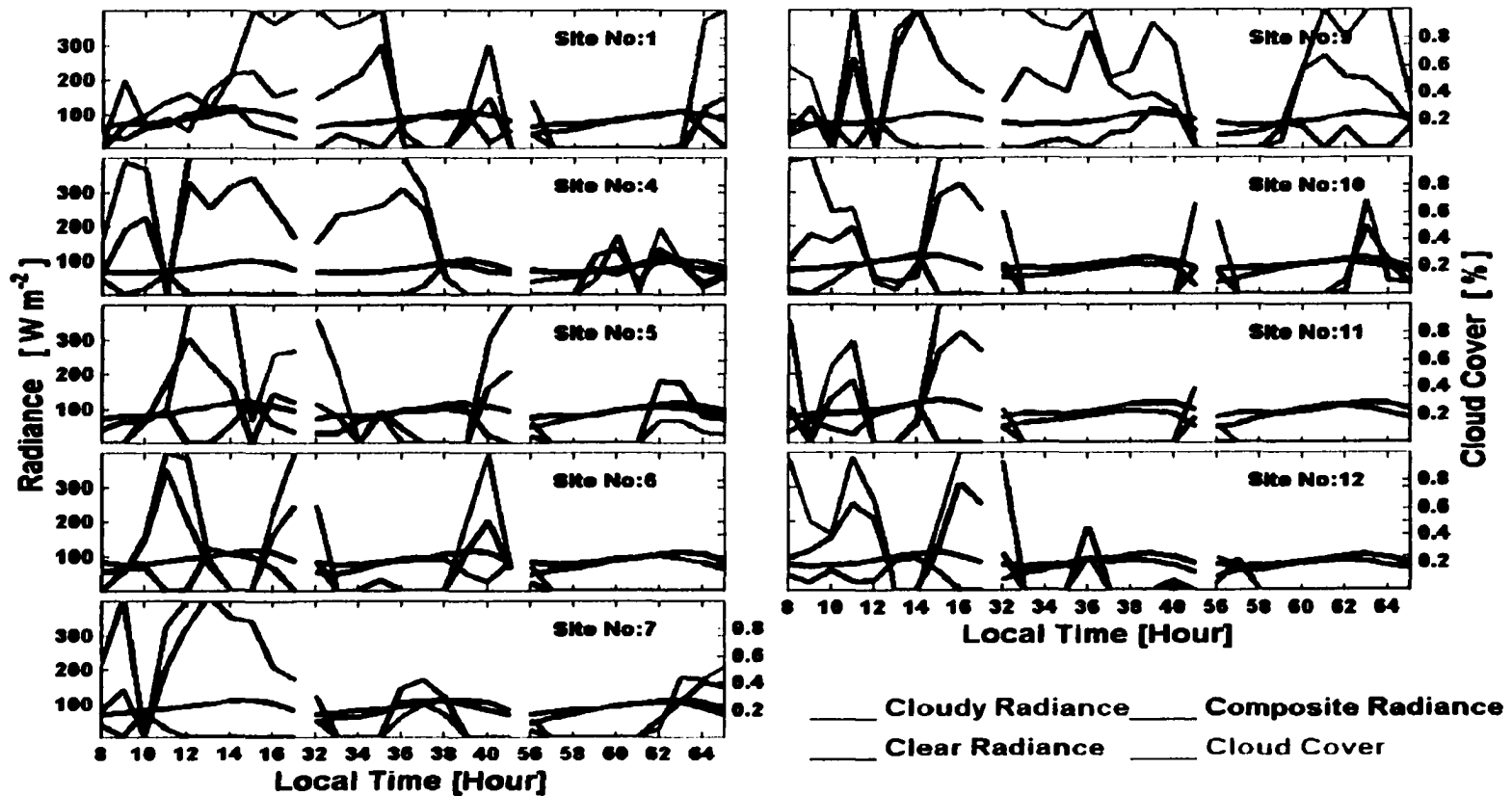


Figure 4.5(a) Time series of cloudy radiance, clear radiance, composite radiance, and cloud cover over the AZMET sites for July 14-16, 1999.

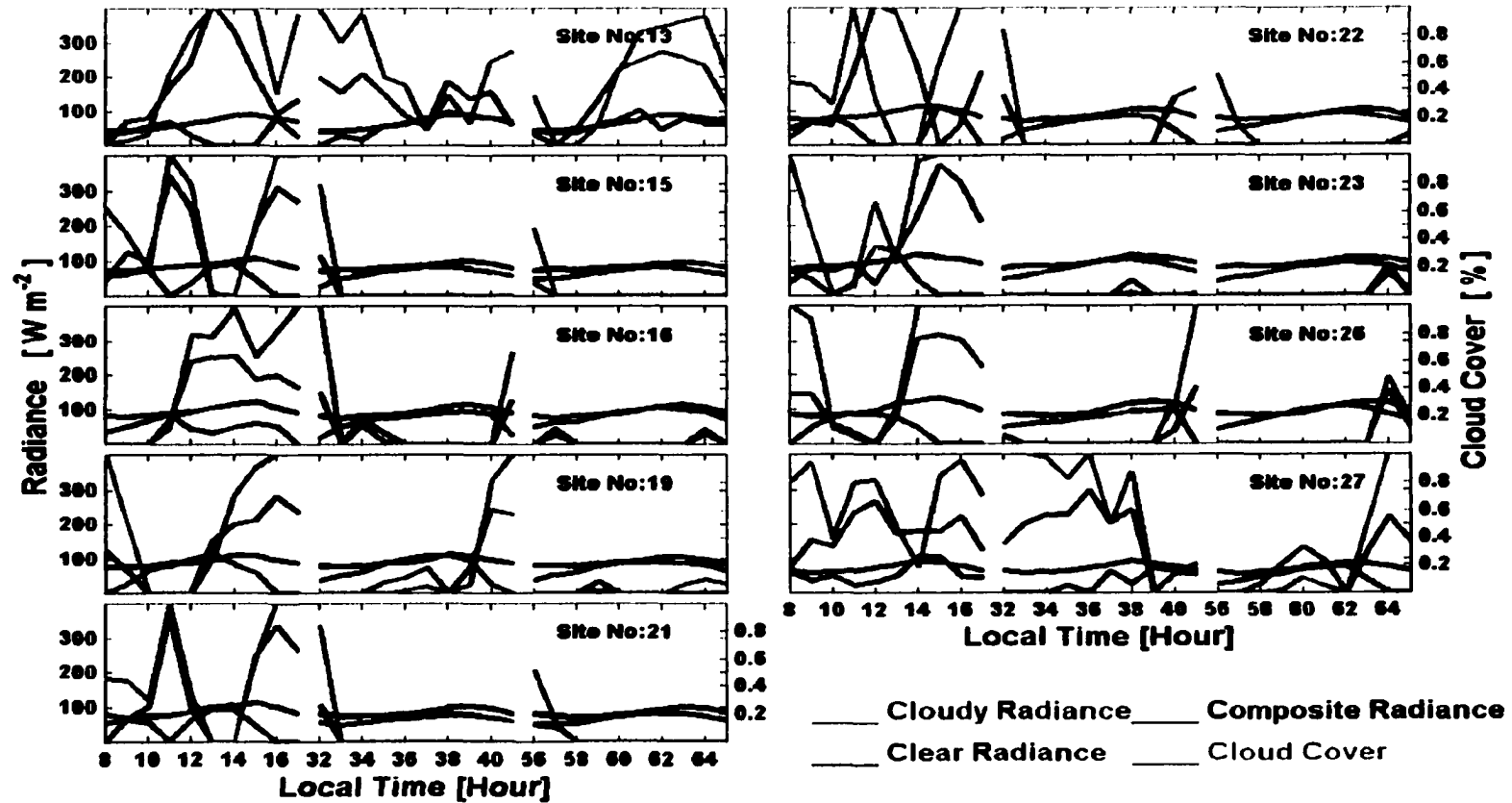


Figure 4.5(b) Time series of cloudy radiance, clear radiance, composite radiance, and cloud cover over the AZMET sites for July 14-16, 1999.

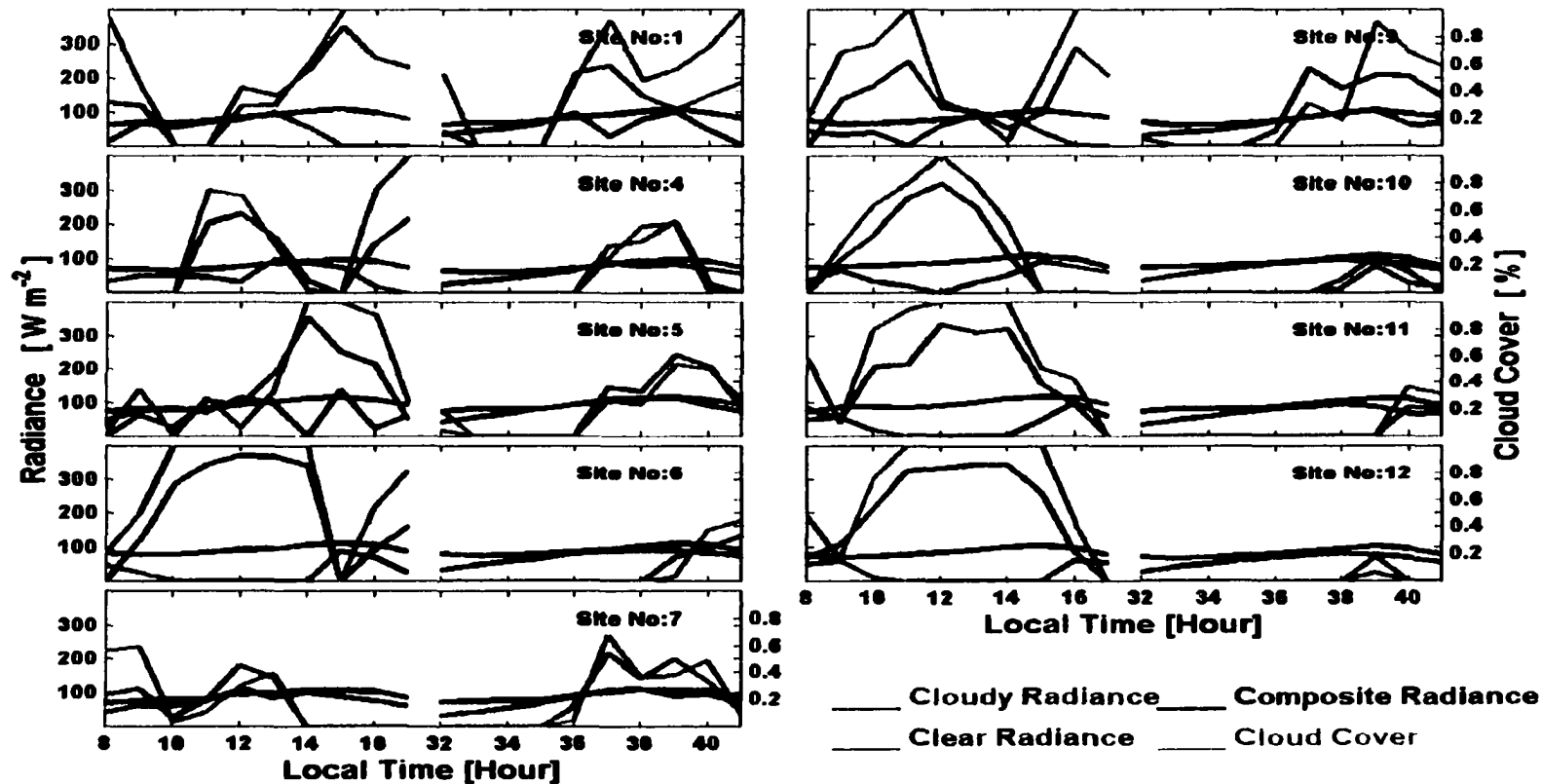
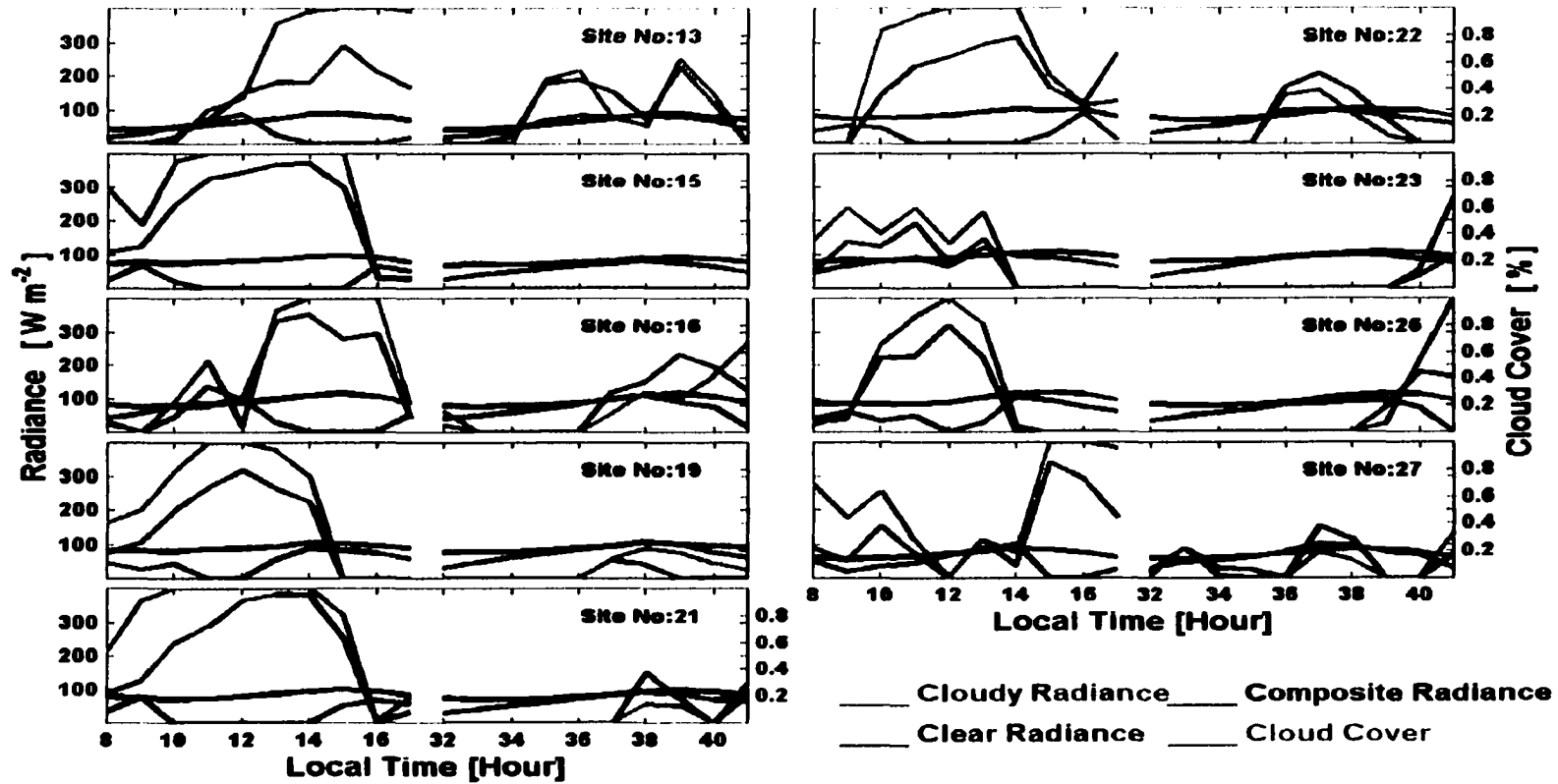


Figure 4.6(a) Time series of cloudy radiance, clear radiance, composite radiance, and cloud cover over the AZMET sites for June 22-23, 2000.



**Figure 4.6(b) Time series of cloudy radiance, clear radiance, composite radiance, and cloud cover over the AZMET sites for June 22-23, 2000.**

## **CHAPTER 5**

### **ASSIMILATING SATELLITE DATA**

#### **5.1 Introduction**

Data assimilation has long been recognized as an important tool for providing initial conditions for numerical model prediction and, more recently, it has also been recognized as a mechanism for improving modeled diagnostic fields. Observations from satellites, aircraft, radiosondes, and land stations have been incorporated to the meteorological models in the major weather forecasting centers, such as those at the U.S. National Meteorological Centers and the U.K. Meteorological Office, using a variety of data assimilation methods. Some of the different data assimilation techniques available were explored and evaluated by Houser (1996) in the context of using remotely sensed soil moisture in four-dimensional data assimilation (4DDA) for hydrological applications. Common among these methods, for instance, is the variational technique, which describes, quantifies and minimizes the distance between observational and model values. However, in order to enhance simplicity of description and allow more ready appreciation of the value of the remotely sensed cloud cover data, the assimilation technique applied in this research involved direct replacement of model estimates with values based on satellite observations.

The combining remotely sensed data with model-calculated fields enables the provision of high-resolution, hydrologically relevant near surface meteorological data in data-sparse areas. Consequently, assimilation of satellite data into the coupled

atmosphere and hydrologic models is likely to play a key role in characterizing both spatial and temporal atmospheric and/or hydrologic variability by facilitating the construction of more accurate and continuous data fields. Recently, a theory supporting the simultaneous assimilation of remotely sensed data such as surface radiation, land cover, cloud cover, into a coupled land surface-atmosphere model to give improved diagnosis of land-surface energy exchanges has been developed (Shuttleworth, 1999). This chapter describes the first step towards implementing that theory, specifically the assimilation of high-resolution fields cloud cover and, implicitly, radiation derived from satellite observations into meteorological models to give accurate, continuous, and continuous data fields of surface energy and water exchanges, which are important for hydrological applications because they control the regional climate system.

## **5.2 Assimilating Satellite-Derived Solar Radiation**

Based on comparison between model results and observations, prior application of the RAMS model demonstrated uncertainty in the calculated solar radiation fields although, on clear days, the model output agreed reasonably well with the observed data. The inconsistencies primarily arose in areas that are modeled by RAMS as being cloud free but which were observed to be cloudy. In a first attempt to redress this model weakness, an attempt was made to use satellite-derived estimates of surface solar radiation fields to correct the modeled net radiation at the surface. High resolution fields of cloudy radiance, clear radiance and cloud fraction derived from GOES observations using the cloud screening algorithm, along with the clear sky composite radiance and

precipitable water were used in the UMD GEWEX/SRB model to produce estimates of the solar radiation components at 4 km x 4 km pixel scale. The required atmospheric precipitable water fields were obtained from the Eta model, but with adjustment made for the topography used in the RAMS model. (Note: a fallback procedure, which used climatological fields of precipitable water when these fields were not available from the Eta model, was also developed.)

An example comparison between observations and remotely sensed estimates surface solar radiation fluxes from this algorithm is given in Figure 5.1. These comparisons were made at 4-km pixel scale and correspond to a field site near Obregon in Mexico and a field site in the San Pedro River basin in Arizona. The satellite derived radiation fluxes clearly demonstrate a reasonable ability to track the effects of clouds with no overall bias and, as Pinker et al. (1994) point out, they are superior to many model-calculated estimates. However, in Figure 5.1(b)-(c), there remains a considerable amount of scatter which is due in part to differences in the sampling of the satellite (an instantaneous, area-average) and ground-based sensor (a time average, point sample). Some of the bias in clear-sky values may be attributable to errors in estimating the surface albedo. Additionally, the field observations are lower (by about  $\sim 100 \text{ Wm}^{-2}$ ) than satellite data in Obregon, but higher (by about  $\sim 100 \text{ Wm}^{-2}$ ) than satellite data at the San Pedro site. There were suggestions that field data may be systematically wrong (by  $\sim 5\%$ ) at these sites.

The promising evidence provided typified by the above comparisons stimulated further investigation in which the remotely sensed surface solar radiation were routinely

assimilated into the RAMS model in an attempt to obtain more accurate modeled estimates of surface fluxes. In practice, the surface short-wave radiation estimates were simply inserted into the model to replace the modeled values every 15 minutes (at which frequency the model's radiation tendency is also updated, this replacement being made using the following expression:

$$S_{i,j} = I_{i,j}^{SAT} \cdot (1 - a_{i,j}) \quad (5.1)$$

where  $i,j$  refers to model's horizontal 4-km grid position,  $S_{i,j}$  is the model's net short-wave radiation in  $\text{Wm}^{-2}$  absorbed at the surface,  $I_{i,j}^{SAT}$  is the satellite-estimated incoming surface short-wave radiation in  $\text{Wm}^{-2}$ , and  $a_{i,j}$  is the model's surface albedo. Figure 5.2 compares absorbed short-wave radiation calculated (a) without and (b) with the benefit of satellite data. There is, of course, a significant impact of this assimilation on the values and spatial distribution of absorbed short-wave radiation in the model. However, although this initial data assimilation study greatly increased the accuracy of the model-calculated net short-wave radiation at the surface, it also revealed some problems. For instance, incoming long-wave radiation fluxes retained their relatively low, clear-sky values the cloud cover simulated in RAMS remained unchanged. In semi-arid areas such as Southern Arizona – the area used in this study – the difference in long-wave radiation between cloud-free and cloud covered areas can easily exceed  $100 \text{ Wm}^{-2}$ . A further important inconsistency is that the RAMS model still generally underestimated precipitation. This motivated exploration of the feasibility of directly assimilating cloud optical depth directly into RAMS as an alternative, preferable approach.

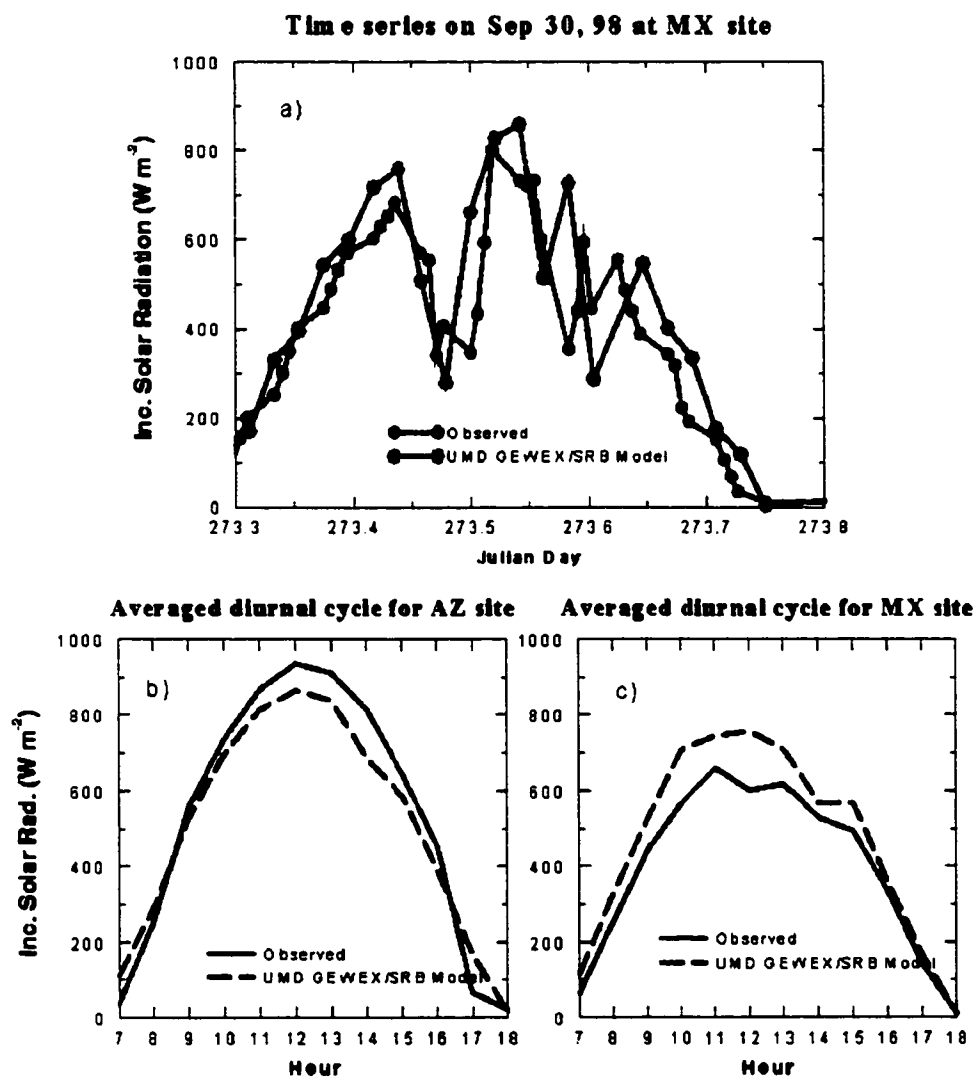


**Figure 5.1** (a) Comparison between observed incoming solar radiation and incoming solar radiation computed using the UMD GEWEX/SRB model for a field site near Obregon in Mexico on September 30, 1998. (b) and (c) average diurnal cycle observed incoming solar radiation and incoming solar radiation computed using the UMD GEWEX/SRB during 1998 for a field site near Obregon in Mexico and a field site in the San Pedro River basin, respectively.

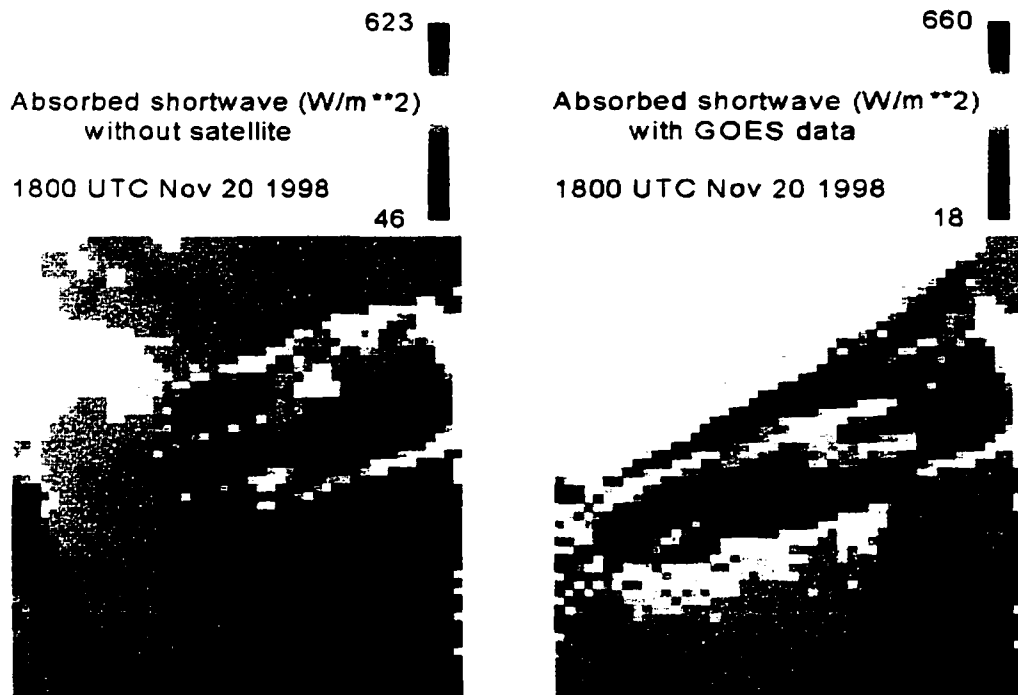


Figure 5.2 Comparison of RAMS-calculated absorbed net short-wave radiation (a) without, and (b) with GOES data.

### 5.3 Assimilating Satellite-Derived Cloud Cover

The critical realization that allows assimilation of cloud cover into RAMS is that the cloudy sky, clear sky, and composite radiances provided by the cloud screening algorithm and cloud fraction used in the UMD GEWEX/SRB model are intimately related to the cloud albedo, cloud optical depth, and cloud water/ice simulated in the RAMS model. This relationship (Equation 2.15) was used to derive an estimate of the vertically integrated cloud water/ice that was directly assimilated into the RAMS model to update the modeled cloud cover. However, because satellite images can only provide

information on the horizontal position of cloud water/ice in the modeled domain, it is necessary to generate/postulate a vertical fractional cloud mass profile to distribute cloud water/ice within the vertical profile in each modeled grid square. In this study, it was assumed that, on average across the modeled domain, RAMS calculates the vertical position of cloud correctly even if it miscalculates total cloud amount in the atmospheric column as a whole. We therefore create and assimilate a cloud field whose horizontal distribution is determined using an image derived from GOES but whose vertical distribution is that of the domain-average cloud field calculated by RAMS in the time step immediately prior to each cloud assimilation. Cloud assimilation was then made incrementally, every minute, with linear interpolation used to derive cloud images for each minute between two successive GOES images. Figure 5.3 indicates the steps used to prepare cloud water and ice fields for use in the RAMS model.

### 5.3.1 Whole-Column Cloud Water and Ice Estimated from Satellite

The UMD GEWEX/SRB model provides estimates of cloud optical depth,  $\tau_{i,j}$ , for the  $N_i \times N_j$  (4 km x 4 km) target areas within the domain. The RAMS model grid is also 4 km x 4 km, and this grid is collocated with the target areas in the satellite image by applying a weighted interpolation between two grid projection system. The cloud optical depth values were interpolated to the RAMS grid for a given model domain as illustrated in Figure 5.4. It is assumed that there is a known relationship between  $m_{i,j}^{CL,SAT}$ , the mass (in kg) of cloud water and ice in the atmosphere above the model grid square ( $i, j$ ), and

the satellite-derived values of cloud optical depth, which is determined as function of cloudy sky radiance,  $L_{i,j}$  and fractional cloud cover,  $c_{i,j}$  thus:

$$\tau_{i,j} = f(c_{i,j}, L_{i,j})$$

and

$$m_{i,j}^{CL,SAT} = 10^{\exp[(\log(\tau_{i,j}) - 0.26)/1.71]} \, di \, dj \quad (5.2)$$

where the right side of this equation is substituted from Equation 2.15 and  $(di \, dj)$  is the area (in  $m^2$ ) of a horizontal grid square. Although there is no discrimination between cloud liquid water and ice water derived from the satellite image, RAMS estimates liquid and ice components of cloud separately, as explained previously. Therefore, satellite-derived cloud water/ice fields are assimilated into RAMS according to the fractions of each component simulated by the model within the atmospheric column above the model grid-square.

### 5.3.2 Fractional Cloud Mass Profiles Represented in RAMS Prior to Assimilation

Cloud assimilation algorithm was incorporated into the RAMS model code immediately following the model's diagnosis and/or prognosis of cloud water and ice fields. If the satellite image indicates cloud water/ice for a particular 4 km x 4 km grid-square in modeled domain, prior to cloud assimilation, RAMS calculates values of air temperature,  $T_{i,j,k}$ , air pressure,  $p_{i,j,k}$ , mixing ratios for total water,  $r_{i,j,k}^T$ , for cloud water,  $r_{i,j,k}^C$ , for rain water,  $r_{i,j,k}^R$ , for hail,  $r_{i,j,k}^H$ , for graupel,  $r_{i,j,k}^G$ , for aggregate,  $r_{i,j,k}^A$ , for snow,

$r_{i,j,k}^S$ , for pristine,  $r_{i,j,k}^P$ , and for water vapor,  $r_{i,j,k}^V$ , respectively at each vertical level,  $k$ , above each model grid square ( $i, j$ ) where satellite observed clouds. The corresponding density of dry air,  $\rho_d$  (in  $\text{kgm}^{-3}$ ) and vapor pressure for water vapor,  $e$  (in kPa), are calculated by the following equations:

$$\rho_d = 0.622 \cdot p_{i,j,k} / (0.622 \cdot R_d \cdot T_{i,j,k} + R_d \cdot T_{i,j,k} \cdot r_{i,j,k}^V) \quad (5.3)$$

and

$$e = \rho_d \cdot (R_d / 0.622) \cdot r_{i,j,k}^V \cdot T_{i,j,k} \quad (5.4)$$

where  $R_d (=287 \text{ Jkg}^{-1}\text{K}^{-1})$  is the dry air gas constant.

The mass of water vapor,  $m_{i,j,k}^V$ , and the mass of water as cloud water,  $m_{i,j,k}^C$ , rain water,  $m_{i,j,k}^R$ , hail,  $m_{i,j,k}^H$ , graupel,  $m_{i,j,k}^G$ , aggregate,  $m_{i,j,k}^A$ , snow,  $m_{i,j,k}^S$ , pristine,  $m_{i,j,k}^P$ , (all in kg) in a parcel of the atmosphere with volume  $V_{i,j,k}$  can then be calculated from their respective mixing ratios and the vapor pressure, air pressure, and temperature of the air parcel, thus:

$$m_{i,j,k} = \frac{(p_{i,j,k} - e) \cdot V_{i,j,k} \cdot r_{i,j,k}}{R_d \cdot T_{i,j,k}} \quad (5.5)$$

Thus, using this last equation, the mixing ratios ( $r_{i,j,k}$ ) of the water species water vapor, cloud water, rain water, hail, graupel, aggregate, snow, and pristine, respectively, are used to calculate their corresponding water masses ( $m_{i,j,k}$ ). The total mass of cloud water

and ice produced in the atmospheric column above model grid-square in the modeled domain is then calculated as follows:

$$M_{i,j}^{CLRAMS} = \sum_k^{N_k} m_{i,j,k}^C + \sum_k^{N_k} m_{i,j,k}^R + \sum_k^{N_k} m_{i,j,k}^H + \sum_k^{N_k} m_{i,j,k}^G + \sum_k^{N_k} m_{i,j,k}^A + \sum_k^{N_k} m_{i,j,k}^S + \sum_k^{N_k} m_{i,j,k}^P \quad (5.6)$$

where  $k$  refers to each atmospheric level along the atmospheric column and  $N_k$  ( $= 28$ ) is the number of vertical levels in the model.

Finally, if total mass of cloud water and ice,  $M_{i,j}^{CLRAMS}$ , in each atmospheric column where satellite observed clouds is greater than zero (meaning that RAMS also produces some clouds for this particular column after assimilation), vertical cloud fractions at each vertical level for a given grid-square are simply given by:

$$f_{k,i,j}^C = \frac{m_{i,j,k}^C}{M_{i,j}^{CLRAMS}}, \quad f_{k,i,j}^R = \frac{m_{i,j,k}^R}{M_{i,j}^{CLRAMS}}$$

$$f_{k,i,j}^H = \frac{m_{i,j,k}^H}{M_{i,j}^{CLRAMS}}, \quad f_{k,i,j}^G = \frac{m_{i,j,k}^G}{M_{i,j}^{CLRAMS}} \quad (5.7)$$

$$f_{k,i,j}^A = \frac{m_{i,j,k}^A}{M_{i,j}^{CLRAMS}}, \quad f_{k,i,j}^S = \frac{m_{i,j,k}^S}{M_{i,j}^{CLRAMS}}, \quad f_{k,i,j}^P = \frac{m_{i,j,k}^P}{M_{i,j}^{CLRAMS}}$$

where  $f_{k,i,j}$ 's are vertical cloud mass profiles for cloud water, rain water, hail, graupel, aggregate, snow, and pristine, respectively.

If  $M_{i,j}^{CLRAMS}$  is equal to zero (meaning that RAMS does not produce any clouds for this particular column but the satellite observes clouds), cloud water must be created

at vertical levels. In this case, it is assumed that only cloud water (rather than other cloud components) will be created, because cloud water is the basis for creating the other cloud water species in the model. Such cloud water is created at the most appropriate level in the atmospheric column. For instance, it is produced at the levels where the air is closest to saturation until  $M_{i,j}^{CL,RAMS}$  is greater than  $m_{i,j}^{CL,SAT}$ . To do this it is assumed that there is some critical value of relative humidity,  $RH_c$ , which is constant through the vertical profile. At each level in the atmospheric column, water vapor in excess of this value of relative humidity is reassigned to cloud water to make  $M_{i,j}^{CL,RAMS}$  greater than  $m_{i,j}^{CL,SAT}$ . However, the appropriate value of  $RH_c$  is not known *a priori* at each time step, so an appropriate value must be found by iteration. Thus, starting with  $RH_c$  set to 1, the value is reduced (in steps of  $\delta RH$ ) until the above criterion is satisfied or until  $RH_c$  is zero, whichever occurs first. As soon as one of these two criteria is satisfied, it is assumed that newly created vertical profile of cloud water given by adding in the water vapor from the air above  $RH_c$  is correct in relative terms. Once calculated, these newly created values of cloud water can then be used to calculate the fractional mass of cloud at each vertical level in the atmospheric column as above, i.e. from

$$f_{k,i,j}^C = \frac{m_{i,j,k}^C}{M_{i,j}^{CL,RAMS}} \quad (5.8)$$

The fractional masses for other cloud species are set equal to zero at this stage, but will evolve as the model runs.

### 5.3.3 Updating the RAMS Cloud Field and Air Temperature

Once the fractional mass or cloud at each vertical level in the atmospheric column has been calculated as above, a new mass of cloud water, rain water, hail, graupel, aggregate, snow, and pristine in each parcel  $(i, j, k)$  of the atmosphere can be calculated from:

$$\begin{aligned}
 (m_{i,j,k}^{C,RAMS})_{new} &= f_{k,i,j}^C m_{i,j}^{CL,SAT}, & (m_{i,j,k}^{R,RAMS})_{new} &= f_{k,i,j}^R m_{i,j}^{CL,SAT} \\
 (m_{i,j,k}^{H,RAMS})_{new} &= f_{k,i,j}^H m_{i,j}^{CL,SAT}, & (m_{i,j,k}^{G,RAMS})_{new} &= f_{k,i,j}^G m_{i,j}^{CL,SAT} \\
 (m_{i,j,k}^{A,RAMS})_{new} &= f_{k,i,j}^A m_{i,j}^{CL,SAT}, & (m_{i,j,k}^{S,RAMS})_{new} &= f_{k,i,j}^S m_{i,j}^{CL,SAT} \\
 (m_{i,j,k}^{P,RAMS})_{new} &= f_{k,i,j}^P m_{i,j}^{CL,SAT}
 \end{aligned} \tag{5.9}$$

A revised mixing ratio for cloud water, rain water, hail, graupel, aggregate, snow, and pristine is then recalculated from:

$$r_{i,j,k} = \frac{R_d \cdot T_{i,j,k} \cdot (m_{i,j,k}^{RAMS})_{new}}{V_{i,j,k} (\rho_{i,j,k} - e)} \tag{5.10}$$

This equation is applied separately for each new water mass  $(m_{i,j,k})_{new}$  of cloud water, rain water, hail, graupel, aggregate, snow, and pristine to calculate their corresponding revised mixing ratios  $(r_{i,j,k})$ . Finally, the mixing ratio of total water,  $r_{i,j,k}^T$ , is updated by summing revised components of cloud water and ice, and vapor mixing ratios as follows:

$$r_{i,j,k}^T = r_{i,j,k}^V + r_{i,j,k}^C + r_{i,j,k}^R + r_{i,j,k}^H + r_{i,j,k}^G + r_{i,j,k}^A + r_{i,j,k}^S + r_{i,j,k}^P \tag{5.11}$$

If satellite does not assign any cloud cover for a particular atmospheric column above grid-square in modeled domain, any cloud amounts produced by the RAMS in that column are removed by assigning all the components of cloud water and ice to zero. In this case, air parcel  $(i,j,k)$  of the atmosphere is represented as being all in the vapor phase, thus:

$$r_{i,j,k}^T = r_{i,j,k}^V \quad (5.12)$$

In the original RAMS code, the model updates air temperature according to the newly determined cloud water and ice fields. This part of the code was placed into the cloud assimilation algorithm so that modeled air temperature is updated immediately after the mixing ratio of the cloud water and ice fields have been revised in accordance with the satellite data. The model temperature is updated using the following expressions:

$$qpcp = alvi \cdot r_{ice} + alvl \cdot n$$

and

$$T_{update} = 0.5 \cdot \left( T_{i,j,k} + \sqrt{T_{i,j,k} \cdot \left( T_{i,j,k} + \frac{4}{c_p} qpcp \right)} \right) \quad T_{i,j,k} > 253 \quad (5.13)$$

$$T_{update} = T_{i,j,k} \cdot \left( 1 + \frac{qpcp}{c_p \cdot 253} \right) \quad T_{i,j,k} < 253$$

and

$$(T_{i,j,k})_{new} = T_{update}$$

where  $alvi$  ( $= 2.83 \times 10^6$ ) and  $alvl$  ( $= 2.50 \times 10^6$ ) are fixed parameters in the model,  $r_{ice}$  and  $r_l$  are the revised mixing ratios of cloud ice water and cloud liquid water, respectively (Equation 2.2), and  $c_p$  ( $= 1004 \text{ Jkg}^{-1}\text{K}^{-1}$ ) is the specific heat at constant pressure.

### 5.3.4 Assimilation Using Different Frequencies

Tests of the impact on modeled fields of assimilating GOES-derived cloud fields at different frequencies into RAMS were carried out. Evaluation involved finding the magnitude of the error rendered by RAMS for a specified period. In each case, while no satellite data were assimilated into one run, satellite data were assimilated every 30-minute, 15-minute and 1-minute into a second, third and fourth run, respectively. The resulting cloud fields were evaluated against the cloud fields available as satellite images and relative to each other. An example comparison between the modeled fields given by RAMS without cloud assimilation and with cloud fields assimilated once every 30-minutes in July 14, 1999 is shown in Figure 5.5. It is obvious that RAMS without assimilation underestimates the magnitude of amount of cloud significantly and that it also distributes clouds wrongly in horizontal domain. Further, RAMS gives rapid degradation of the assimilated cloud field even at the first time step after assimilation by reintroducing aspects of the modeled cloud field prior to next assimilation. Moreover, RAMS has a predisposition to introduce a modeled “clumping” of cloud cover between assimilation cycles. Nonetheless, there is, on average, a significant improvement in RAMS ability to simulate both the overall amount and horizontal position of cloud when the observed cloud cover is assimilated every 30 minutes. The quality of the modeled

cloud fields is further enhanced when remotely sensed cloud cover images are assimilated every 15-minutes as shown in Figure 5.6.

However, although the quality of cloud fields is further enhanced with a 15-minute assimilation frequency, RAMS still tends to evolve “lumpy” clouds between assimilation cycles. Therefore, GOES-derived cloud fields were assimilated at higher frequency, i.e. at 1-minute intervals, at which time the assimilated cloud fields were derived using linear interpolation between two 15-minute GOES images. The cloud images equivalent to those shown in Figure 5.5 but, in this case, with interpolated cloud fields assimilated every minute are displayed in Figure 5.7. The tendency of RAMS to evolve “lumpy” clouds is now significantly reduced. Furthermore, there is substantial improvement in modeled horizontal distribution and the overall cloud amount when satellite data is assimilated each minute. On the basis of this research, it was concluded that, for the purposes of evaluating the impact of cloud assimilation on the surface energy and water balance, the optimum assimilation procedure is to linearly interpolated GOES images between the 15 minute samples, and to assimilate these every minute into the RAMS model.

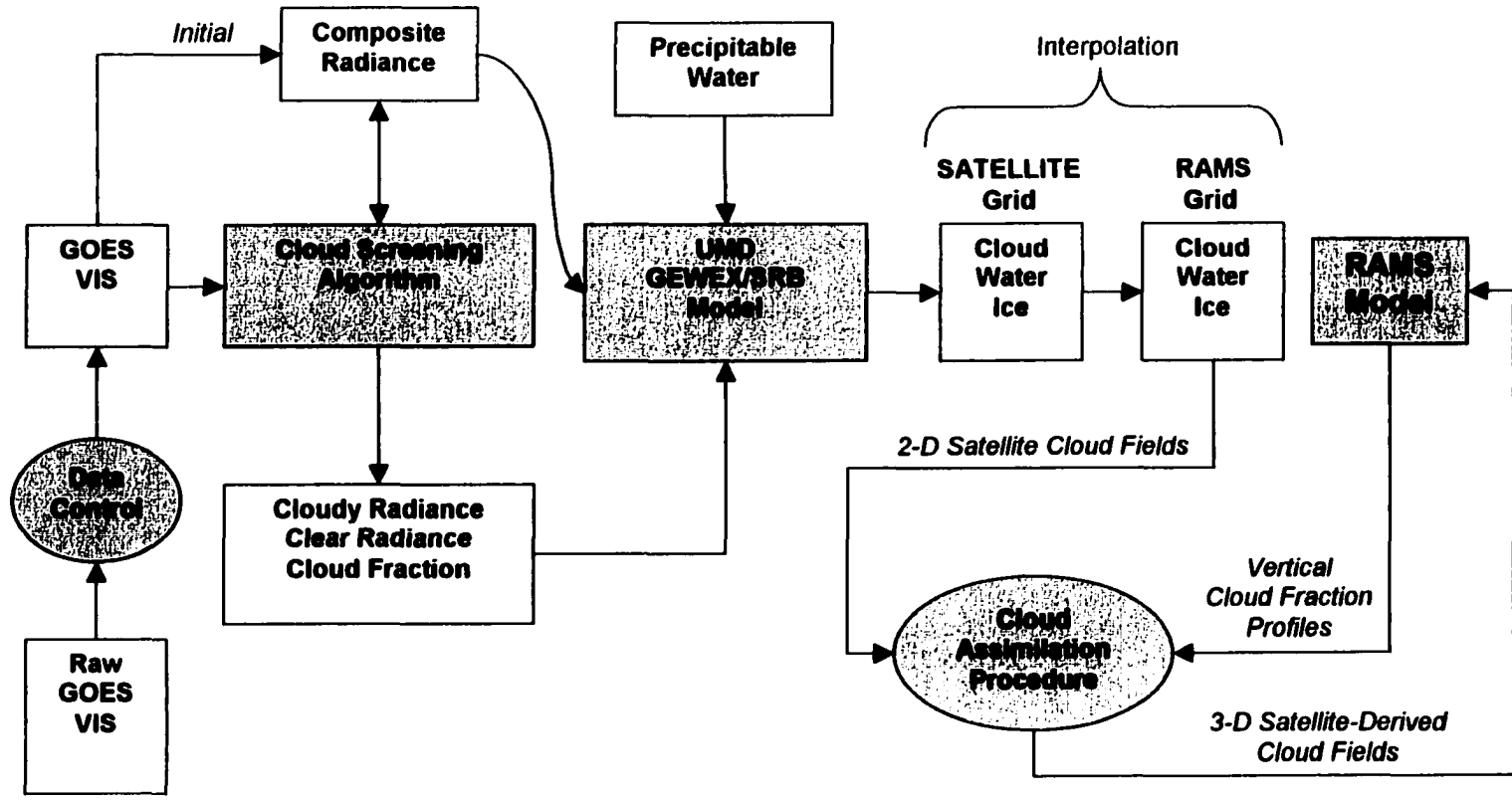


Figure 5.3 Diagram showing the entire steps for assimilating satellite-derived cloud fields into RAMS model.

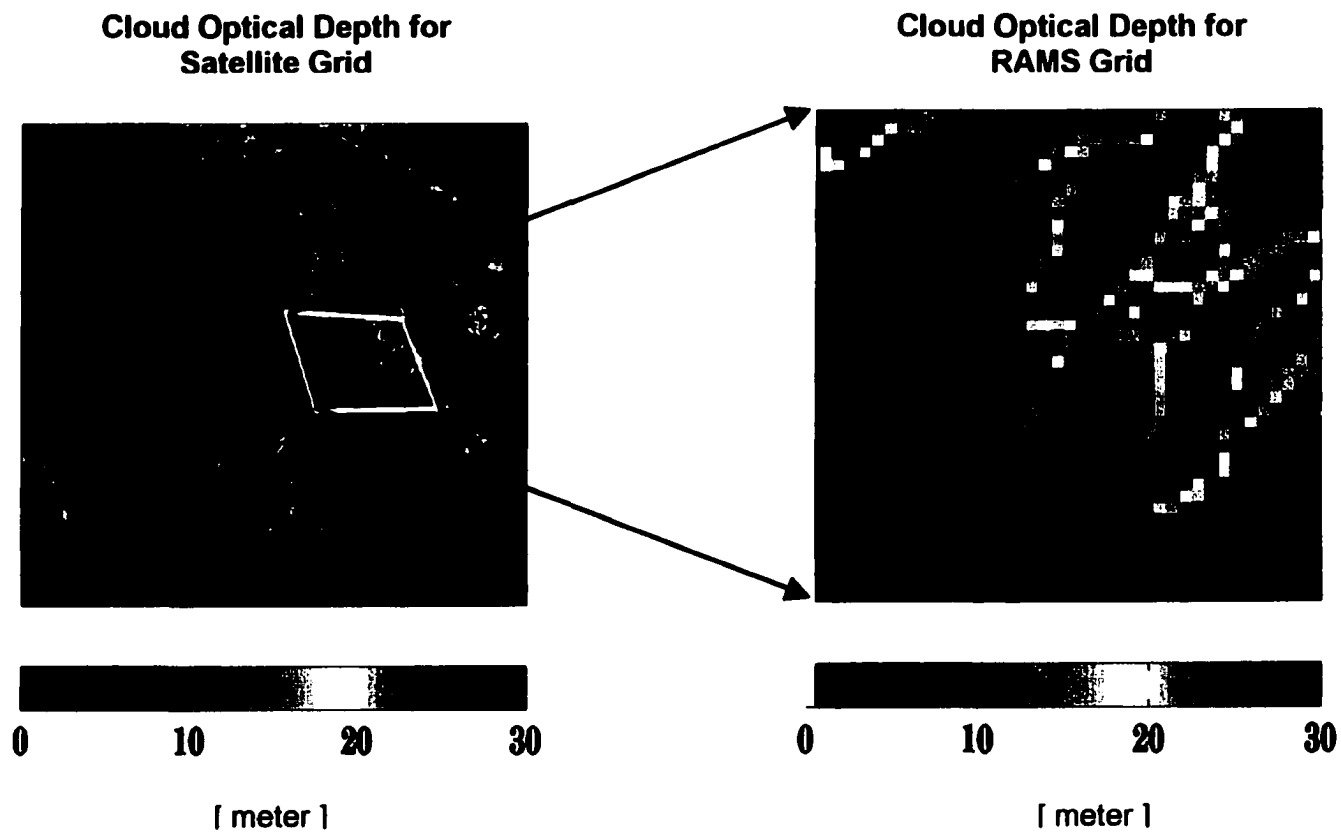


Figure 5.4 Application of weighted interpolation method for cloud optical-depth values. Solid line shows the RAMS model domain to where optical depth values were interpolated.

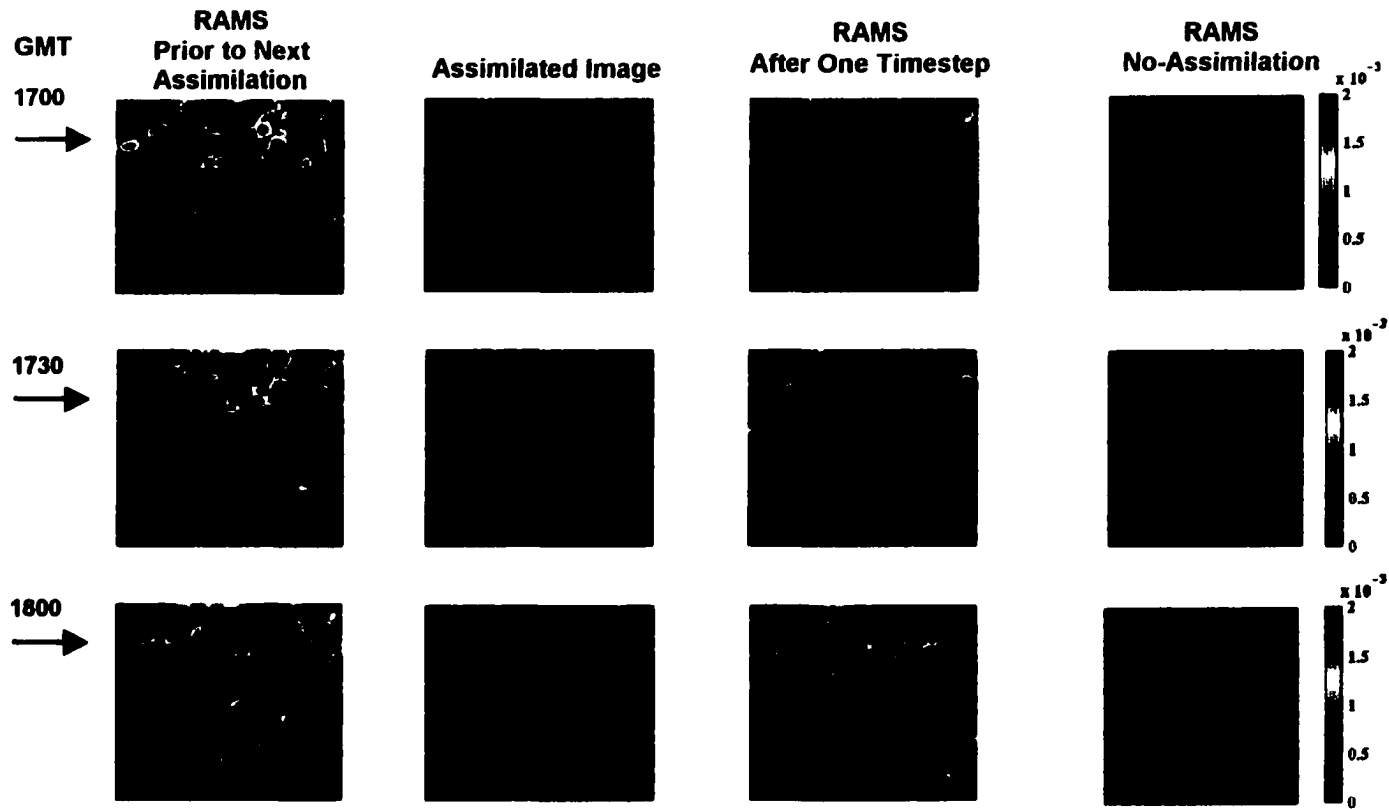


Figure 5.5 Comparison between the total cloud/ice mixing ratio in the vertical column across the modeled domain with observations derived from GOES images assimilated into RAMS at 30 minute intervals. The first column show values immediately before next assimilation takes place, the second column shows the assimilated cloud image, the third column shows the modeled field one time step after assimilation, while the fourth column shows the field calculated by RAMS when there is no assimilation of satellite observations. (Results on July 14, 1999)

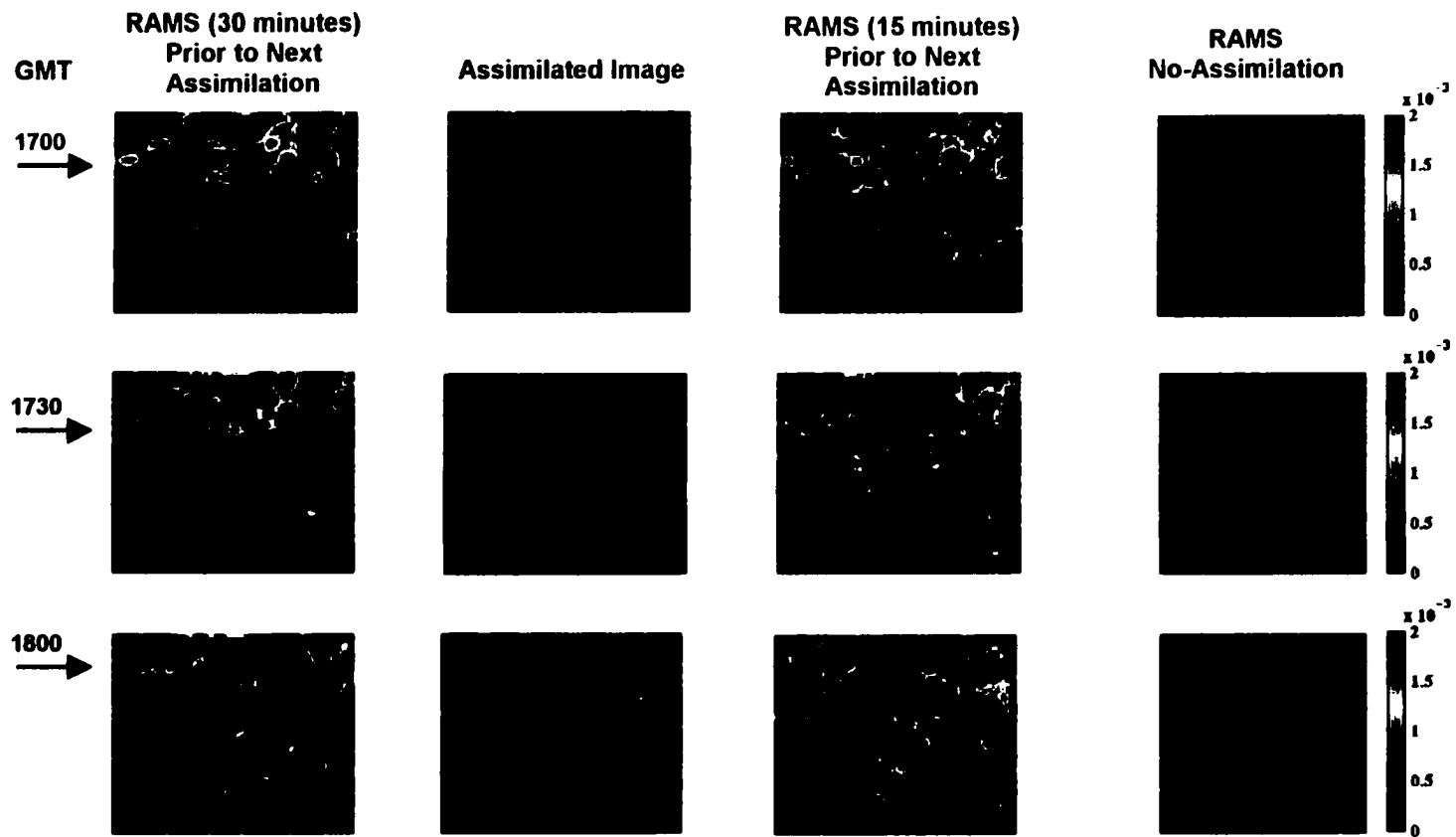
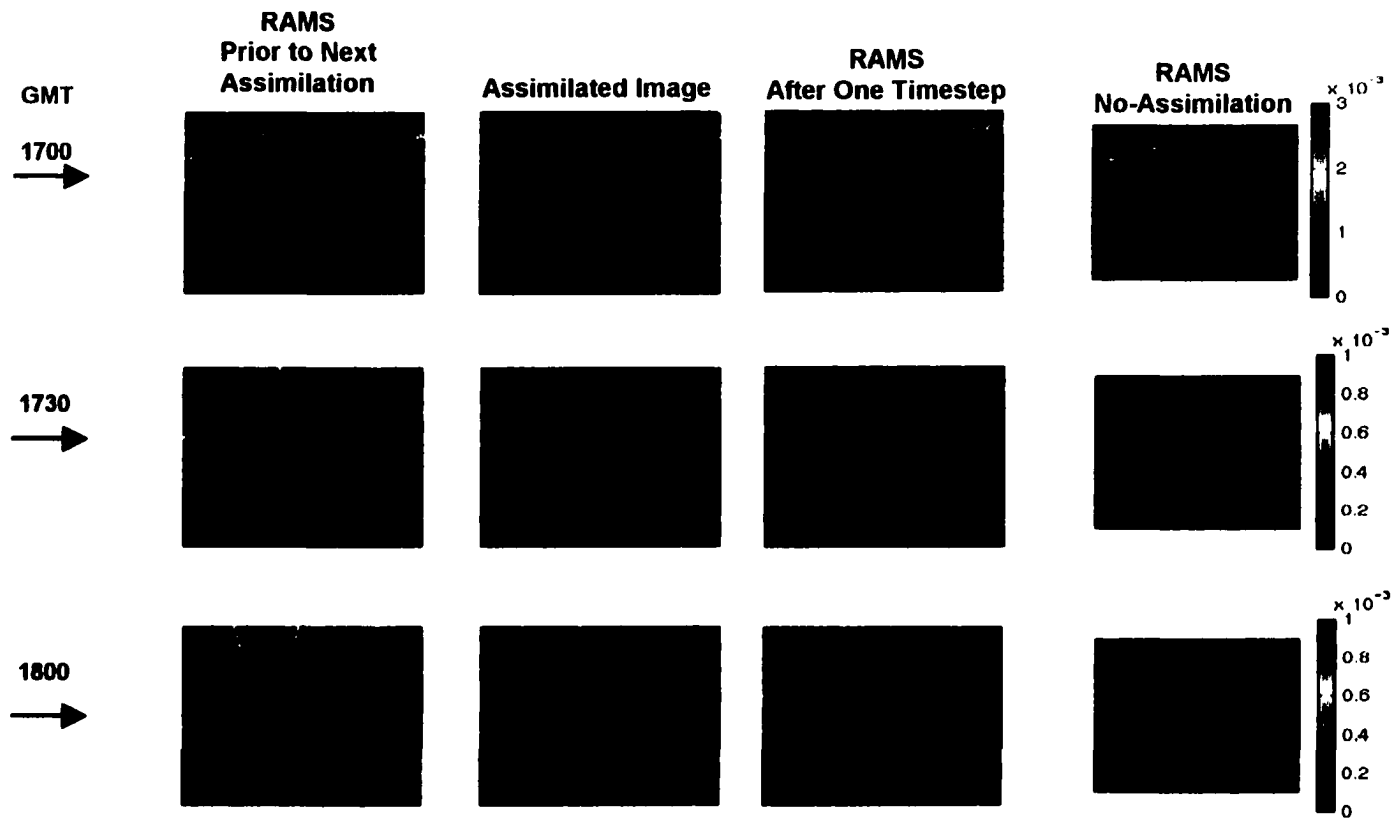


Figure 5.6 Comparison between the total cloud/ice mixing ratio in the vertical column across the modeled domain with observations derived from GOES images assimilated into RAMS at 15 minutes and 30 minutes, respectively. The first and third columns show values immediately before next assimilation takes place, the second column shows the assimilated cloud image, and the fourth column shows the field calculated by RAMS when there is no assimilation of satellite observations. (Results on July 14, 1999)



**Figure 5.7** Comparison between the total cloud/ice mixing ratio in the vertical column across the modeled domain with observations derived from GOES images assimilated into RAMS at every minute applying linear interpolation between image cycles. The first column show values immediately before next assimilation takes place, the second column shows the assimilated cloud image, the third column shows the modeled field one time step after assimilation, while the fourth column shows the field calculated by RAMS when there is no assimilation of satellite observations. (Results on July 14, 1999)

## **CHAPTER 6**

### **RESULTS**

#### **6.1 Evaluation**

As noted in Chapter 1, in meteorological models, cloud cover provides a critical linking control between the modeled short- and long-wave radiation fields and precipitation incident on the surface and the land surface energy and water balance. However, changes in cloud cover also affect the magnitude and spatial distribution of other atmospheric and near-surface weather variables in these models, such as wind speed and air temperature. Moreover, there is a possibility that model initiation may alter the results. Consequently, the results of this study are presented in three sections. The first, Section 6.2, compares the resulting modeled fields of vertical wind speed and compound wind speed as simulated by two RAMS runs with and without cloud assimilation.

In section 6.3, the impact of the cloud assimilation on the surface energy and water balance in RAMS is evaluated by comparing model runs with and without cloud assimilation with data obtained from the AZMET observation sites in southern Arizona. Statistical analyses are also made, to evaluate the improvement in the model-calculated incoming short- and long-wave radiation and precipitation when cloud assimilation is applied. As described in Chapter 2, the Chen and Cotton (1983) short-wave radiation scheme was found to exhibit deficiencies and, accordingly, in this research, this scheme was replaced with the improved scheme of Harrington (1997). In general, this

replacement was made for both the short-wave and the long-wave radiation calculations. However, in practice, the RAMS model is capable of running the Chen long-wave radiation scheme even while using the Harrington short-wave radiation scheme. Therefore, to evaluate the relative merit of these two long-wave radiation schemes, the model-derived incoming long-wave radiation fields were compared with observed data for both the Harrington and the Chen and Cotton long-wave radiation schemes.

In the Section 6.4, to investigate the extent to which the above results are sensitive to initial conditions, the results of five, ensemble runs with cloud assimilation are presented. The influence of initiation on near-surface atmospheric variables (i.e. the components of horizontal wind speed, air temperature and humidity) and on the precipitation and downward solar radiation at the surface is investigated.

## **6.2 Impact of Cloud Assimilation on Atmospheric Wind Speed**

Figure 6.1 shows a comparison between two RAMS runs with and without cloud assimilation for cloud water and ice mixing ratio, vertical wind speed and horizontal compound wind speed. In this figure, the first column of figures respectively show the horizontal cross section of cloud water and ice mixing ratio and contours of vertical wind speed and compound wind speed calculated by RAMS when there is no assimilation of satellite observations, while the second column shows the equivalent fields with cloud assimilation. These spatial patterns were those simulated at GMT 20:00 on June 22, 2000 at vertical level 17 (6400 m), which is where RAMS produced a significant amount of cloud in the simulation with cloud assimilation. These figures illustrate an important

practical point. The magnitude of the horizontal and vertical components of wind speed can be critical to a continuous and reliable model simulation because the advection stability criteria used in the model can stop the model simulation if the modeled values exceed specified criteria. However, as shown in Figure 6.1, although the assimilated cloud fields did directly influenced the magnitude and spatial distribution of wind speed, the resulting alteration in the wind fields did not “shock” the model to the extent it failed to meet this criteria in spite of the fact that it assimilated significant cloud at this time. Thus, the RAMS model is able to adapt to the assimilation of cloud images and calculate consistent atmospheric wind velocity fields.

In Figure 6.1, the modeled vertical velocity component is directly related to the location and magnitude of cloud water/ice mixing ratio. For instance, in the column of figures with assimilation, the edges of cloud mass have relatively lower ( $\sim 1.5$  g/kg) cloud amounts than in the cloud mass. In these areas, the modeled vertical wind speed reflects this with  $2\text{--}5$  m s<sup>-1</sup> strong downdrafts. Similarly, the greater cloud-mixing ratio in the inner part of the cloud mass corresponds to a region with modeled updrafts of  $2\text{--}8$  m s<sup>-1</sup>. The updrafts are a sign for developing clouds while the downdrafts indicate cloud development is ceasing. The last two contour plots in both columns in Figure 6.1 show the compound horizontal wind speed for the same model level calculated using zonal and meridional components of wind velocity. In these plot, higher magnitudes occur in location where there is enhanced cloud development. When clouds are assimilated into RAMS, the magnitude of the compound wind speed is doubled (and minimum value remains close to  $5$  m s<sup>-1</sup> but the maximum value reaches to  $15$  m s<sup>-1</sup>, for instance). In

general, as anticipated, when the cloud assimilation results in RAMS generating cloud, both the magnitude and the spatial distribution of the modeled wind fields are noticeably altered compared with the equivalent fields in the run without cloud assimilation.

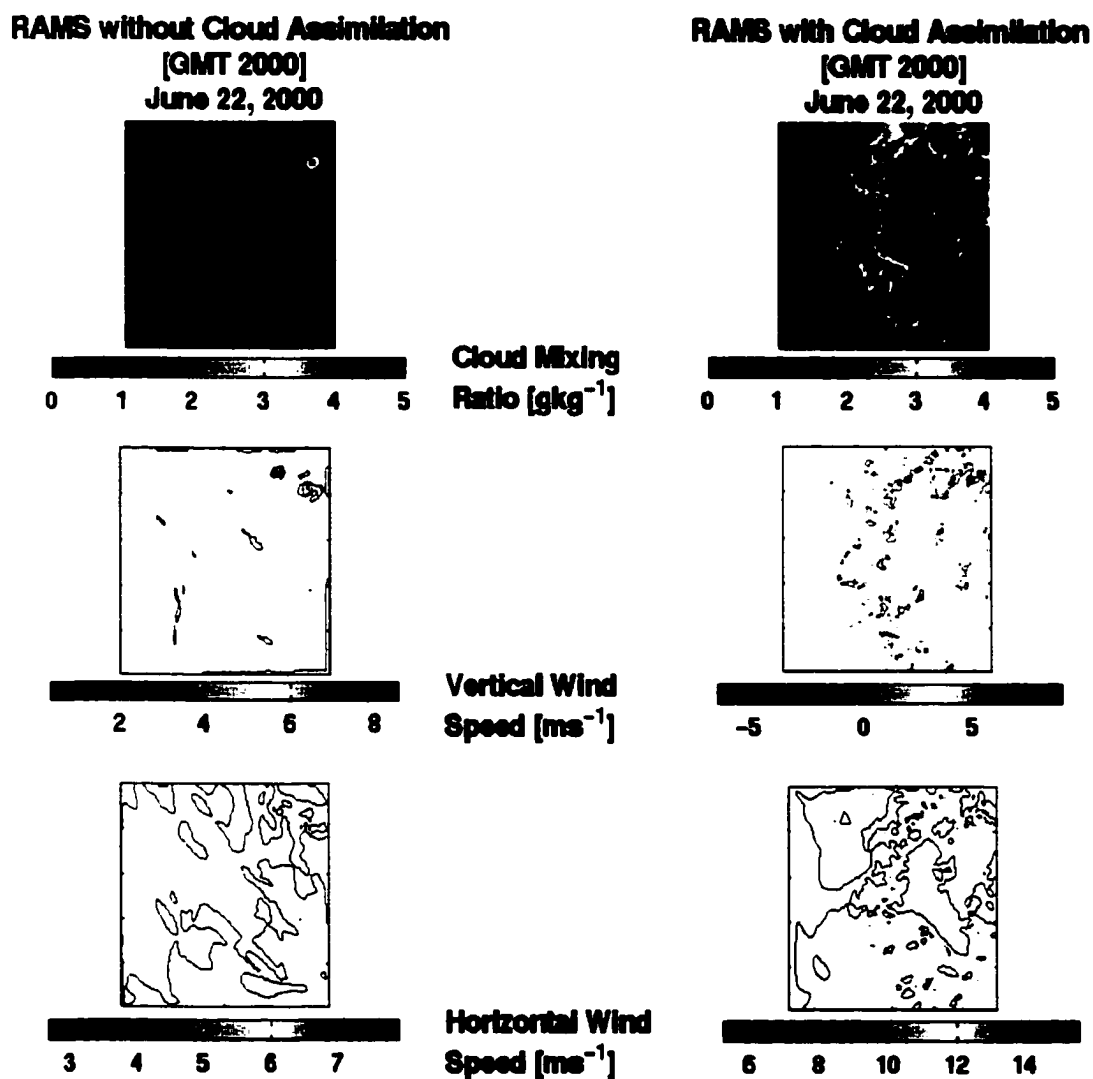


Figure 6.1 Comparison between the fields cloud water/ice mixing ratio, vertical wind speed and compound wind speed calculated by RAMS without cloud assimilation and with cloud assimilation on June 22, 2000 at GMT 20:00 at vertical level 17 in the model.

## **6.3 Impact of Cloud Assimilation on the Surface Energy and Water Balance**

### **6.3.1 Evaluation of Model-Derived Near-Surface Data Relative to Observations**

The model-calculated surface fields, with and without cloud assimilation, were compared against observed data from the AZMET sites during a 3-day period, 14-16 July 1999, and during a 2-day period, 22-23 June 2000. During these periods satellite data showed a worthwhile amount of cloud and they were selected for this reason. The main RAMS-derived surface fields compared with observational data were incoming short-wave and long-wave radiation and precipitation, these being selected because their magnitude is strongly dependent on cloud cover. In addition, downward long-wave radiation fluxes were measured at one site for comparison with model-generated fluxes because this measurement is not available from the AZMET network. These field observations were only available during the second study period, i.e. 22-23 June 2000.

The comparisons between modeled surface data and observed data were made at point scale by selecting the 4-km model grid that most closely corresponds to each measurement site in the AZMET network and the timing appropriately selected to match that of the observations. It is important to remember such point comparisons can include potential error because measured data may poorly sample the model-derived data which are aggregate values over 4 km x 4 km pixel. Although comparisons with observed data at a few points easily reveals possible model error, comparisons with observed data at several different points is required for a credible test of the model's ability to represent different sites and precipitation amounts.

### 6.3.1.1 Incoming Short-wave Radiation

Figure 6.2a and 6.2b show the RAMS-derived surface solar radiation, with and without cloud assimilation, averaged over hourly intervals on July 14-16, 1999 compared with observed values at the AZMET surface meteorology sites in Southern Arizona. Figure 6.3a and 6.3b show equivalent diagrams on June 22-23, 2000. The site number is given in these figures, the actual location of AZMET sites having been given earlier in Figure 3.1.

Certain features are very clear and consistent in these figures. It is apparent that the RAMS model consistently gives rise to substantial overestimates of surface solar radiation at AZMET sites when satellite observations are not assimilated. This is because RAMS systematically underestimates the extent of cloud cover over the array of AZMET sites on these days when warm season daytime convection is taking place. As a result, the modeled atmosphere is too transparent. However, this is substantially altered and improved by cloud assimilation. The modeled solar radiation is greatly improved by assimilating the fractional cloud cover derived from satellite observations over each AZMET site (previously illustrated in Figures 4.4a-b and 4.5a-b for July 14-16, 1999 and for June 22-23, 2000). The modeled atmosphere becomes optically thicker because of the assimilated clouds, and RAMS is able to do a superior job in predicting the surface radiation fields throughout the simulation periods and all the points sampled by observations within the horizontal domain of the model.

Figure 6.2a-b and 6.3a-b both show that RAMS, when aided by cloud assimilation, better simulates convective cloud (with cloud fraction greater than 0.7)

during the monsoon period at these semi-arid sites. The improvement is most obvious at sites 6, 7, 9, 10, 11, 12 and 26 on the first day of the simulation period July 14-16, 1999, and at sites 1, 5, 6, 10, 12, 15, 21, and 26 on the first day during simulation period June 22-23, 2000, when dense cloud is simulated with little error. During these times, both the observed and modeled incoming solar radiation are less than  $100 \text{ W m}^{-2}$ . However, the impact of relatively thin clouds (with cloud fraction less than 0.5) on the surface radiation is sometimes missed with cloud assimilation even though, according to the Figures (4.4a-b and 4.5a-b), these clouds do appear to be provided to RAMS. This feature is apparent at site numbers 23 and 26 during simulation period July 14-16, 1999, and at site numbers 4, 7, 13, 21, 23 during simulation period June 22-23, 2000. This is presumably because the radiation physics in RAMS assumes that atmosphere is mostly transparent for relatively thin and high clouds. This error is most obvious at site 13 during the last day of the June 22-23, 2000 simulation period. At this site, the error mainly contributes to a wrong location of clouds. In general, RAMS with no-assimilation systematically estimates very low values of surface radiation early in the morning over most of the sites. This is probably because the model tends to create an inversion layer (e.g. fog layer) near the surface at these times. However, cloud assimilation improves this by removing this inversion layer. Another important conclusion from Figures 6.2a-b and 6.3a-b is that, although there may be limitations in RAMS ability to simulate cloud, when the sky is clear, the model does provide good calculations of surface radiation.

Figure 6.4 shows scatter plots of modeled and observed hourly-average surface solar radiation for (a) July 14-16, 1999 and (b) June 22-23, 2000, for model simulations

without and with cloud assimilation during periods which were selected as being cloudy on the basis of the satellite observations. Several features already noticed in the time series plots are also apparent in these figures. The RAMS tendency to overestimate surface radiation is reflected in these plots by the presence of points with high modeled and low observed values, while the presence of an early morning near-surface inversion layer in the RAMS run without assimilation show up as points with low modeled and high observed values. The scatter associated with these phenomena is substantially less with assimilation of cloud cover, and this is clear in the figure. A statistical analysis of these data pairs also provides quantitative evidence of the improvement. For example, with assimilation, the correlation coefficient, root mean square error, and bias were respectively improved from 0.66, 355.85  $\text{Wm}^{-2}$  and 194.97  $\text{Wm}^{-2}$  to 0.93, 145.74  $\text{Wm}^{-2}$  and 26.63  $\text{W m}^{-2}$  for the period July 14-16, 1999, and from 0.65, 338.77  $\text{W m}^{-2}$  and 189.73 to 0.89, 180.15  $\text{W m}^{-2}$  and 51.78  $\text{W m}^{-2}$  for the period June 22-23, 2000. Figure 6.4b shows relatively more scatter than Figure 6.4a (the run with data assimilation) because, as mentioned above, thin and higher clouds were more pronounced in this simulation period.

Figure 6.5 illustrates scatter plots equivalent to those in Figure 6.4, but in this case for the daily-average surface solar radiation fields. In this case, the improvement with cloud assimilation is even more enhanced, both visually and statistically. Figure 6.6, on the other hand, shows equivalent scatter plots of hourly surface solar radiation fields only for clear sky conditions. These figures show that, when there is no cloud assimilation, RAMS calculates incoming surface solar radiation accurately but with some uncertainty

(the RSME is 117.76 and 101.33  $\text{Wm}^{-2}$ ) and some bias (the mean bias is 37.18 and 28.61  $\text{Wm}^{-2}$ ). However, even in clear sky condition, in both study periods the runs with cloud assimilation have slightly increased accuracy (reduced RMSE) due, in part, to the removal of the near-surface modeled inversion layer with cloud assimilation. However, for both modeled periods, the bias is increased with cloud assimilation (from 37.18 to 57.76  $\text{Wm}^{-2}$  for July 14-16, 1999, and from 28.61 to 36.53  $\text{Wm}^{-2}$  for June 22-23, 2000) because, in the runs with no assimilation, the scatter, although larger, is more balanced on either side of the one-to-one line. Nonetheless, the general result is that, despite the slightly higher bias, cloud assimilation results in more accurate solar radiation fields even in clear sky conditions.

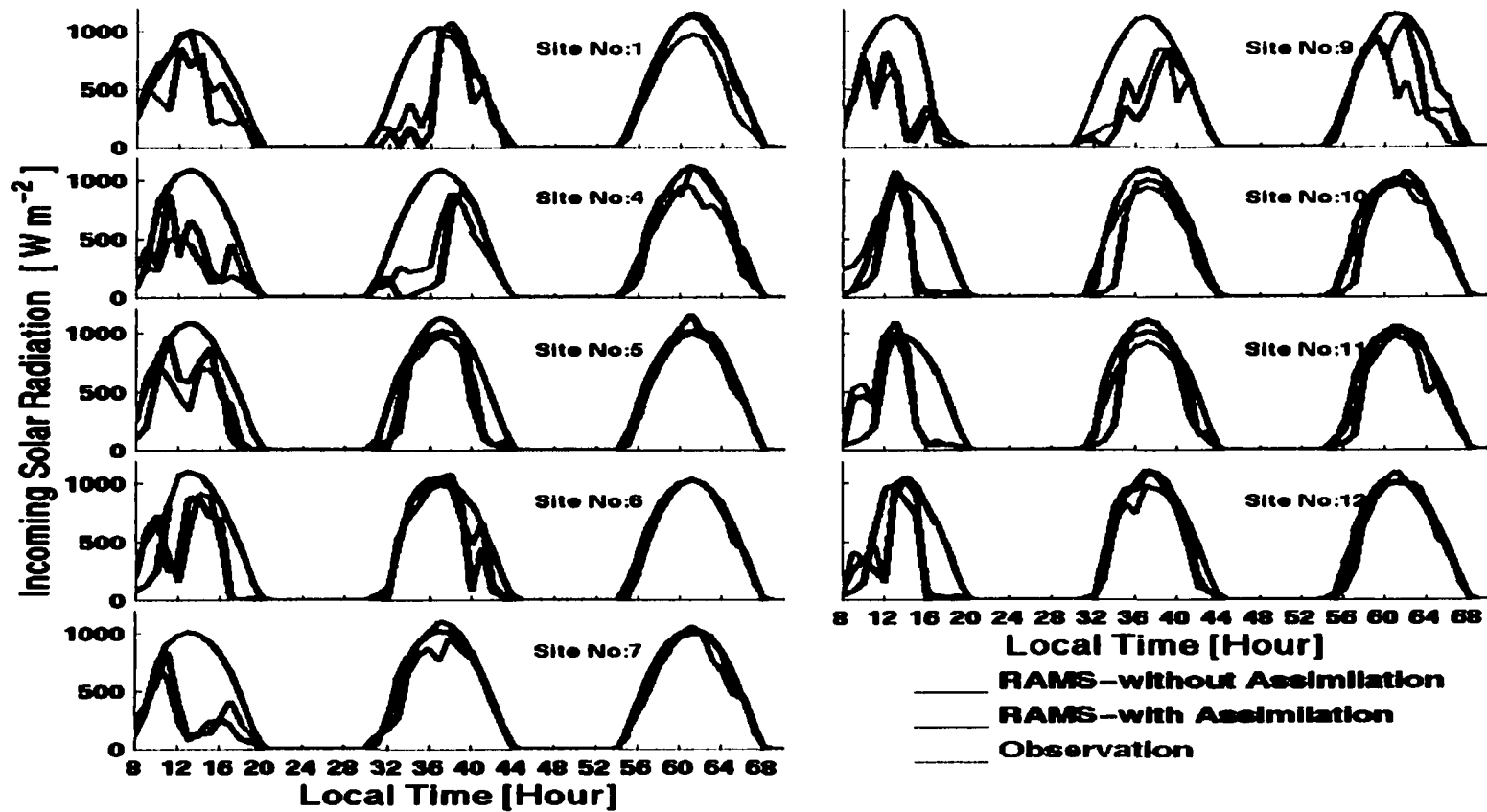


Figure 6.2a RAMS-derived surface solar radiation, with and without cloud assimilation, averaged over hourly intervals on July 14-16, 1999 compared with observed values at the AZMET surface meteorology sites in Southern Arizona.

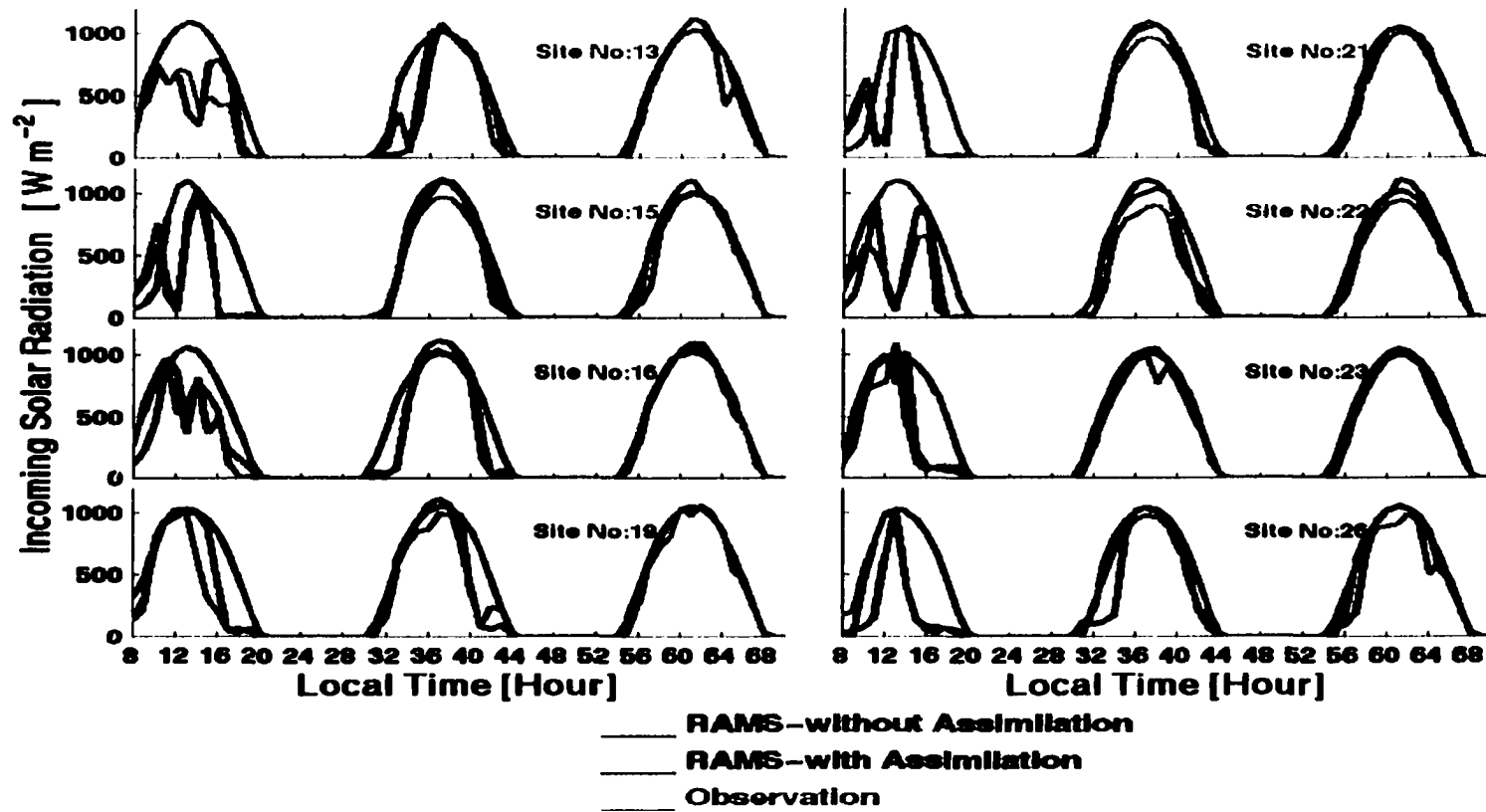


Figure 6.2b RAMS-derived surface solar radiation, with and without cloud assimilation, averaged over hourly intervals on July 14-16, 1999 compared with observed values at the AZMET surface meteorology sites in Southern Arizona.

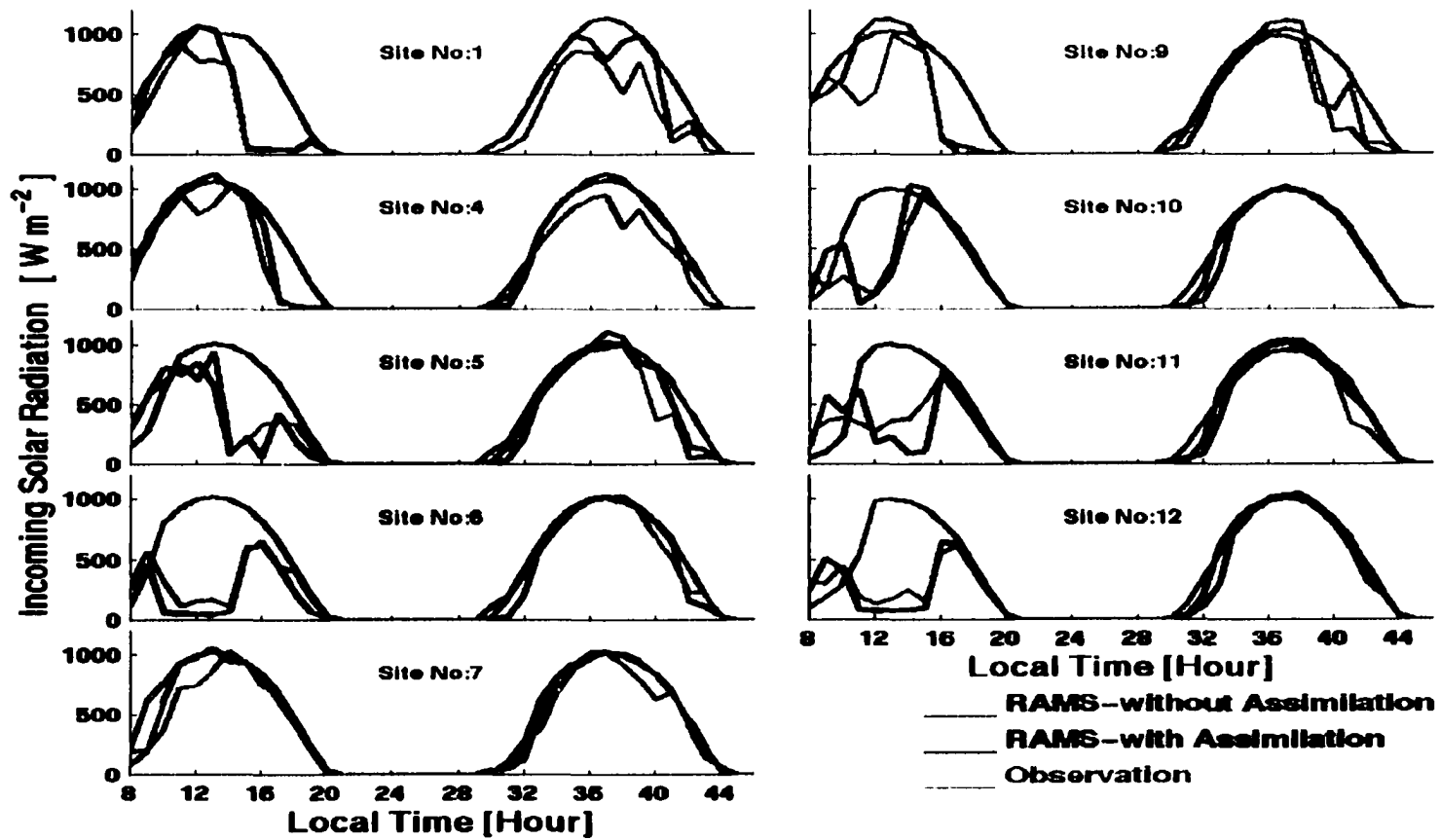


Figure 6.3a RAMS-derived surface solar radiation, with and without cloud assimilation, averaged over hourly intervals on June 22-23, 2000 compared with observed values at the AZMET surface meteorology sites in Southern Arizona.

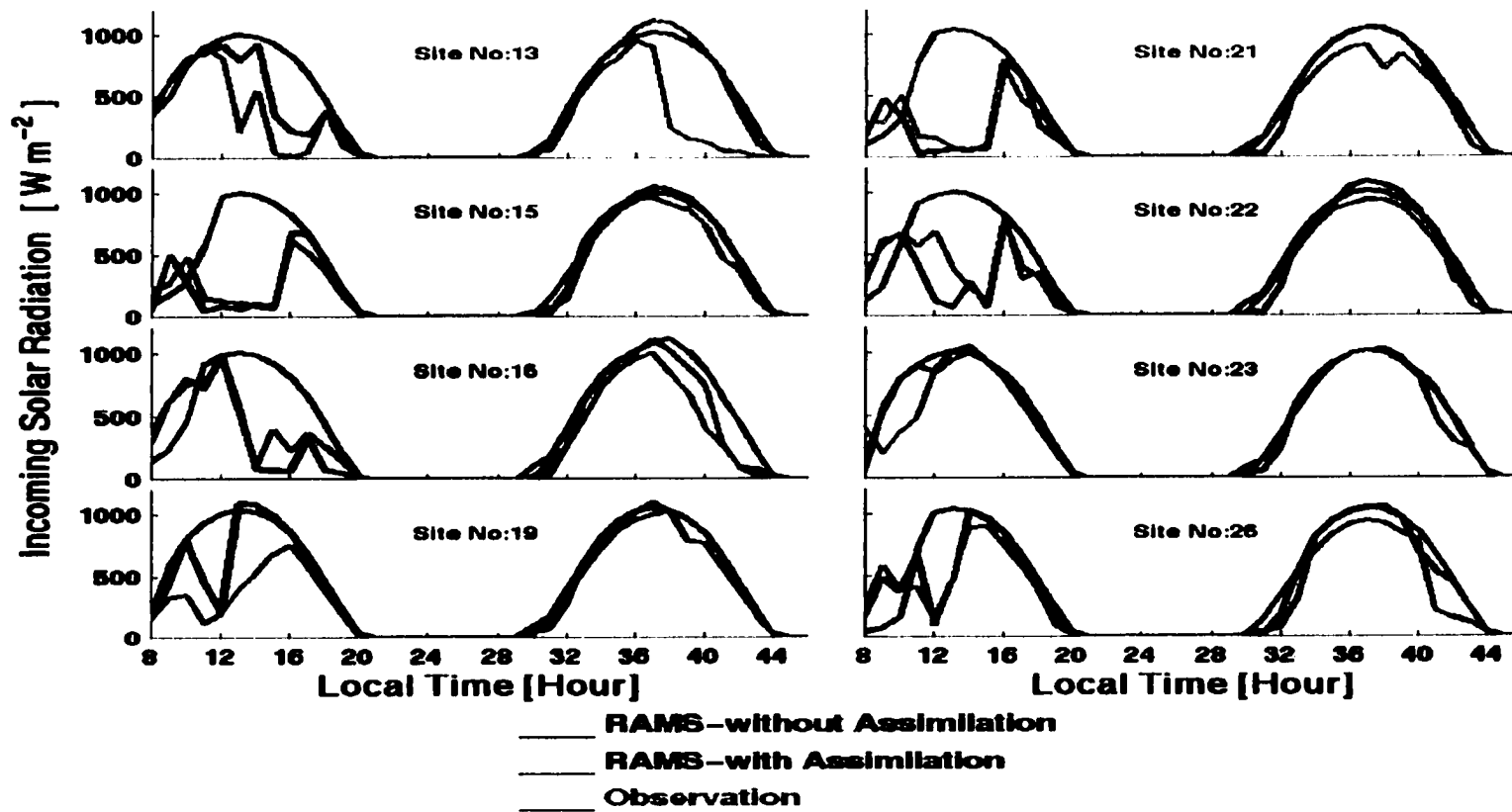


Figure 6.3b RAMS-derived surface solar radiation, with and without cloud assimilation, averaged over hourly intervals on June 22-23, 2000 compared with observed values at the AZMET surface meteorology sites in Southern Arizona.

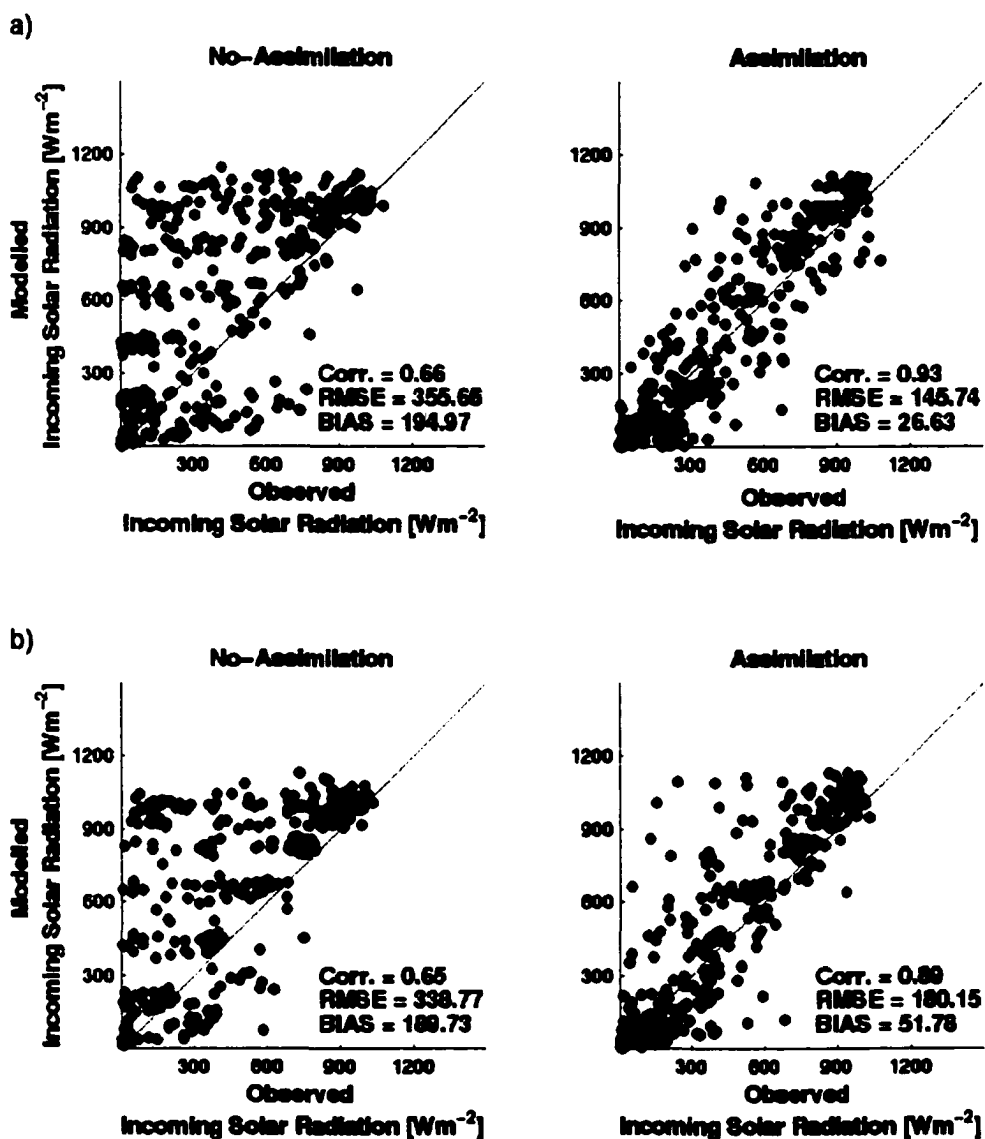


Figure 6.4 Scatter plots of hourly-average modeled and observed surface solar radiation in cloudy sky conditions for (a) July 14-16, 1999 and (b) June 22-23, 2000 and model simulations without and with cloud assimilation.

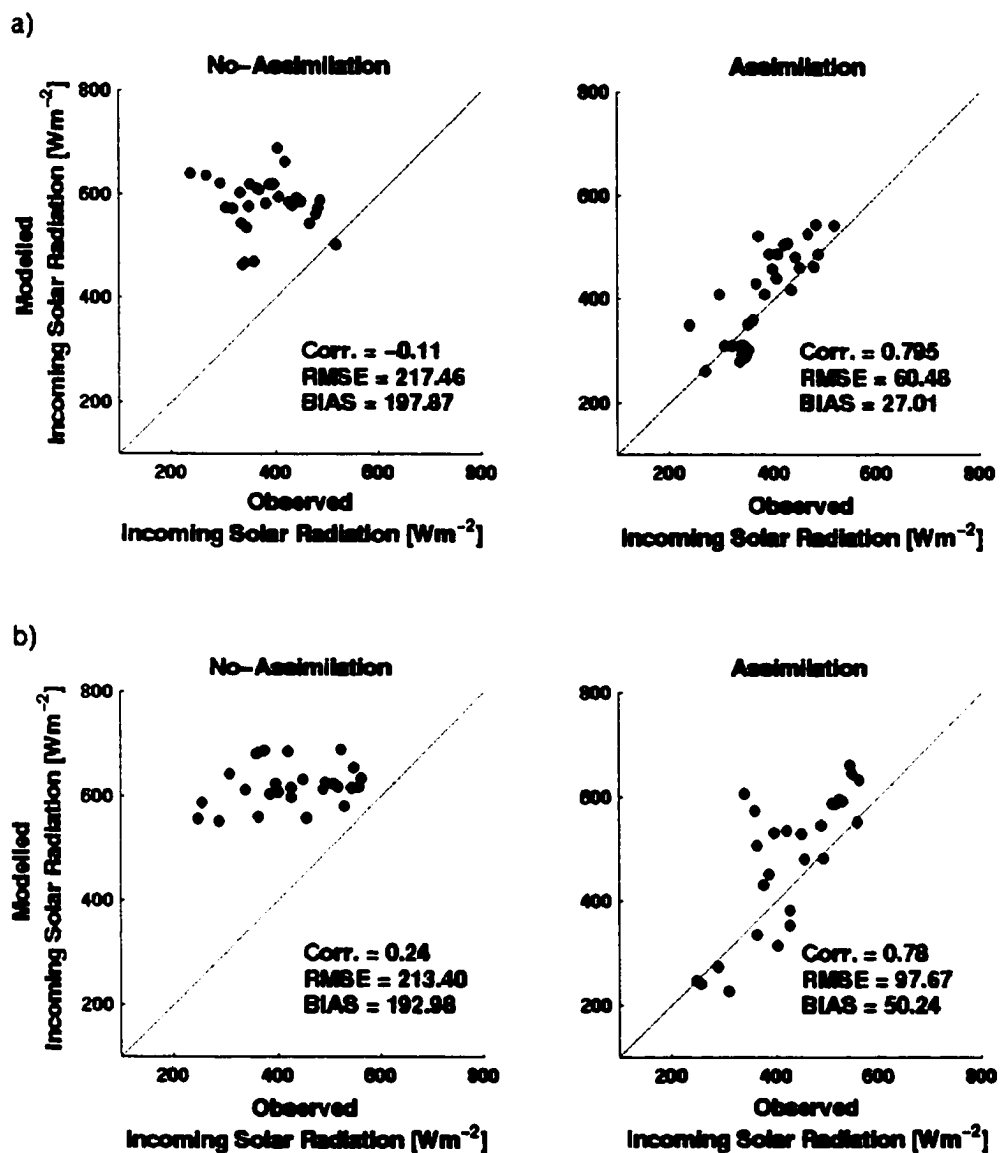


Figure 6.5 Scatter plots of daily-average modeled and observed surface solar radiation in cloudy sky conditions for (a) July 14-16, 1999 and (b) June 22-23, 2000 and model simulations without and with cloud assimilation.

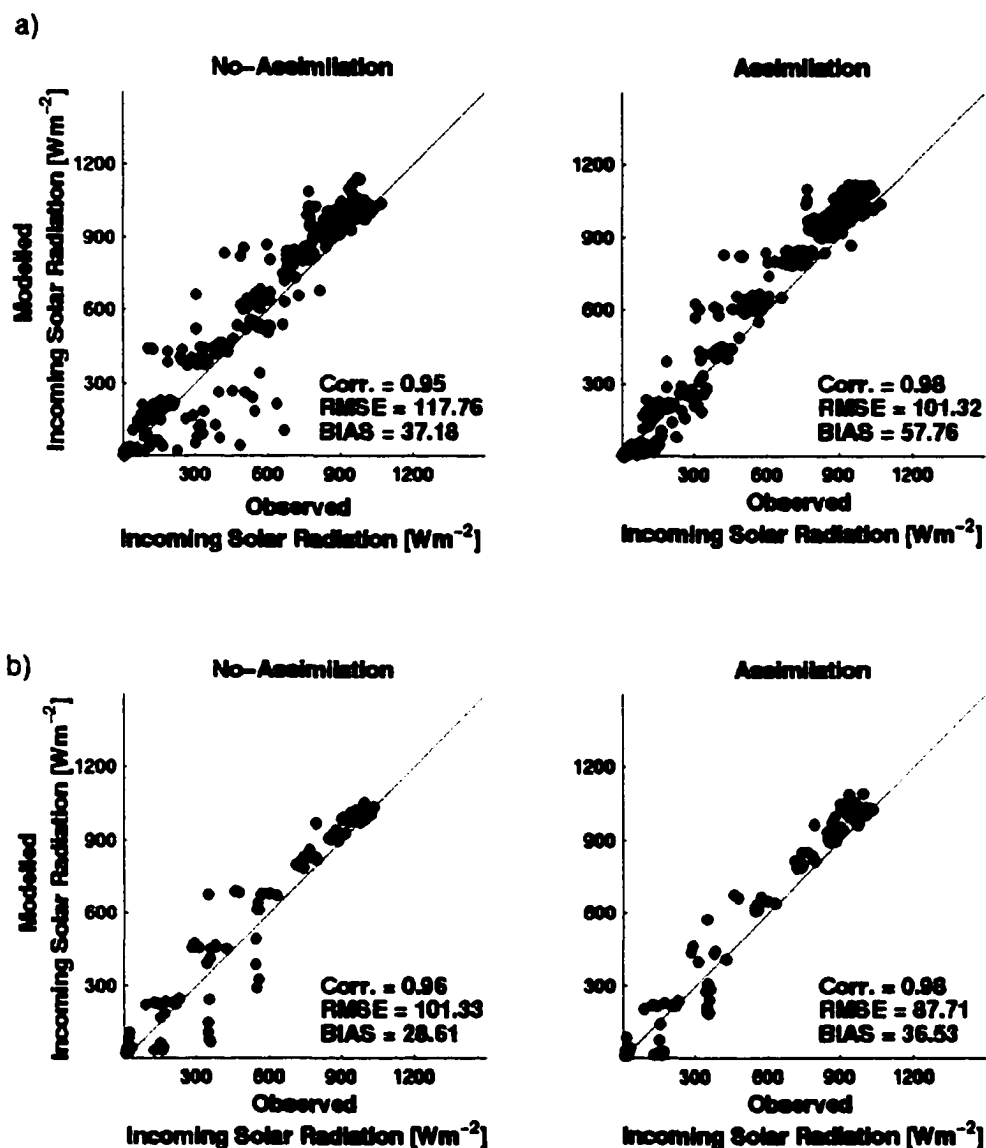


Figure 6.6 Scatter plots of hourly-average modeled and observed surface solar radiation in clear sky conditions for (a) July 14-16, 1999 and (b) June 22-23, 2000 and model simulations without and with cloud assimilation.

### 6.3.1.2 Incoming Long-wave Radiation

Figure 6.7 shows modeled hourly average surface radiation fields, with and without cloud assimilation, compared with observations for (a) incoming short-wave radiation, and (b) incoming long-wave radiation on June 22-23, 2000, using both the Chen/Cotton and the Harrington radiation schemes in the RAMS. In Figure 6.7b the fractional cloud cover derived from satellite observations is also given. The limited availability of the infrared radiometer data means comparisons can only be made for one point in the modeled domain. However, comparison at this one measurement point does provide important evidence for the improvement in the simulation of incoming long-wave radiation flux with cloud assimilation. With the Chen/Cotton long-wave radiation scheme, RAMS-simulated incoming long-wave radiation responds to the variation in cloud cover appropriately when satellite observations are assimilated. Increased cloud cover gives increased downward long-wave radiation flux, as expected. However, the same variation is not true in the case of the Harrington long-wave scheme. Using the Harrington scheme, the long-wave flux only shows the expected variation when relatively thick clouds are assimilated into the model, as shown in Figure 6.7b at the local times 15 hours and 42 hours.

Careful inspection of the long-wave radiation time series shows that the amount of fractional cloud cover at local times 33 hours and 37 hours was around 0.2, and corresponding long-wave flux with the Chen scheme at these times were 325 and 400  $W m^{-2}$ , respectively. This implies that at local time 37 hours, relatively thicker cumulus cloud is captured in the atmospheric column even though the fractional cloud cover is only of

0.2. This is consistent with the results for incoming short-wave radiation derived with both radiation schemes at this particular local time shown in Figure 6.7a. Another important result that is true for both of the long-wave schemes, is that cloud assimilation also tends to improve nighttime values of incoming long-wave radiation relative to the values of those derived from RAMS with no-assimilation, despite the fact that the cloud images are only available during the day. When there is no cloud assimilation, the Harrington scheme gave more cooling during the night than the Chen/Cotton scheme, and reached a minimum value of  $250 \text{ W m}^{-2}$ , i.e. less than for Chen scheme which stayed near  $300 \text{ W m}^{-2}$  during the night. This may partly contribute towards the generally poor representation of long-wave fluxes obtained with the Harrington scheme and cloud assimilation. The domain average vertical temperature profile shown in Figure 6.8 also indicates there is more cooling during the night at lower model levels when the Harrington radiation scheme is used. For instance, the difference between air temperature using the Chen and the Harrington schemes at the first model level is about  $3.5 \text{ }^\circ\text{K}$ . The domain averaged vertical temperature profiles shown in Figure 6.8 were calculated using only the nighttime temperature values when there is no-cloud assimilation.

Figure 6.9 shows scatter plots between the observed, daytime values of hourly average incoming long-wave radiation and modeled values with and without assimilation for (a) the Chen/Cotton scheme, and (b) the Harrington scheme on June 22-23, 2000. It is clear that cloud assimilation shifts long-wave radiation values towards higher values and closer to observation, and that this is more evident in the case of the Chen/Cotton radiation scheme (Figure 6.9a). The improvement is also demonstrated by statistical

analysis. For example, cloud assimilation improved the RMSE and bias from  $71.54 \text{ Wm}^{-2}$  and  $-69.80 \text{ Wm}^{-2}$  to  $38.62 \text{ Wm}^{-2}$  and  $-26.84 \text{ Wm}^{-2}$ , respectively, for the Chen scheme, and improved the RMSE and bias from  $73.42 \text{ Wm}^{-2}$  and  $-71.76 \text{ Wm}^{-2}$  to  $59.57 \text{ Wm}^{-2}$  and  $-50.72 \text{ Wm}^{-2}$ , respectively, for the Harrington scheme. These statistics confirm that the Chen/Cotton long-wave radiation scheme in general is preferable to the Harrington scheme in this application.

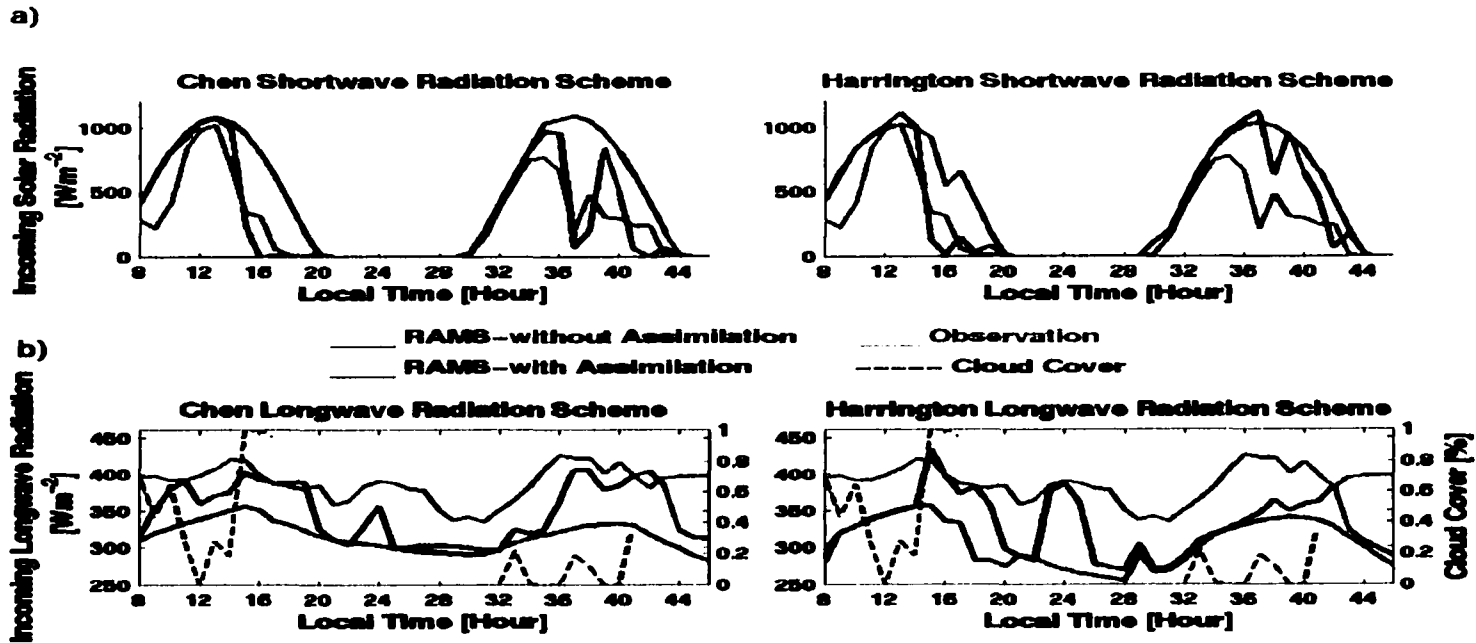


Figure 6.7 Comparison between observed surface radiation fields and RAMS-derived values, with and without cloud assimilation, for (a) incoming short-wave radiation, and (b) incoming long-wave radiation on June 22-23, 2000 using the Chen/Cotton and the Harrington radiation schemes. In (b), the satellite-derived fractional cloud cover is also plotted.

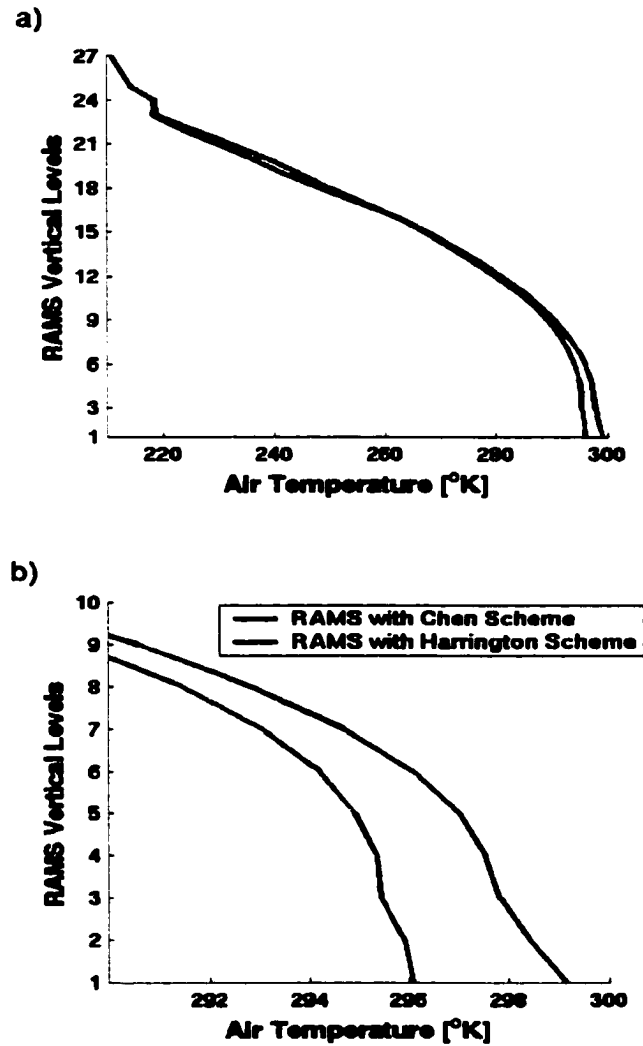


Figure 6.8 Domain-average vertical temperature profiles during the night as modeled by RAMS with the Chen/Cotton and the Harrington schemes for (a) all levels and for (b) the lower model levels.

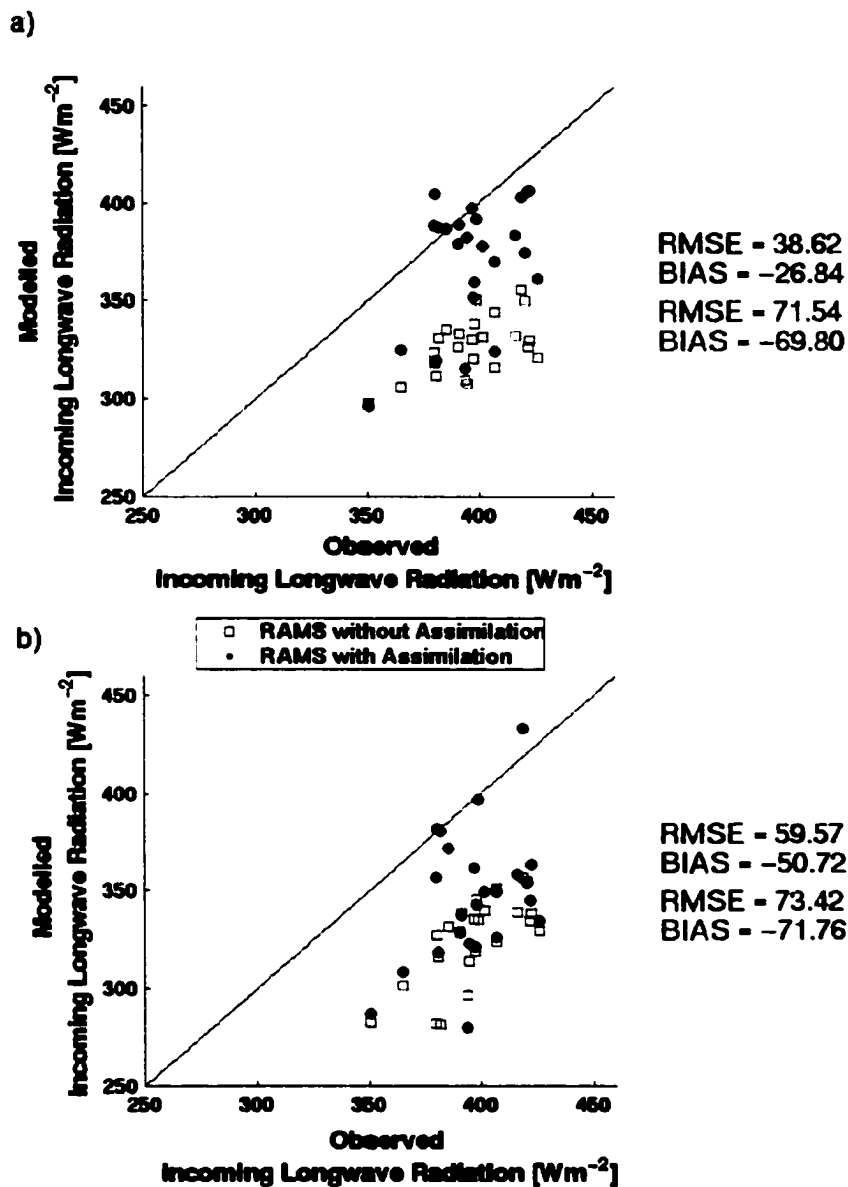


Figure 6.9 Scatter plots between the observed values and modeled values, with and without assimilation, of hourly averaged incoming long-wave radiation during the day for (a) the Chen/Cotton scheme and for (b) the Harrington scheme on June 22-23, 2000.

### 6.3.1.3 Precipitation

Figure 6.10a-b show a comparison between the observed precipitation and that calculated by RAMS with and without cloud assimilation on July 14-16, 1999 at the AZMET sites in Southern Arizona. Figure 6.11a-b show equivalent diagrams on June 22-23, 2000.

It is apparent that the microphysics used in the RAMS model consistently underestimates and/or rarely estimates surface total precipitation at each of the AZMET sites when no satellite observations of cloud are assimilated. This may in part be due to RAMS using inaccurate model re-initialization fields and domain boundary forcing and, more importantly, a modeled atmospheric boundary layer in which latent heat flux is easily curtailed by soil moisture stress and sensible heat becoming the dominant energy flux over the semi-arid landscape.

However, this feature is substantially altered and improved by cloud assimilation. After applying cloud assimilation, RAMS tends to overestimate precipitation relative to observations at the AZMET sites because precipitation is highly sensitive to the concentration of microphysical variables and these are updated every minute by satellite observations. Nonetheless, with cloud assimilation, RAMS generally estimates precipitation reasonably well when compared to the point measurement of precipitation at the AZMET sites on July 14-16, 1999. The simulated storms are approximately in the right place and at the right time because the cloud cover is more realistic. Conversely, RAMS was not able to capture the precipitation (~20 mm) observed at sites 7 and 11 during the night, 12 hours after the last cloud assimilation.

RAMS exhibited a greater tendency toward overestimating surface precipitation compared to the observations during the second study period, June 22-23, 2000. For instance, at sites 5, 6, 10, 12, 15, and 21, the model generated large amounts of precipitation while observations recorded little if any precipitation at these sites. However, the observed incoming solar radiation (Figures 6.3a-b) showed that very thick convective clouds were observed at this time at these sites. The model therefore has reason to calculate precipitation and, since the observations are point measurements, it is possible that the measurements missed some precipitation from the convective system. It would be more reliable to compare the modeled precipitation compared with observations from a number of stations in each (4 km x 4km) modeled grid square.

The observed daily precipitation amount at each AZMET site are compared with the estimates given by model simulations with and without cloud assimilation in Table 6.1 for July 14-16, 1999 and in Table 6.2 for June 22-23, 2000. The observed and modeled values (with assimilation) precipitation given in these Tables were also plotted against each other in Figure 6.12a for July 14-16, 1999 and in Figure 6.12b for June 22-23, 2000. The overestimation of modeled precipitation with cloud assimilation already observed in the time series plots for June 22-23, 2000 are again revealed clearly in Figure 6.12b for both the daily precipitation and site average precipitation plots. The scatter in daily precipitation plots in Figure 6.12a is reduced when the domain average is taken (Figure 6.12a.) The correlation coefficient improves from 0.42 to 0.84. Clearly, averaging over the sites smoothes the data. Temporal variations of the observed hourly precipitation is compared with modeled values with and without assimilation as a domain average in

Figure 6.13a for July 14-16, 1999 and in Figure 6.13b for June 22-23, 2000. The comparison given in Figure 6.13a shows excellent agreement between the modeled values with assimilation and the observed precipitation during the simulation period. In Figure 6.13b, there is a substantial discrepancy in magnitude between modeled and observed precipitation, but at least some precipitation is observed during this period--not the case without assimilation—and the timing is broadly correct with cloud assimilation.

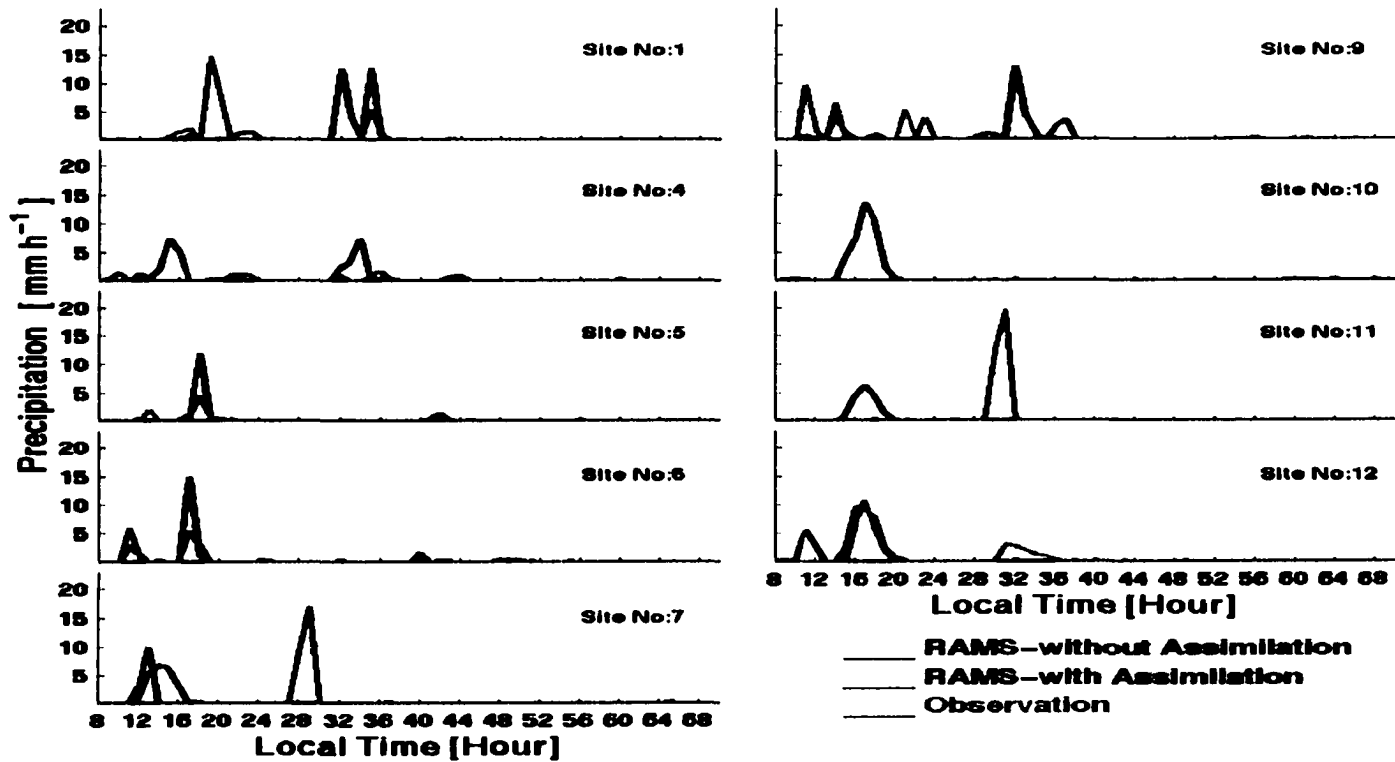


Figure 6.10a Comparison between observed precipitation and that calculated by RAMS with and without cloud assimilation or hourly intervals on July 14-16, 1999 at the AZMET sites in Southern Arizona.

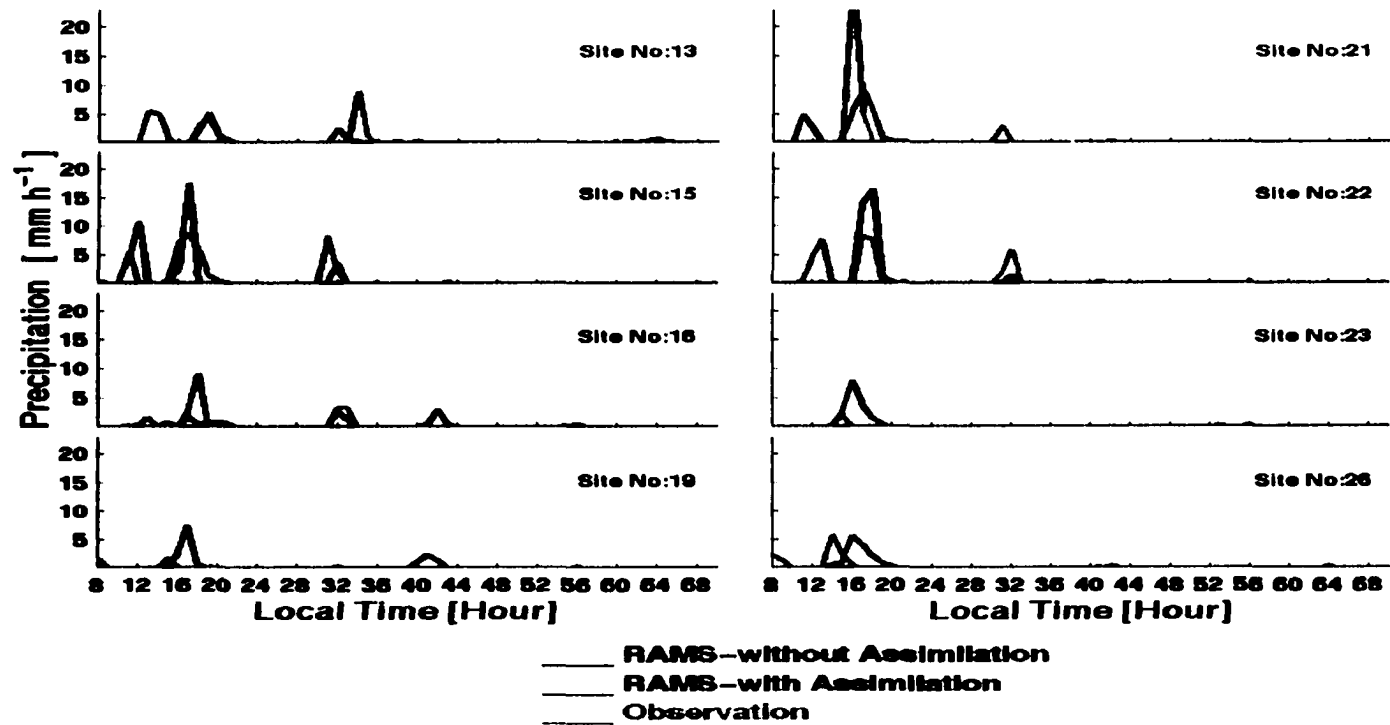


Figure 6.10b Comparison between observed precipitation and that calculated by RAMS with and without cloud assimilation for hourly intervals on July 14-16, 1999 at the AZMET sites in Southern Arizona.

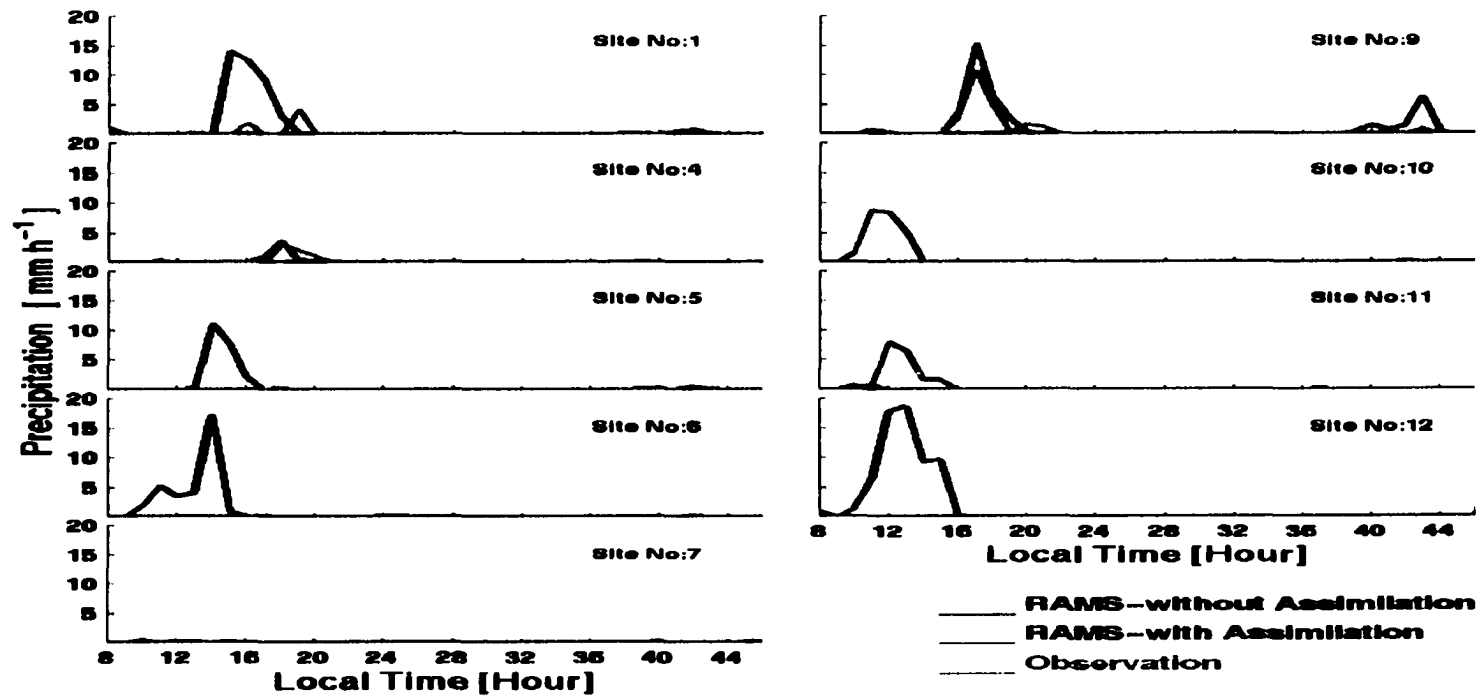


Figure 6.11a Comparison observed precipitation and that calculated by RAMS with and without cloud assimilation hourly intervals on June 22-23, 2000 at the AZMET sites in Southern Arizona.

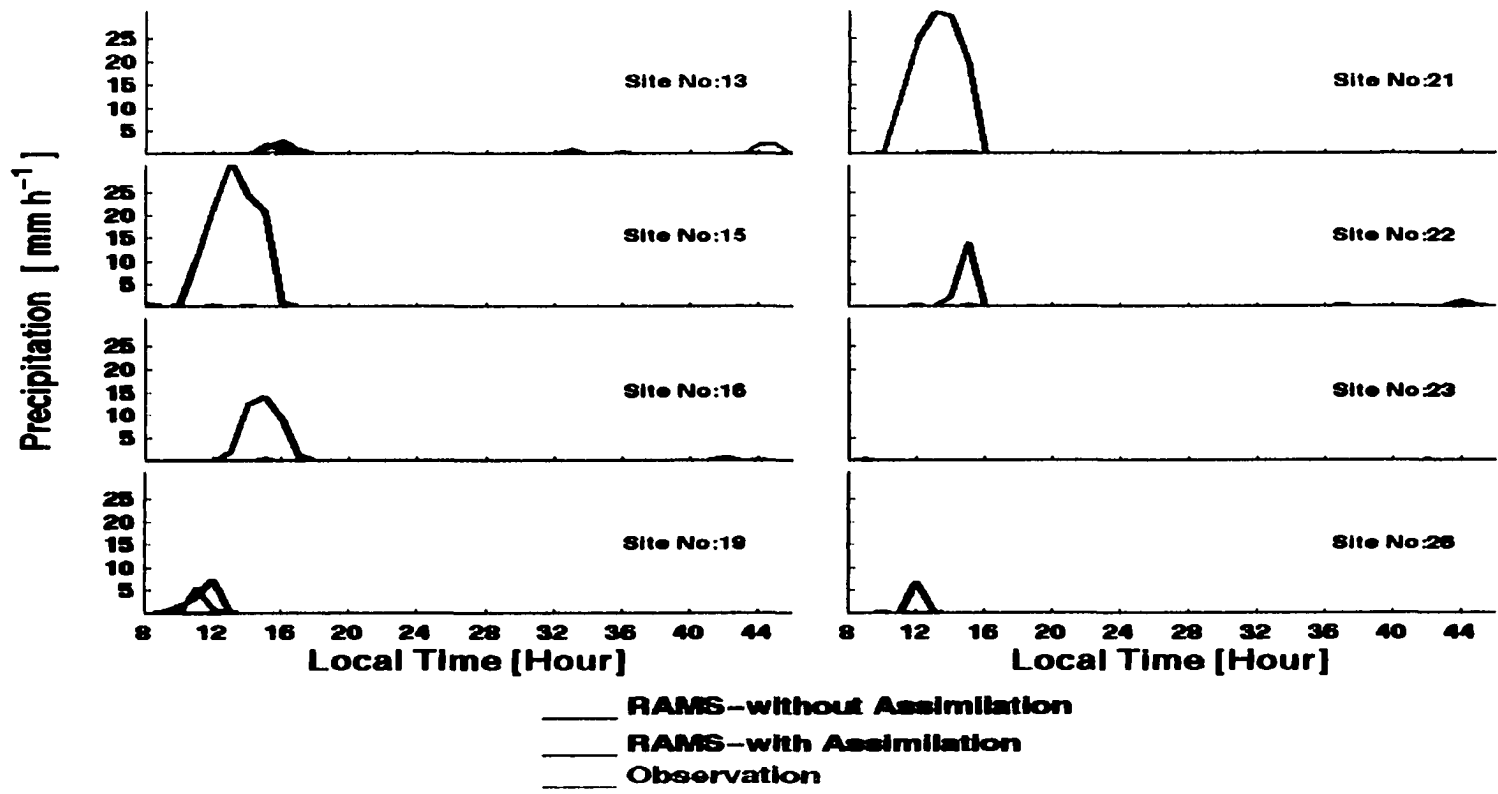


Figure 6.11b Comparison between observed precipitation and that calculated by RAMS with and without cloud assimilation for hourly intervals on June 22-23, 2000 at the AZMET sites in Southern Arizona.

Observed Precipitation	Modeled Precipitation		Days of the Events	AZMET Sites (#)
	Assimilation	No-Assimilation		
26.66 12.95 0	4.9 23.9 0	0.2 0.1 0	July 14, 99 July 15, 99 July 16, 99	1
3 2 0	18.7 17.9 0.1	0 0 0	July 14, 99 July 15, 99 July 16, 99	4
15 0 0	7.5 2.1 0.1	0 0 0	July 14, 99 July 15, 99 July 16, 99	5
23 0 0	13.3 2.5 1	0 0 0	July 14, 99 July 15, 99 July 16, 99	6
13 22 0	22.2 0.1 0.1	0 0 0	July 14, 99 July 15, 99 July 16, 99	7
27.66 1 0	8.4 26.5 1.6	0 0 0	July 14, 99 July 15, 99 July 16, 99	9
0 0.5 1.25	38.1 0.2 0.1	0 0 0	July 14, 99 July 15, 99 July 16, 99	10
0.51 31.75 0	17.6 0.3 0	0 0 0	July 14, 99 July 15, 99 July 16, 99	11
24.13 11.67 0.25	40.5 0.2 0	0.2 0 0	July 14, 99 July 15, 99 July 16, 99	12
8 10 0	20.2 3.2 1.7	0 0 0	July 14, 99 July 15, 99 July 16, 99	13
25.4 10.41 0	39.1 3.6 0	0.4 0 0	July 14, 99 July 15, 99 July 16, 99	15
12.44 6.6 0	6.6 7.5 0.5	0.1 0 0	July 14, 99 July 15, 99 July 16, 99	16
1.78 0 0	10.7 4.6 0.1	0 0 0	July 14, 99 July 15, 99 July 16, 99	19
33.02 3.3 0	28.6 0.1 0	0 0 0	July 14, 99 July 15, 99 July 16, 99	21
17.02 7.61 0	44.4 1.4 0.2	0 0 0	July 14, 99 July 15, 99 July 16, 99	22
1.78 0 0	16.1 0 0.2	0 0 0	July 14, 99 July 15, 99 July 16, 99	23
8.64 0 0	15.6 0.4 0	0 0 0	July 14, 99 July 15, 99 July 16, 99	26

Table 6.1 RAMS-simulated, with and without cloud assimilation and measured daily precipitation at AZMET sites for July 14-16, 1999.

Observed Precipitation	Modeled Precipitation		Days of the Events	AZMET Sites (#)
	Assimilation	No-Assimilation		
8.89 0.5	38.1 2.2	0 0	June 22, 2000 June 23, 2000	1
6 0	5.3 0.1	0 0	June 22, 2000 June 23, 2000	4
0 0	20.7 0.8	0 0	June 22, 2000 June 23, 2000	5
0 0	33 3.6	0 0	June 22, 2000 June 23, 2000	6
0.51 0.5	0.4 0.1	0 0	June 22, 2000 June 23, 2000	7
20.82 0.76	28.8 10.1	0.4 0	June 22, 2000 June 23, 2000	9
0 0	23.7 0.1	0 0	June 22, 2000 June 23, 2000	10
0.76 0	18.4 0.1	0 0	June 22, 2000 June 23, 2000	11
0.25 13.96	63.6 0	0.7 0	June 22, 2000 June 23, 2000	12
4 5	4.7 0.6	0 0	June 22, 2000 June 23, 2000	13
0.50 0	110.2 0.1	0.9 0	June 22, 2000 June 23, 2000	15
0.52 0.25	38.8 1	0 0	June 22, 2000 June 23, 2000	16
6.61 0	13 0.2	0 0	June 22, 2000 June 23, 2000	19
1.1 0	116 0.3	0 0	June 22, 2000 June 23, 2000	21
0.51 1.77	16.4 0.3	0 0	June 22, 2000 June 23, 2000	22
0.51 0	0.3 0.4	0 0	June 22, 2000 June 23, 2000	23
6.35 0	7.7 0.1	0 0	June 22, 2000 June 23, 2000	26

Table 6.2 RAMS-simulated, with and without cloud assimilation and measured daily precipitation at AZMET sites for June 22-23, 2000.

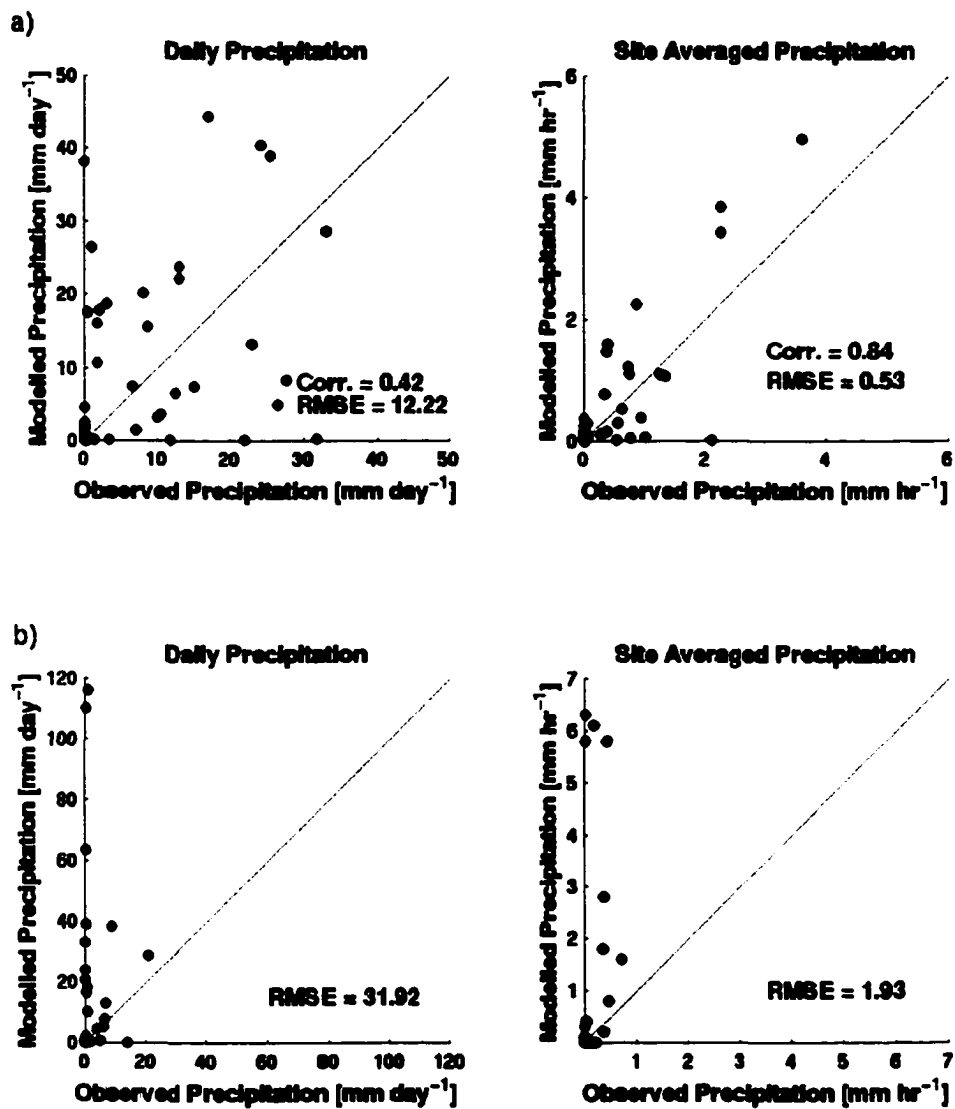


Figure 6.12 Scatter plots between observed and modeled (with assimilation) daily total, site-average precipitation for (a) July 14-16, 1999 and for (b) June 22-23, 2000.

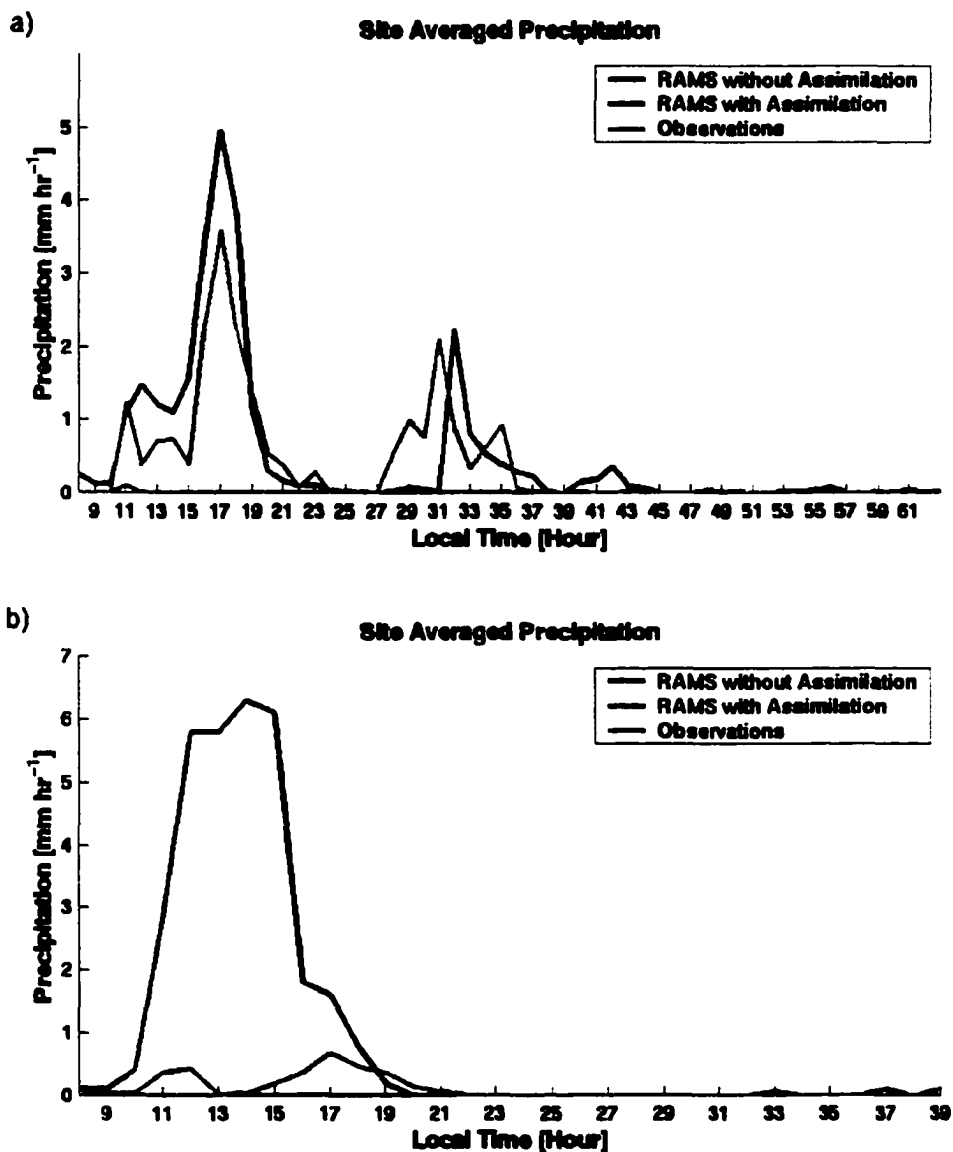


Figure 6.13 Time series of observed and hourly average modeled (with and without assimilation) precipitation averaged over all AZMET sites in model domain for (a) July 14-16, 1999 and for (b) June 22-23, 2000.

## 6.4 Ensemble Runs

Because the atmosphere is a chaotic dynamical system, small errors in the initial conditions can lead to growing errors in model simulations, eventually leading to a total loss of any predictive information. To estimate the possible size of such errors, models should be run from several different initial (perturbed) conditions. In this study, initial perturbations were created by initiating RAMS from the surface-analysis, and from the 3-hour, 6-hour, 9-hour, and 12-hour forecasts of the Rapid Update Cycle (RUC) model. By performing runs with these different initiations we were able to investigate how sensitive the results were to initial conditions.

Figure 6.14 (a, b, c) shows perturbations created using the RUC surface-analysis and 3-hr, 6-hr, 9-hr, 12-hr RUC forecasts and Eta surface-analysis for (a) air temperature, (b) relative humidity, and (c) wind speed, respectively, at the initial time of 00:00 GMT on July 14, 1999 (i.e. local time 17:00 PM on July 13, 1999). These fields are interpolated from RUC and Eta domains (the RUC and Eta models both have 40-km horizontal resolution) to RAMS domain at the lowest model level. For simplicity of interpretation, the compound wind speed in Figure 6.14c is given rather than the zonal and meridional wind speeds, which were those actually used for initiation. These figures illustrate that it was indeed feasible to initiate the RAMS model simulations using slightly different initiations.

The results of these five ensemble runs are displayed in Figures 6.15a, b, c, d, and e in the form of domain-average air temperature, water vapor mixing ratio, compound wind speed, accumulated precipitation, and incoming solar radiation at lowest model-

level, respectively, for the model simulation period July 14-16, 1999. In these figures, the daytime period during which cloud assimilation occurred is separated from the nighttime periods that are purely model simulation. In practice, there is little difference in the modeled behavior between daytime (with assimilation) and nighttime (without assimilation) periods. The difference between initial values is clear, but all the runs tend to converge within a few hours of initiation when there is no cloud cover assimilation. 14 hours after initiation, at local time 7, the ensemble of runs converges rapidly. The general result of this ensemble runs is that RAMS, when run with and without cloud cover assimilation, shows little sensitivity to the initial conditions, and this increases the credibility and generality of the results given in previous sections.

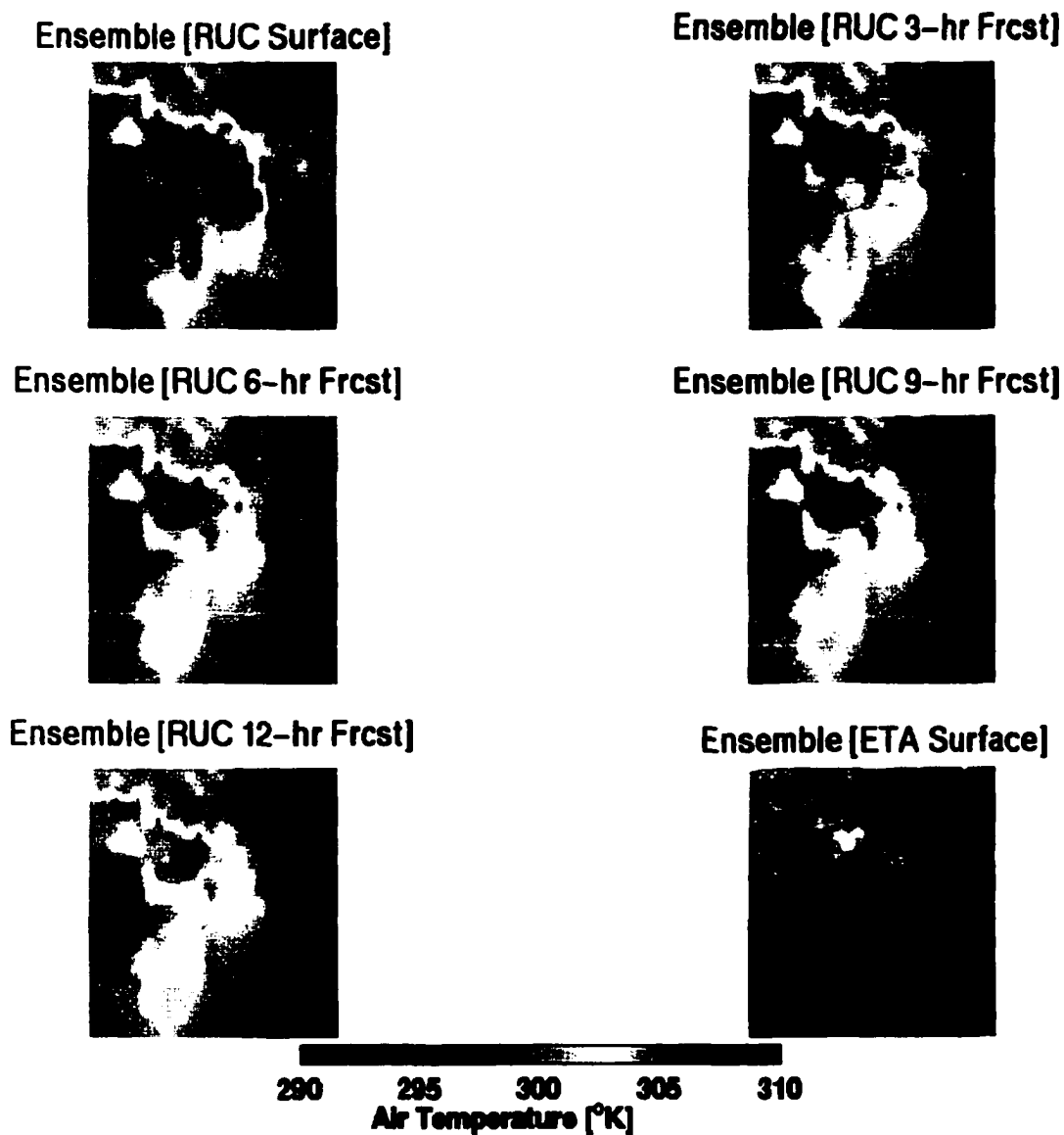


Figure 6.14a Shows initial perturbations created from RUC surface-analysis and RUC 3-hr, 6-hr, 9-hr, and 12-hr forecasts and Eta surface-analysis for air temperature at the lowest model level on July 14, 1999 at GMT 00:00.

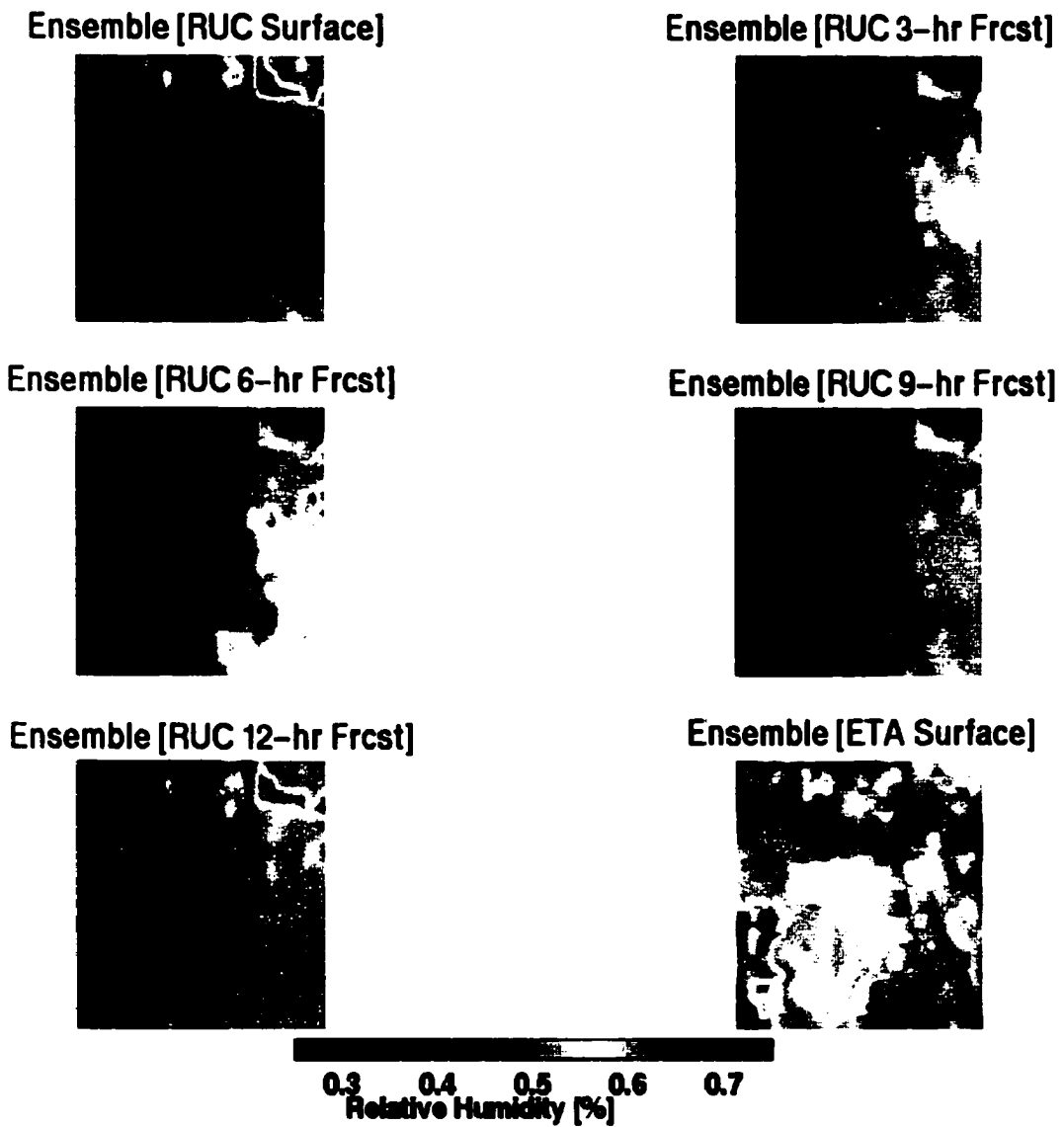


Figure 6.14b Shows initial perturbations created from RUC surface-analysis and RUC 3-hr, 6-hr, 9-hr, and 12-hr forecasts and Eta surface-analysis for relative humidity at the lowest model level on July 14, 1999 at GMT 00:00.

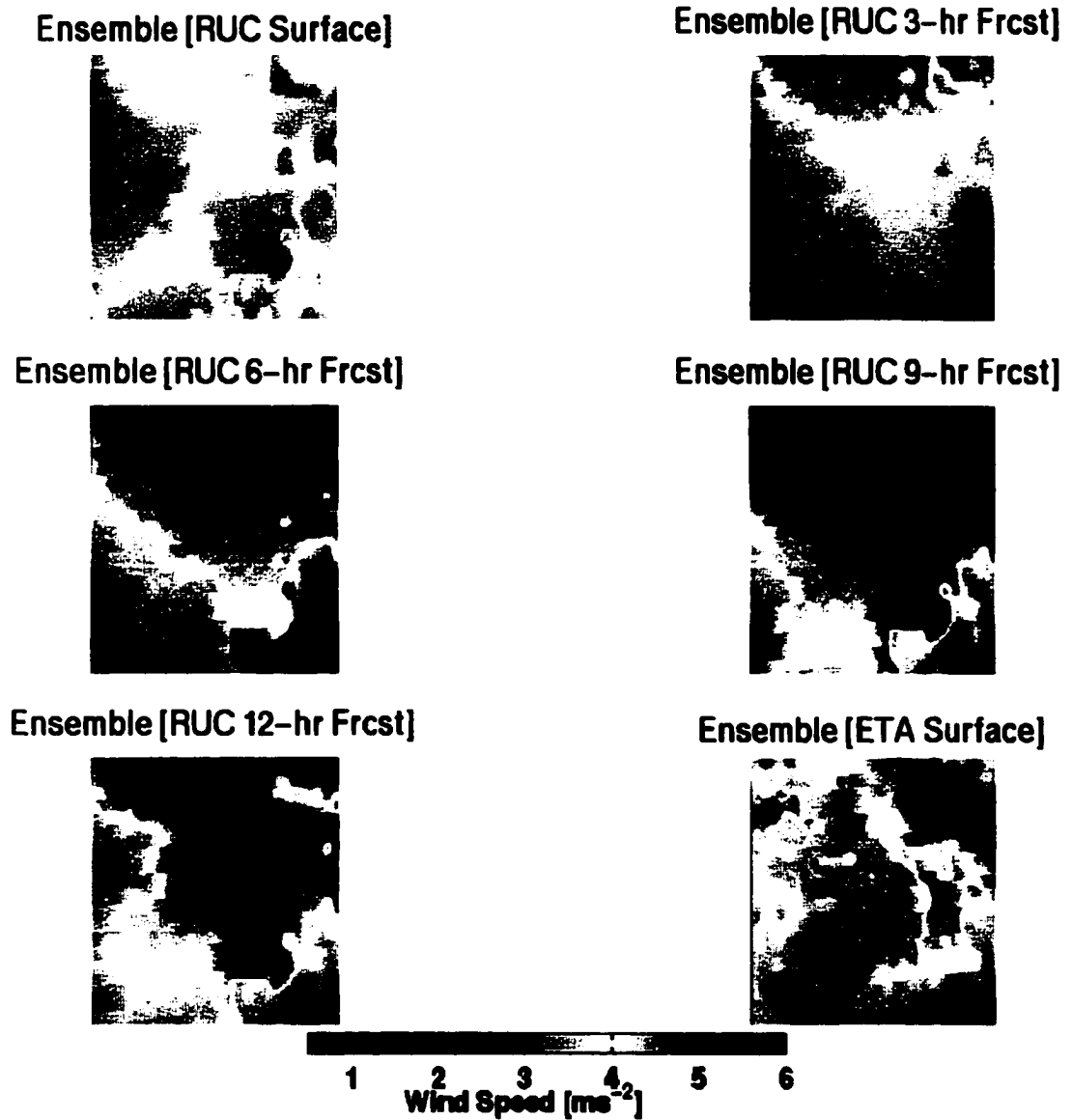


Figure 6.14c Shows initial perturbations created from RUC surface-analysis and RUC 3-hr, 6-hr, 9-hr, and 12-hr forecasts and Eta surface-analysis for compound wind speed at the lowest model level on July 14, 1999 at GMT 00:00.

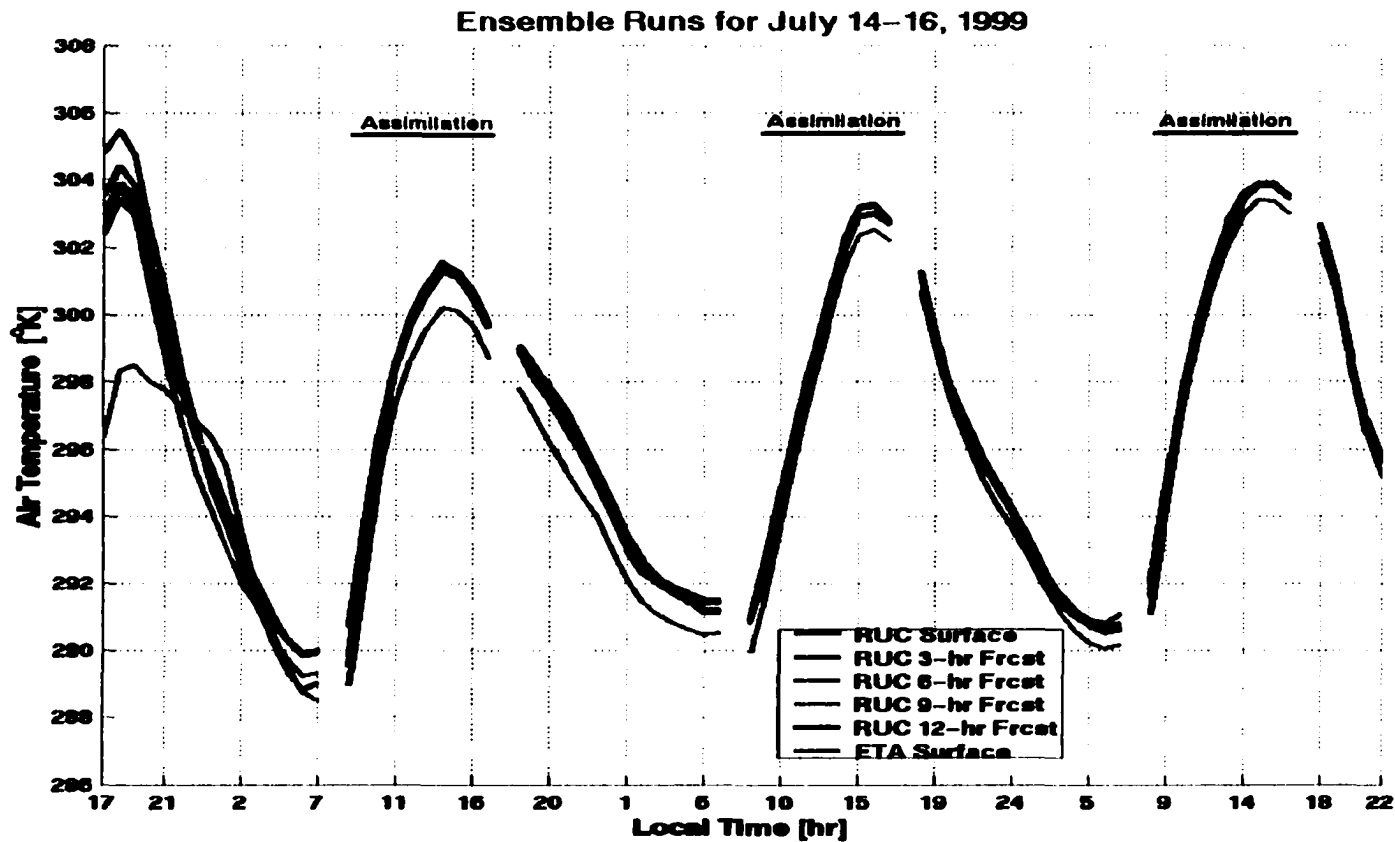


Figure 6.15a Results of domain average lowest model-level air temperature from five ensemble runs with RAMS coupled with cloud assimilation on July 14-16, 1999.

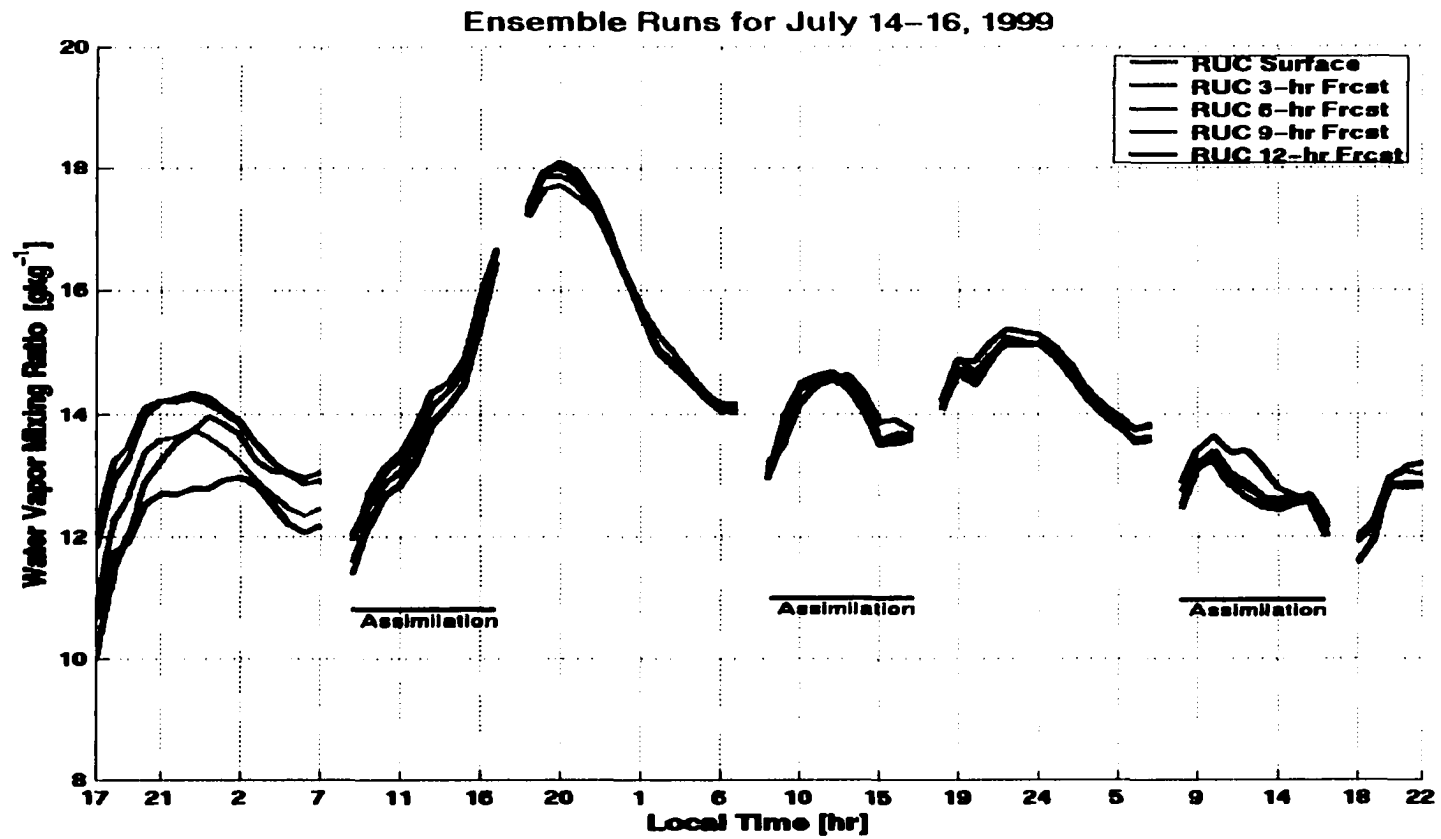


Figure 6.15b Results of domain average lowest model-level water vapor mixing ratio from five ensemble runs with RAMS coupled with cloud assimilation on July 14-16, 1999.

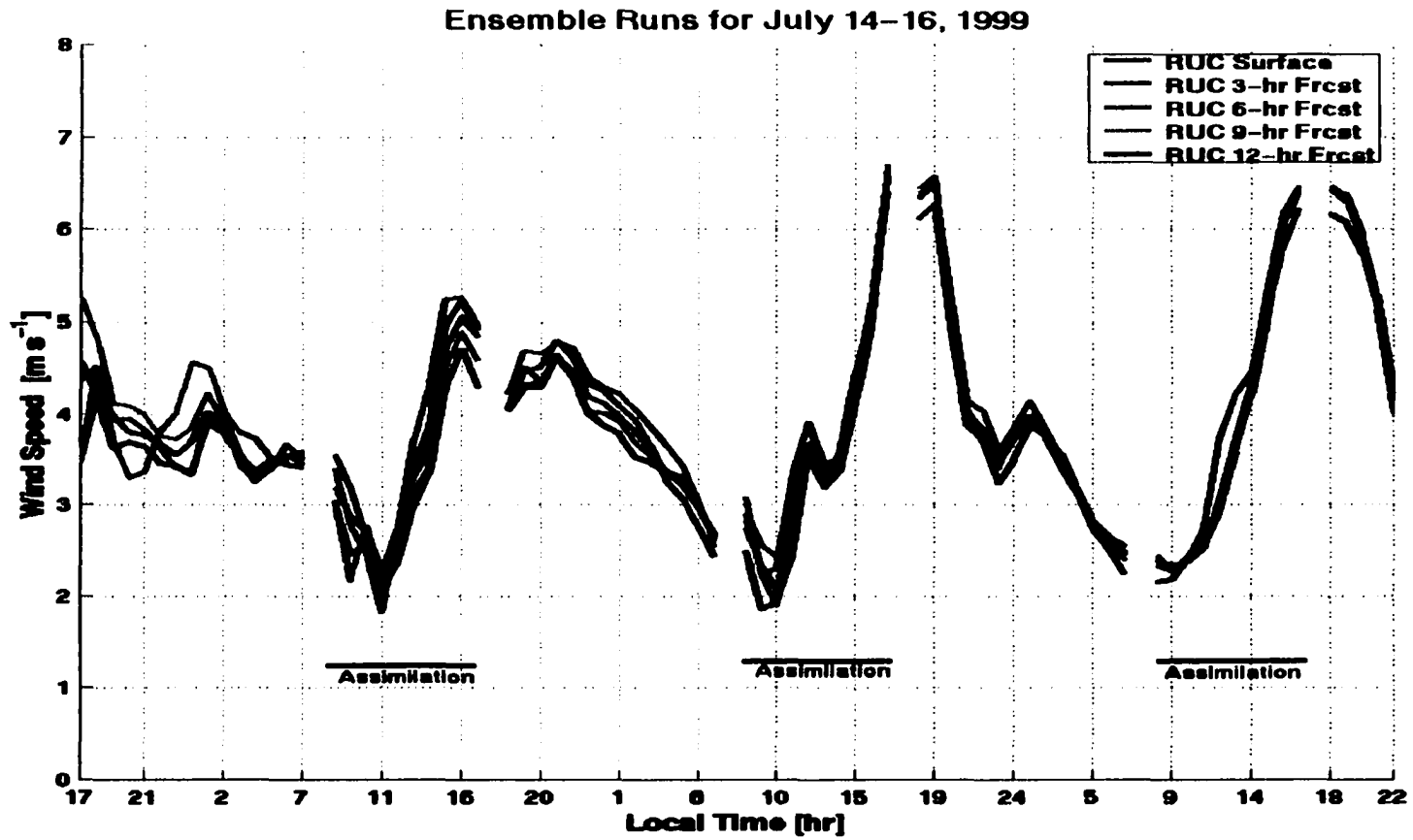


Figure 6.15c Results of domain average lowest model-level wind speed from five ensemble runs with RAMS coupled with cloud assimilation on July 14-16, 1999.

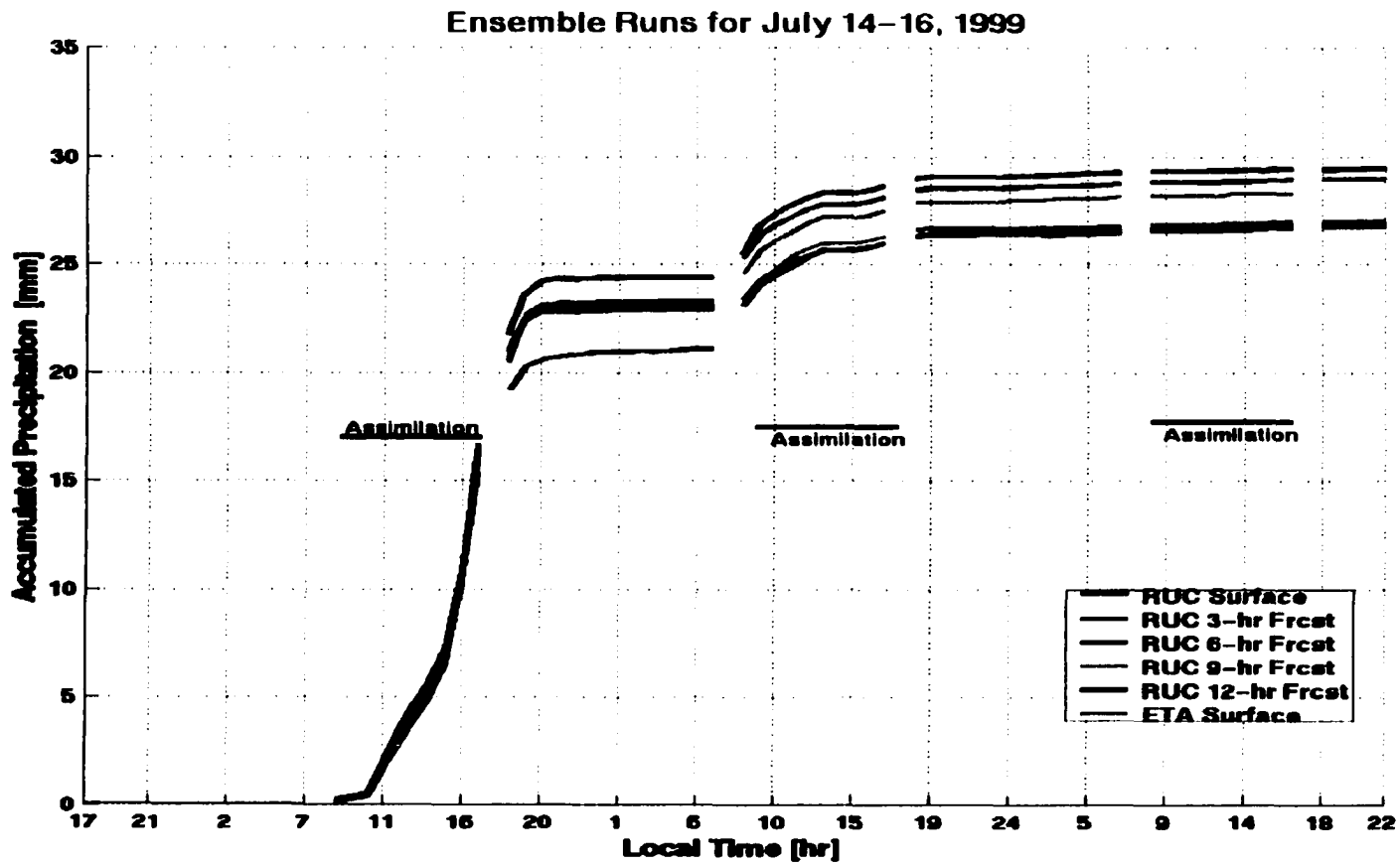


Figure 6.15d Results of domain average lowest model-level accumulated precipitation from five ensemble runs with RAMS coupled with cloud assimilation on July 14-16, 1999.

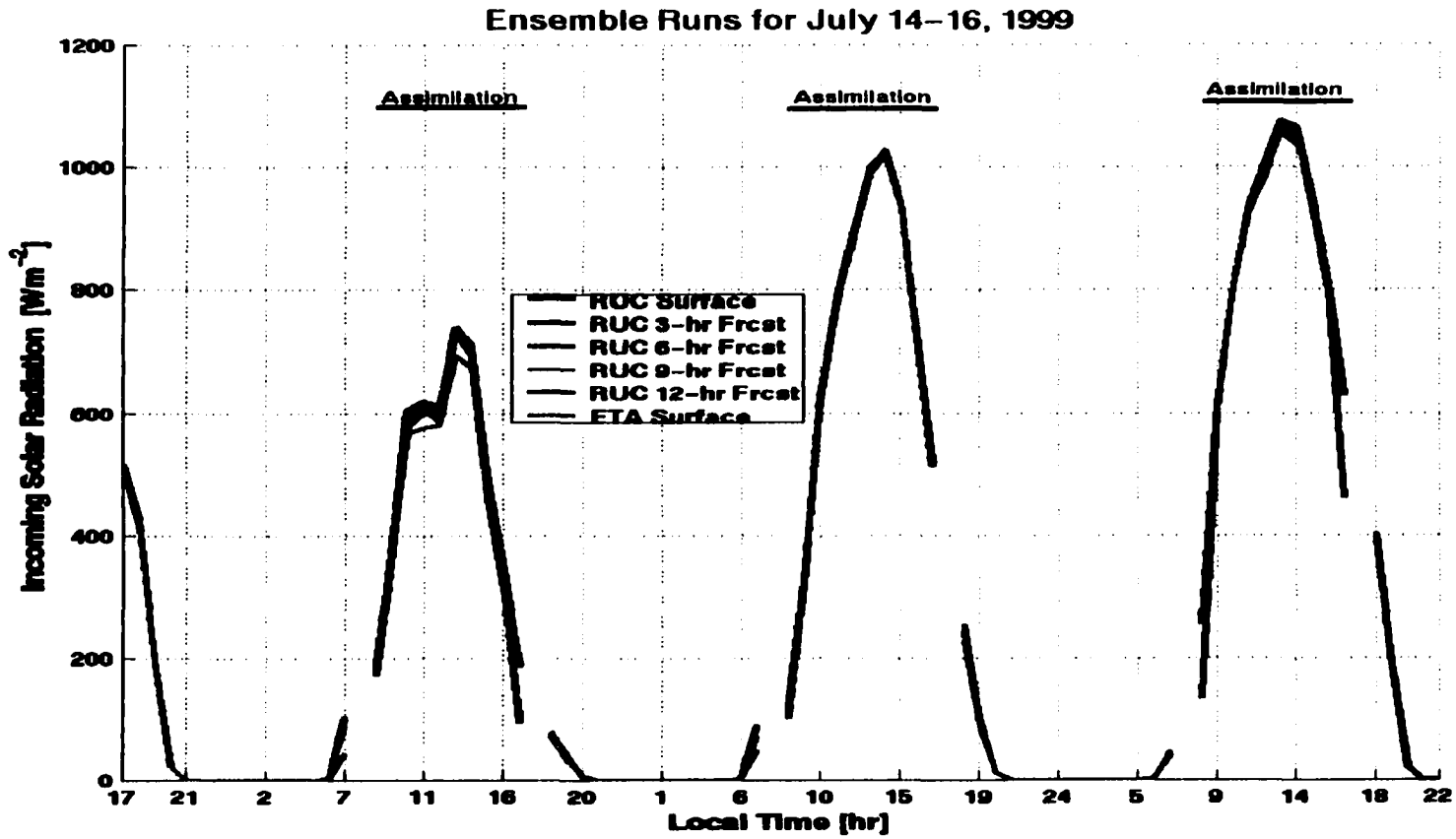


Figure 6.15e Results of domain average lowest model-level incoming solar radiation from five ensemble runs with RAMS coupled with cloud assimilation on July 14-16, 1999.

## CHAPTER 7

### SUMMARY, CONCLUSIONS AND RECOMMENDATIONS

#### 7.1 Summary

Notwithstanding the detailed parameterization schemes they use for clouds, radiation, and precipitation processes, mesoscale meteorological models coupled to realistic land surface models, such as RAMS, still predict cloud and their associated impact on surface radiation and precipitation with considerable error. However, accurate estimation of high-resolution surface radiation and precipitation fields are required for the hydrological application of these coupled models. Satellite remote sensing potentially represents a powerful innovative technique to improve definition and prediction of the required high-resolution fields by such models. This thesis describes research in which novel techniques were developed to acquire fine-scale information on cloud cover from the GOES visible imager, and to assimilate these data into the RAMS model to yield improved description of incoming short- and long-wave radiation and precipitation at the earth's surface.

The first step towards assimilating cloud cover in RAMS involved developing an automatic cloud-screening procedure to derive high resolution (4 km x 4km) fields of cloud cover from visible band GOES-10 data using a novel tracking procedure to determine the clear-sky composite image. The high resolution cloud properties derived using this cloud screening algorithm were used in the UMD GEWEX/SRB model, initially to produce estimates of surface solar radiation fields and, subsequently, to derive

estimates of vertically integrated cloud water and ice. Initially, an attempt was made to assimilate the satellite based estimates of surface solar radiation into RAMS, to redress weaknesses in the model-calculated surface radiation balance. However, this initial study revealed problems associated with inconsistencies between the revised solar radiation fields and the RAMS-calculated incoming long-wave radiation and precipitation fields, because modeled cloud cover remained unchanged and, consequently, these other surface fields retained their low, clear-sky values. Therefore exploration was made of the feasibility of directly assimilating cloud water/ice fields (derived from cloud optical depth) to update modeled cloud cover. This is a superior alternative because it allows the RAMS radiation and precipitation codes to calculate the actual spatial variability generated by the observed clouds. In the method adopted, the assimilated image takes the horizontal distribution of cloud from the satellite image but it retains a vertical distribution which is the area-average simulated by RAMS across the modeled domain in the time step immediately prior to cloud assimilation. The effect of assimilating GOES-derived cloud images at different frequencies was explored. Initially assimilation was made at 30- and 15-minute intervals, but ultimately assimilation was made every minute, the assimilated image being obtained by linear interpolation between the nearest 15-minute images. With a one-minute assimilation of interpolated images, RAMS simulated improved cloud patterns, both in terms of the magnitude and spatial distribution .

Comparisons were made between modeled variables and observed data from the AZMET array of surface stations for model runs with and without cloud assimilation to investigate the improvement (or otherwise) in RAMS' ability to describe surface

radiation and precipitation fields. As expected, cloud assimilation was found to substantially improve the RAMS model's ability to capture both the temporal and spatial variations in surface fields associated with the observed cloud cover. The most striking improvement was in the accuracy with which the model calculates incoming solar radiation. However, in addition, RAMS also showed a worthwhile improvement in the accuracy with which it calculated incoming long-wave radiation and precipitation, at least during the daylight hours when satellite data were available and assimilated.

The sensitivity of the above-described comparisons to model initiation was explored by making five-member ensemble runs starting from different initiation fields. In general, the results of these ensemble runs showed that, with cloud assimilation, RAMS is not sensitive to realistic perturbation of initial conditions. All the ensemble runs tended to converge within a few hours from initiation and they converged entirely 14 hours after initiation.

## **7.2 Conclusions**

The main goal of the research described in this dissertation was to provide an improved, high-resolution, regional diagnosis of three important surface variables, i.e. the downward short- and long-wave surface radiation fields and precipitation, by developing a method that involves assimilating satellite-derived, fine-resolution cloud cover into the model. It was clearly demonstrated that such a method can indeed be successfully developed and successfully applied. Not only did this greatly improve the surface fields

diagnosed by the model, it potentially enhances the modeling system's ability to make more accurate short-term forecasts of precipitation.

The primary conclusions that can be drawn on the basis of the research described in this thesis are as follows:

- It is possible to create an automatic cloud-screening procedure that uses real-time tracking (as opposed to retrospective analysis), and to use this as the basis of a cloud cover retrieval algorithm that is robust, functions correctly, and provides appropriate, fine-resolution detection of clouds.
- Using the above described cloud cover retrieval in the UMD GEWEX/SRB model does provide realistic estimates of solar radiation, but assimilating these estimates into RAMS gave inadequate improvement in the model-calculated surface fields because the associated fields of incoming long-wave radiation and precipitation were not simultaneously and consistently updated.
- It is possible to derive three-dimensional fields of cloud cover appropriate for assimilation into a mesoscale meteorological model from the retrieved horizontal cloud patterns by assuming that, on average across the modeled domain, the RAMS model computes a realistic vertical profile during the previous time-step, and this can be assimilated into RAMS without disrupting model stability.
- On average, there is a significant improvement in RAMS' ability to simulate both the overall amount and horizontal distribution of cloud fields when satellite observations are assimilated, although RAMS tends to evolve

“lumpy” clouds between assimilation cycles and, consequently, the preferable assimilation procedure is to assimilate cloud images every minute using cloud fields that are linearly interpolated between the nearest 15-minute GOES images.

- Cloud assimilation substantially increases the quality of the comparison between RAMS-calculated estimates of downward surface solar radiation and equivalent observations from the AZMET field networks during trial model simulation periods by extending the already good simulation in clear-sky conditions to give improved simulation during cloudy-sky conditions.
- Similar comparison between model-calculated precipitation estimates and AZMET observations demonstrated that cloud cover assimilation also gave a worthwhile improvement in the timing and, to some extent, magnitude of modeled precipitation, but the agreement was not perfect because of the sensitivity of the relationship between cloud and precipitation used in RAMS, and because comparison was made between point-sample observations of precipitation and area-average (4 km x 4 km) model estimates.
- A single-point comparison between model-derived and observed downward long-wave radiation provided evidence that RAMS ability to simulate this field is also improved by assimilating cloud cover, most significantly during the day when cloud cover information is available but also, to some extent, even during the subsequent night.

- The comparison between observed and modeled long-wave radiation provided evidence that using the Chen/Cotton radiation scheme is preferable to using the Harrington radiation scheme in RAMS, at least in the semi-arid study region where the comparisons was made in this study.
- Five-member ensemble runs with different initial conditions demonstrated that all of the above conclusions remain valid and are independent of the model initiation

### **7.3 Recommendations**

With respect to application, given the proven feasibility and value of the cloud assimilation technique developed during the research described in this thesis, the following recommendations can be made:

- There is clearly value in extending the capability to assimilate cloud cover data to other mesoscale meteorological models and, in particular, to the MM5 (i.e. the Pennsylvania State University/National Center for Atmospheric Research mesoscale model) which, at this writing, is becoming a community standard model.
- There is a need to investigate and extend the off-line implementation of cloud cover assimilation capability developed in this research into real time applications, with a view to improving short-term forecasting capability, and providing hydrological benefit through flood forecasting and weather risk mitigation.

Regarding extending the capability developed during the present research, important additional research issues include the following:

- The use of remotely sensed cloud-top temperatures derived from infrared imagery better to specify the vertical position of clouds in each grid square in the assimilated cloud fields should be explored, rather than assuming the RAMS-calculated area-average vertical distribution as in this research. If the position of the top of the cloud is specified in this way, perhaps the cloud-base can then be estimated for each grid square by assuming there is only one cloud layer and the vertical distribution of cloud water/ice (derived from visible imagery) is proportional to that which would be produced by pseudo-adiabatic ascent from cloud base to cloud top.
- Although it was acceptable in the present research to assume there was no discrepancy between the location of the cloud and that of the model grid, in general this is not necessarily always true. Consequently, in future research the potential to correct pixel locations in GOES visible images by applying pixel-based spatial displacement corrections using data from two GOES satellites (Mahani, 2000) should be explored.

## REFERENCES

- Arakawa, A., and Lamb V. R., 1977: Computational design of the basic dynamical processes of the UCLA general circulation model. *Meth. Comput. Phys.* 17, 174-264.
- Avissar R., Mahrer Y., 1988: Mapping frost-sensitive areas with a three-dimensional local-scale numerical model. Part I: Physical and numerical aspects. *J. Appl. Meteor.*, 27, 400-413.
- Bengtsson L., and J. Shukla, 1988: Integration of space and in situ observations to study global climate change. *Bull. Am. Meteorol.*, 24, 128-143.
- Chen, C., and W. R. Cotton, 1983: A one-dimensional simulation of the stratocumulus-capped mixed layer, *Boundary Layer Meteorology*, 85:391-421.
- Clark T. L., and Farley R. D., 1984: Severe downslope windstorm calculations in two and three spatial dimensions using anelastic interactive grid nesting: A possible mechanism for gustiness. *J. Atmos. Sci.*, 41, 329-350.
- Clark T. L., 1977: A small-scale dynamic model using a terrain-following coordinate transformation. *J. Comput. Phys.*, 24, 186-215.
- Cotton W. R., and G. J. Tripoli, 1978: Cumulus convection in shear flow – three-dimensional numerical experiments. *J. Atmos. Sci.*, 35, pp. 1503-1521.
- Cotton G.J., Tripoli, R. M. Rauber, and E. A. Mulvihill, 1986: Numerical simulation of the effects of varying ice crystal nucleation rates and aggregation processes on orographic snowfall. *J. Climate Appl. Meteor.*, 25, 1658-1680.
- Cotton, W.R. and R.A. Anthes, 1989, Storm and Cloud Dynamics. *International Geophysics Serial 44*, Academic Press, 883 p.
- Deardorf J. W., 1980: Stratocumulus-capped mixed layers derived from a three-dimensional model. *Bound.-Layer Meteor.*, 18, 495-527.
- Gabriel, P., J. Y. Harrington, G. L. Stephens, and T. L. Schneider, 1998: Adjoint Perturbation Method Applied to Two-Stream Radiative Transfer, *J. Quant. Spectrosc. Radiat. Transfer*, 59, pp. 1-24.
- Garatuza-Payan, J., 1999: Evaporation from irrigated crops: Its measurement, modeling and estimation from remotely sensed data, Ph.D. Dissertation, Department of Hydrology and Water Resources, University of Arizona, 225 pp.

- Garatuza-Payan, J., R.T. Pinker, and W. J. Shuttleworth 2000, High-Resolution Cloud Observations for Northwestern Mexico from GOES-7 Satellite Observations, *Journal of Oceanic and Atmospheric Technology*, (in press).
- Hansen J. E., and L. D. Travis, 1974: Light scattering in planetary atmospheres. *Space Sci. Rev.*, 16, 527-610.
- Hanson H. P., 1991: Marine stratocumulus climatologies. *Inter. J. Climate*. 11, 147-164.
- Harrington, J. Y., 1997: The effects of radiative and microphysical processes on simulated warm and transition season arctic stratus, Ph. D. Dissertation, Atmospheric Science Paper No. 637, Department of Atmospheric Science, Colorado State University, 289 pp.
- Herman G., Goody R., 1976: Formation and persistence of summertime arctic stratus clouds. *J. Atmos. Sci.*, 33, 1537-1553.
- Houser, P. R., 1996: Remote Sensing Soil Moisture Using Four Dimensional Data Assimilation, Ph. D. Dissertation, Department of Hydrology and Water Resources, University of Arizona, 430 pp.
- Joiner J., and A. M. Da Silva, 1998: Efficient methods to assimilate remotely sensed data based on information content, *Q. J. R. Meteorol. Soc.*, 124, pp. 1669-1694.
- Lacis A. A., Hansen J., 1974: A parameterization for the absorption of solar radiation in earth's atmosphere. *J. Atmos. Sci.*, 31, 118-133.
- Leighton H. G., 1979: Application of the Delta-Eddington method to the absorption of solar radiation in the atmosphere. *Atmos. Ocean*, 18, 43-52.
- Lipton A. E., 1993: Cloud Shading Retrieval and Assimilation in a Satellite-Model Coupled Mesoscale Analysis System, *Monthly Weather Review*, 121, 3062-3081.
- Lipton A. E., and G. D. Modica, 1999: Assimilation of Visible-Band Satellite Data for Mesoscale Forecasting in Cloudy Conditions, *Monthly Weather Review*, 127, 265-278.
- Lousie J. F., 1979: A parametric model of vertical eddy fluxes in the atmosphere. *Bound.-Layer Meteor.*, 17, 187-202.
- Mahani, E. S., X. Gao, S. Sorooshian, and B. Imam, 2000: Estimating cloud top height and spatial displacement from scan-synchronous GOES images using simplified IR-based stereoscopic analysis. *Journal of Geophysical Research*, 105, 15597-15608.

- Mahrer Y., Pielke R. A., 1977: A numerical study of the airflow over irregular terrain. *Beitrage zur Physik der Atmosphere*, 50, 98-113.
- Manebe R. J., Stouffer, M. J. Spelman, and K. Bryan, 1991: Transient responses of a coupled ocean-atmosphere model to gradual changes of atmospheric CO<sub>2</sub>. Part 1: Annual mean response. *J. Climate*. 4, 785-818.
- Manton M. J., and W. R. Cotton, 1977b: Parameterizations of the atmospheric surface layer. *J. Atmos. Sci.*, 34, pp. 331-334.
- McNider R. T., Pielke R. A., 1981: Diurnal boundary-layer development over sloping terrain. *J. Atmos. Sci.*, 38, 2198-2212.
- Meyers M. P., P. J. Demott, and W. R. Cotton, 1991: New Primary Ice-Nucleation Parameterizations in an Explicit Cloud Model, *Journal of Applied Meteorology*, 3, 708-721.
- Meyers M. P., and W. R. Cotton, 1992: Evaluation of the potential for wintertime quantitative precipitation forecasting over mountainous terrain with an explicit cloud model. Part I: Two-dimensional sensitivity experiments. *J. Appl. Meteor.*, 31, 26-50.
- Pielke R.A., W. R. Cotton, R. L. Walko, C. J. Tremback, W. A. Lyons, L. D. Grasso, M. E. Nicholls, M. D. Moran, D. A. Weskey, T. J. Lee, and J. H. Copeland, 1992: A Comprehensive Meteorological Modeling System – RAMS, *Meteorol. Atmos. Phys.* 49, 69-91.
- Pinker R.T., and Ewing, J. A. (1985), Modeling surface solar radiation: model formulation and validation, *J. Climate Appl. Meteor.* 24:389-401.
- Pinker, R.T. and Laszlo, 1992, Modeling Surface Solar Irradiance for Satellite Applications on Global Scale, *Journal of Applied Meteorology*, 3:194-212.
- Pinker, R.T., W.P. Kustas, I. Laszlo, M. S. Moran, and A. R. Huete, 1994, Basin-Scale Solar Irradiance Estimates in Semiarid Regions Using GOES 7. *Water Resources Research*, (30)5:1375-1386.
- Pinker, R.T., R. Frouin, and Z. Li, 1995: A Review of Satellite Methods to Derive Surface Shortwave Irradiance, *Remote Sens. Environ.* 51:108-124.
- Pruppacher, H.R. and D.J. Klett, 1980, Microphysics of Clouds and Precipitation. D. Reidel, Dordrecht, The Netherlands, 714 p.

Randall D. A., J. Coakley, C. Fairall, R. Kropfli, and D. Lenschow, 1984: Outlook for research on marine subtropical stratocumulus clouds. *Bull. Amer. Meteor. Soc.*, 65, 1290-1301.

Rossow, W.B. and L.C. Garder, 1993a, Cloud Detection Using Satellite Measurements of Infrared and Visible Radiances for ISCCP. *Journal of Climate*, 6:2341-2369.

Rodgers C. D., 1967: The use of emissivity in atmospheric radiation calculations. *Quart. J. Roy. Meteor. Soc.*, 93, 43-54.

Reynolds, D. W. and T. H. Vonder Haar, 1977, A Bi-Spectral Method for Cloud Parameter Determination. *Monthly Weather Review*, 105:446-457.

Ruggiero F. H., G. D. Modica and A. E. Lipton, 2000: Assimilation of Satellite Imager Data and Surface Observations to Improve Analysis of Circulations Forced by Cloud Shading Contrasts, *Monthly Weather Review*, 128, 434-448.

Schiffer, R.A. and W.B. Rossow, 1983, The International Satellite Cloud Climatology Project (ISCCP): The First Project of the World Climate Research Program. *Bulletin of the American Meteorological Society*. 64:779-784.

Seze, G. and W. B. Rossow, 1991, Time-cumulated Visible and Infrared Radiance Histograms used as Description of Surface and Cloud Variations, *International Journal of Remote Sensing*, 12:877-920.

Shuttleworth, W. J., 1999, Combining remotely-sensed data using aggregation algorithms, *Hydrology and Earth System Science*, 2(2-3), 149-158.

Slingo A., 1990: Sensitivity of the Earth's radiation budget to changes in low clouds. *Nature*, 343, 49-51.

Stephens G. L., 1978: Radiation profiles in extended water clouds. Theory. *J. Atmos. Sci.*, 35, 2111-2122.

Stephens G. L., S. Ackerman and E. A. Smith, 1984: A Shortwave Parameterization Revised to Improve Cloud Absorption, 41, 687-690.

Stephens, G. L., The parameterization of radiation for numerical weather prediction and climate models, *Mon. Weather Rew.*, 1984, 112, 826.

Stewart, J. B., H. A. R., deBruin, J. Garatuza-Payan, A. R. van den Berg, L. Cervera-Gomez, M. Domitsu-Kono, J. G. Osuna-Chavez, and C. J. Watts, 1994, PC-Based

System to Estimate Hydrological Variables in Northwest Mexico Using Satellite Data, Final Report (EEC Project: CI1\*-CT91-0900), Wallingford, UK.

Stowe, L. L., C. G. Wellemeyer, T. F. Eck, H. Y. M. Yeh, and the NIMBUS-7 Cloud Data Processing Team, 1989. NIMBUS-7 Global Cloud Climatology. Part I: Algorithms and Validation. *Journal of Climate*, 1:445-470.

Tremback C. J., Tripoli G. J., Cotton W. R., 1985: A regional scale atmospheric numerical model including explicit moist physics and a hydrostatic time-split scheme. *Preprints, 7<sup>th</sup> AMS Conference on Numerical Weather Prediction*, June 17-20, Montreal, Quebec, Canada, Amer. Meteor. Soc., Boston, 433-434.

Tremback C. J., 1990: Numerical simulation of a mesoscale convective complex: model development and numerical results. Ph.D. dissertation, Atmos. Sci. Paper No. 465, Department of Atmospheric Science, Colorado State University, Fort Collins, CO 80523, 247 pp.

Tripoli G. J., Cotton W. R., 1980: A numerical investigation of several factors contributing to the observed variable intensity of deep convection over south Florida. *J. Appl. Meteor.*, 19, 1037-1063.

Tripoli G. J., and W. R. Cotton 1982: The Colorado State University three-dimensional cloud/mesoscale model-1982. Part I: General theoretical framework and sensitivity experiments. *J. Rech. Atmos.* 16, 185-220.

Tripoli G. J., Cotton W. R., 1986: An intense, quasi-steady thunderstorm over mountainous terrain Part IV: Three-dimensional numerical simulation. *J. Atmos. Sci.*, 43, 896-914.

Toth, J. J., D. C. Goodrich, M. S. Moran, R. L. Scott, D. C. Hymer, C. Harlow, I. Yucel, W. J. Shuttleworth, A. G. Chehbouni, G. Boulet, C. Watts, D. I. Cooper, M. W. Kirkland, R. Avissar, R. T. Pinker, and L. E. Hipps, 1998: An Overview of Spatially Distributed Surface Fluxes of Heat and Moisture Across the Semi-Arid San Pedro Basin, AMS Special Symposium on Hydrology, Preprints, 11-16 Jan. 1998, Phoenix.

Yamamoto G., 1962: Direct absorption of solar radiation by atmospheric water vapor carbon dioxide and molecular oxygen. *J. Atmos. Sci.*, 19, 182-188.

Yucel, I, W. J. Shuttleworth, J. Washburne, and F. Chen, 1998, Evaluating NECEP ETA Model-Derived Data Against Observations, *Monthly Weather Review*, 126, 7, 1977-1991.

- Walko R. L., C. J. Tremback, R. A. Pielke, and W. R. Cotton, 1995a: An interactive nesting algorithm for stretched grids and variable nesting ratios. *J. Appl. Meteor.*, 34, 994-999.
- Warren, S. G., C. J. Hahn, J. London, R. M. Chervin, and R. L. Jenne, 1986, Global Distribution of Total Cloud and Cloud Type Amounts Over the Ocean. NCAR Technical Note TN-317+STR/DOE Technical Report ER-0406, 42p + 170 maps. [NTIS NUMBER de90-00-3187].
- Wielicki B. A., R. D. Cess, M. D. King, D. A. Randall, and E. F. Harrison, 1995, Mission to Planet Earth: Role of Clouds and Radiation in Climate, *Bulletin of the American Meteorological Society*, Vol:76, 11, 2125-2153.
- Wood E. F., D. P. Lettenmaier, V. G. Zartarian, 1992: A land-Surface Hydrology Parameterization With Subgrid Variability for General Circulation Models, *Journal of Geophysical Research*, 97, D3, 2717-2728.
- Wylie, D. P. and Menzel, W. P., 1989. Two Years of Cloud Cover Statistics using VAS. *Journal of Climate*, 2:280-392.
- Vukicevic T., and J. Paegle 1989: The influence of one-way interacting lateral boundary conditions upon predictability in bounded numerical models. *Mon. Wea. Rev.*, 117, 340-350.